Renewable Energy Generation and Storage: From Microwires to Macro-Energy Systems

Thesis by

Kathleen Kennedy

In Partial Fulfillment of the Requirements for the Degree of

Doctor of Philosophy.

CALIFORNIA INSTITUTE OF TECHNOLOGY

Pasadena, California

2021

(Defended May 4th, 2021)

Kathleen Kennedy
ORCID: 0000-0002-7125-4871

ACKNOWLEDGEMENTS

I am deeply grateful to the many people who helped me reach graduate school and somehow survive the experience with my sanity (mostly) intact.

First, I would like to thank my committee members for taking the time to review this thesis. Professor Keith Schwab taught one of my favorite courses at Caltech, and often provided fun discussions about that morning's NPR story that were an enjoyable way to start an early morning solid state physics class. Professor Johnson approaches legendary status in the department, and I am glad I got the chance to take his thermodynamics course before his retirement. Professor Gray is a long-time friend of the Lewis Group, and always guaranteed to make the day a little brighter from a chance meeting around campus. And of course, I would particularly like to thank my adviser, Nate Lewis. The Lewis Group is a truly unique environment, and it has given me a chance to learn not only about science, but about the impact I hope to have on the world.

I would also like to thank several others for advising who have given me feedback and support at various points in my PhD. Thank you to Ken Caldeira for his warm welcome into the MEM group and for bringing together such a wonderful group of people. Thank you to Bruce Brunschwig for providing much-appreciated feedback on my first paper. And thank you to Kimberly Papadantonakis, who was the best combination of officemate, adviser, and friend I could have asked for.

Nothing at Caltech would work without the amazing administrative staff. Thank you to Christy Jenstad and Jennifer Blankenship for keeping the APhMS department running, and to Barbara Miralles for everything she does for the Lewis Group.

Much of my work would not have been possible without the facilities of the Kavli Nanoscience Institute (KNI) and the support of the KNI staff. Thank you to Guy DeRose, Bert Mendoza, Nathan Lee, Alex Wertheim, and Matthew Hunt for all the time they spent training me on instruments and helping me troubleshoot my processing.

I have been lucky to have many amazing mentors and collaborators during my time at Caltech. Stefan Omelchenko was my department mentor in my first year, and I am incredibly grateful for his help in finding my way at Caltech, introducing me to the Lewis Group, and helping me prepare for my Candidacy exam. Sisir Yalamanchili spent many hours helping me learn how to use instruments in the KNI and was always my first stop when I needed to figure out problems in my processing or just wanted to bounce ideas off of someone. Paul Kempler helped me get started on the project that became my first paper and kept me supplied with silicon microwires for my experiments. Miguel Cabán-Acevedo was an enormous help in making that first paper a reality with his insights and expert FIB work. Azhar Carim was always ready to share his insights from his many years in the Lewis Group, and assisted with some of my tougher SEM imaging challenges.

I began my energy systems modeling work in the middle of the coronavirus pandemic, which could have been a terrible experience. Instead, it was wonderful, entirely because of the kind support at every step from Tyler Ruggles, Lei Duan, Katherine Rinaldi, and Jackie Dowling. Thank you all for every zoom call, email, and slack message that helped me figure out what I was doing and actually produce a paper.

I also want to thank Pai Buabthong, Ethan Simonoff, Paul Nunez, Katie Chen, Michael Mazza, and Ellen Yan for helpful conversations about science, how to navigate the pandemic, and life in general.

No list like this could be complete without my roommates, who helped me get through classes in first year and everything else in the years since. Thank you to Ben Herren, Kevin Korner, Sydney Corona, Yayatti Chachan, and Emma Reinhart for everything.

Another big part of what kept me going in my time at Caltech was working with the Caltech Y. Thank you to Greg Fletcher, Athena Castro, and the rest of the Y staff who support so many amazing programs for students. The work I have done with the Y's Student Activism Speaker Series has changed how I see the world and what I want out of my career, and I am so grateful for the opportunity to be a part of it.

Finally, I want to thank my family and my wonderful boyfriend, Jonathan Gross. Thank you to my family for believing in me when I got the crazy idea to start a PhD and thank you for listening to all of my complaints and difficulties along the way. Thank you to Jonathan for all your support, for being willing to spend an extra few years in LA, and for sharing your couch-potato dog with me.

Kathleen Kennedy
May 2021
Pasadena, CA

ABSTRACT

Anthropogenic greenhouse gas emissions must reach net-zero quickly in order to meet the Paris Agreement goal of no more than 2 °C of warming, which will require decarbonizing the entire economy. Certain sectors are more difficult to decarbonize than others given current technological limitations. This thesis focuses on efforts to support decarbonization of such sectors through the development of solar fuels devices to produce green hydrogen and through macro-energy systems modeling.

Long-term stability of light-absorbing materials remains a substantial barrier to the viability of solar fuels devices. In this thesis, we identify corrosion pathways in TiO_2-protected silicon microwire arrays in a polymer membrane either attached to a substrate or free-standing. Both top-down and bottom-up corrosion processes were observed in both morphologies, with top-down corrosion arising from defects in the TiO_2 protection layer and bottom-up corrosion occurring through the substrate and membrane. We also present fabrication methods for III-V nanowire structures that could allow for enhanced efficiency in future solar fuels devices.

Solar energy incident on the earth's surface can be converted to usable electricity through multiple technologies. At present, electricity generation by concentrated solar power (CSP) is much more expensive than from photovoltaics (PV), but thermal energy storage (TES), especially when coupled to CSP, is much cheaper than chemical battery storage. In Chapter 4 of this dissertation, we use a macro-scale energy model with historical demand in conjunction with hourly historical weather data to analyze the role of CSP/TES relative to PV/batteries in an idealized least-cost wind/solar/storage system that reliably meets hourly demand. Without TES, minimal CSP generation is built because CSP and PV have similar generation profiles, but solar photovoltaics are currently much cheaper on a dollar-per-kWh produced basis than CSP generation. However, CSP+TES occupies a small niche providing valuable grid services by adding flexibility due to the favorable cost of storing energy in TES compared to batteries. Consequently, CSP does not compete directly with PV, but rather TES competes with short-duration storage from

batteries, with the coupled CSP technology providing cost-effective grid services to achieve reliability. A cost-sensitivity analysis shows that penetration of CSP+TES in this idealized wind/solar/storage electricity system is primarily limited by the relatively high current CSP generation costs. These results provide a framework for researchers and decision-makers to assess the role of CSP+TES in future electricity systems.

PUBLISHED CONTENT AND CONTRIBUTIONS

Kennedy, K. M.; Kempler, P. A.; Cabán-Acevedo, M.; Papadantonakis, K. M.; Lewis, N. S. Primary Corrosion Processes for Polymer-Embedded Free-Standing or Substrate-Supported Silicon Microwire Arrays in Aqueous Alkaline Electrolytes. *Nano Lett.* **2021**, *21* (2), 1056–1061. https://doi.org/10.1021/acs.nanolett.0c04298.

K.M.K. participated in the conception of the project and design of the study, performed the corrosion experiments, optical and SEM characterization, performed image analysis, and wrote the text. Adapted with permission from the copyright holder. {American Chemical Society, 2021}

TABLE OF CONTENTS

LIST OF FIGURES

LIST OF TABLES

Chapter 1

INTRODUCTION

1.1 Climate Change and Anthropogenic Causes of Warming

Temperature records over the past century show a notable rise in land and ocean temperatures, with the seven hottest years on record all occurring since 2014 (Figure 1.1).[3] Multiple studies using different measures of consensus have shown that there is strong agreement among >90% of climate scientists that this change is due to human activity.[4,5] The Intergovernmental Panel on Climate Change (IPCC) summarized this finding in their 5th Assessment Report, saying:

> "Anthropogenic greenhouse gas emissions have increased since the pre-industrial era, driven largely by economic and population growth, and are now higher than ever. This has led to atmospheric concentrations of carbon dioxide, methane and nitrous oxide that are unprecedented in at least the last 800,000 years. Their effects, together with those of other anthropogenic drivers, have been detected throughout the climate system and are *extremely likely* to have been the dominant cause of the observed warming since the mid-20th century." [6]

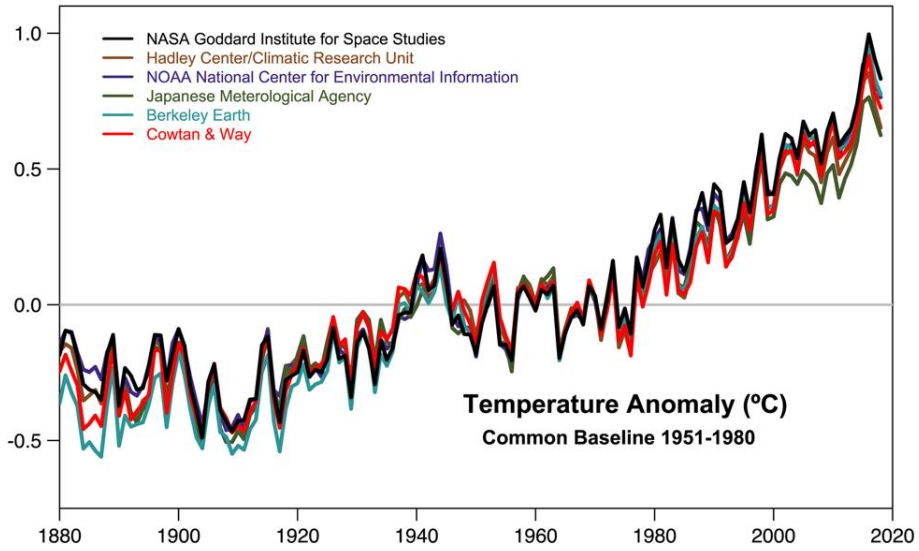

Figure 1.1 Comparison of six analyses of the annual global surface temperature anomaly through 2018. NASA = National Aeronautics and Space Administration; NOAA = National Oceanic and Atmospheric Administration. Reproduced with permission from Lenssen, et al.[7]

The warming caused by anthropogenic emissions of greenhouse gases (GHG's) is already impacting many different natural phenomena, with more severe impacts expected as warming continues.[6] These impacts include greater frequency and intensity of droughts, heatwaves, and precipitation events such as hurricanes.[8] Excess carbon uptake by the oceans is causing ocean acidification, which threatens many species and ecosystems, as well as ocean industries such as fishing.[8] The Greenland and Antarctic ice sheets are losing mass at an accelerating rate, Arctic sea-ice extent is shrinking, permafrost is warming, and sea levels are rising.[9] All of these phenomena have negative implications for human-serving systems such as food, water, energy, tourism, and trade.[9] While many of these effects of climate change are already occurring and therefore impossible to avoid entirely, it is still possible to mitigate their progression if we act quickly.[8]

1.2 Net-Zero Emissions

In 2015, the Paris Agreement was adopted by 196 countries seeking to limit global warming to less than 2 °C, or preferably less than 1.5 °C compared to preindustrial levels.[10] Current estimates suggest that approximately 1 °C of warming has already taken place, making urgent action a necessity to meet these goals.[6] The amount of warming experienced by the climate due to greenhouse gas emissions is determined by cumulative emissions going back to the beginning of the industrial period.[11] The total amount of greenhouse gases that may be emitted before reaching a given threshold of warming is often referred to as the "carbon budget." [11] Because the relevant quantity is cumulative emissions rather than annual emissions, staying within a given carbon budget requires reaching net-zero emissions, where anthropogenic sources and sinks are balanced and the sum of human activity does not increase the level of GHG's.[6] If emissions cannot be reduced quickly enough, we could overshoot the carbon budget and then need to achieve net-negative emissions later in the century to stay below the warming threshold defined by the Paris Agreement.[11]

These already difficult targets of net-zero or net-negative emissions are made even more challenging by the expected growth in global energy demand needed to support economic growth, particularly in the global south, and population growth.[12] Figure 1.2 shows the

projected growth in global energy demand through mid-century based on 2019 data prior to the coronavirus pandemic. This analysis projected ~50% growth in energy demand by 2050, a dramatic increase primarily driven by growth in non-OECD nations.[12] As the pandemic is ongoing at the time of this writing, it remains uncertain how big an impact it will have on future energy demand. Figure 1.3 shows a projection for US energy demand from the US Energy Information Administration that includes the impact of the pandemic. That projection suggests that growth will be slower compared to pre-pandemic estimates, with energy demand not returning to 2019 levels until 2029.[13] However, despite this substantial change due to the pandemic, energy demand is still expected to increase by 2050 in the reference scenario.[13] Therefore, although there is uncertainty about the recovery path after the pandemic, it is reasonable to assume that some amount of energy production growth will still be needed in the coming decades to meet future demand. In order to have any hope of meeting the net-zero targets necessitated by the Paris Agreement warming goals, this growth must come from green sources such as those discussed in this thesis.[11]

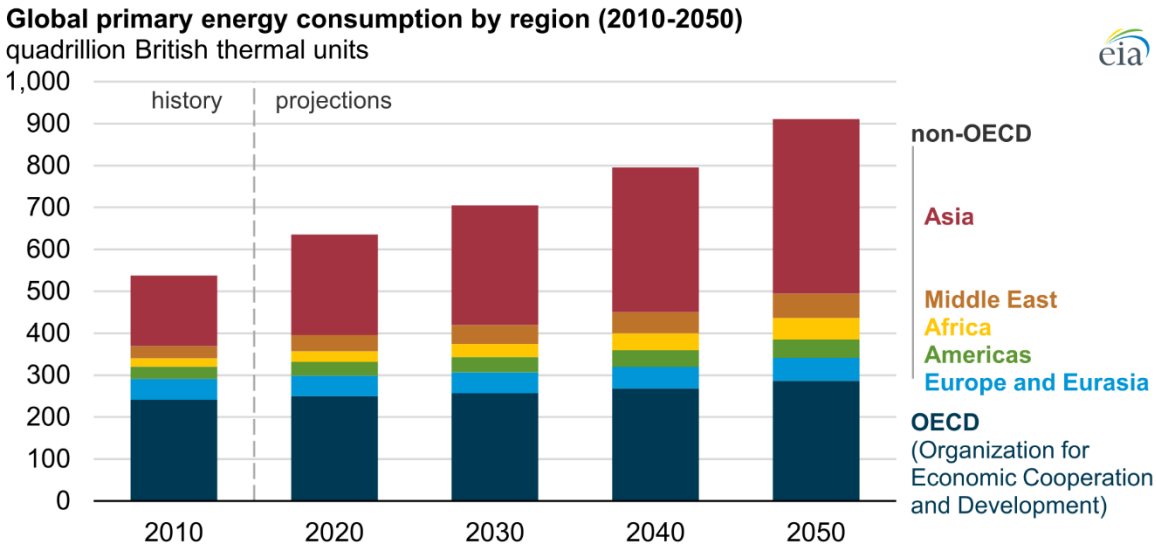

Figure 1.2 Projection of global energy demand through 2050 without considering the impact of the coronavirus pandemic. Source: U.S. Energy Information Administration, International Energy Outlook (Sep 2019).[12]

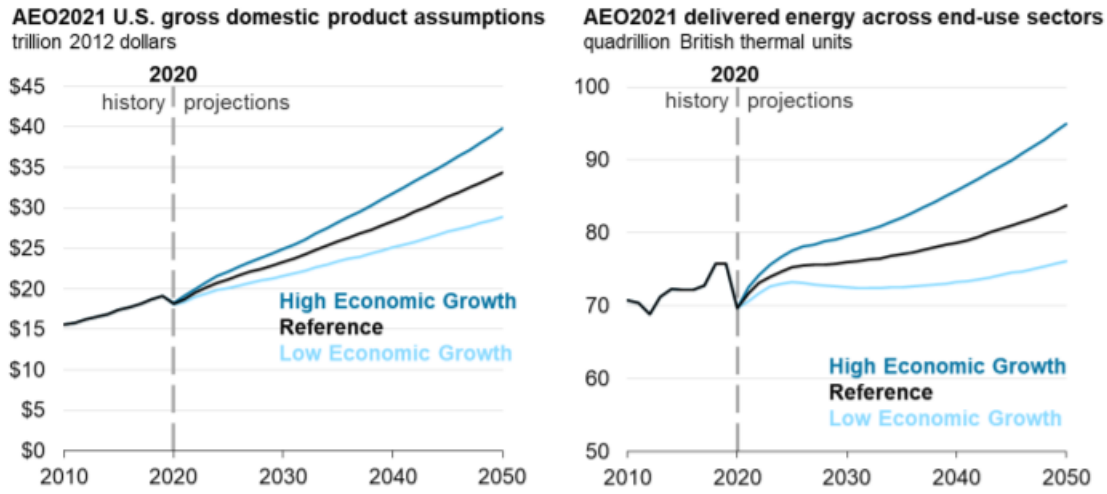

Figure 1.3 Projection of US GDP and US energy demand through 2050, including the impact of the coronavirus pandemic. Source: U.S. Energy Information Administration, Annual Energy Outlook (Feb 2021).[13]

1.2.1 Emissions by Sector

Reaching net-zero emissions will require massive changes across all sectors of the global economy.[6,14] While this transformation will present challenges in all sectors, certain areas are particularly difficult to decarbonize given current technological and economic limitations.[14] A summary of such "difficult-to-eliminate" emissions using data from 2014 is given in Figure 1.4. The first sector identified is the production of iron, steel, and cement, which account for ~9% of global emissions.[14] They are not only energy intensive processes, but they also produce CO_2 directly through chemical reactions inherent to the processes.[14] While these remain important problems that warrant more research and innovation, they are outside the scope of this work. This thesis will focus on projects related to the other two difficult-to-decarbonize areas identified in Figure 1.4 – transport related emissions shown in orange and load-following electricity shown in red.

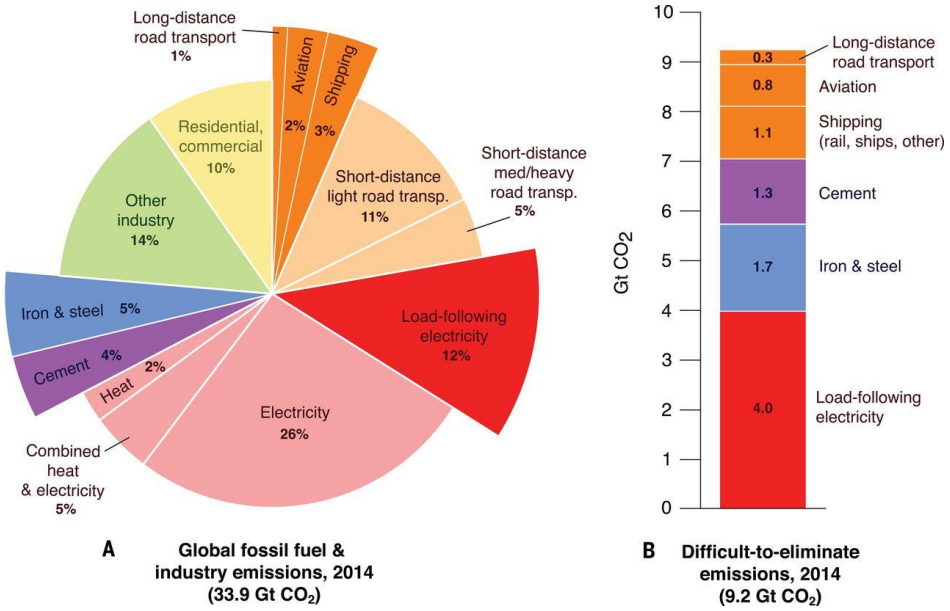

Figure 1.4 Difficult-to-eliminate global greenhouse gas emissions from 2014. (A and B) Estimates of CO2 emissions related to different energy services, highlighting those services that will be the most difficult to decarbonize, and the magnitude of 2014 difficult-to-eliminate emissions. Totals and sectoral break-downs shown are based primarily on data from the International Energy Agency and EDGAR 4.3 databases. From Davis, et al.[14] Reprinted with permission from AAAS.

1.2.2 Load-Following Electricity

Emissions from electricity generation account for the largest share of global greenhouse gas emissions of any single economic sector.[6] There is a consensus among many studies of electricity production that variable renewable energy (VRE) resources such as solar and wind can decarbonize a large part of the electricity sector, but moving beyond a generation mix of around ~80% renewables to reach full decarbonization becomes much more difficult.[14–16] The inherent variability of solar and wind power due to weather patterns makes it difficult to ensure there is always sufficient generation to meet electricity demand.[15,17] This variability persists on a range of timescales, necessitating strategies to deal with hourly changes, day-night cycling, seasonal variation, and inter-annual variability.[17]

Commonly proposed strategies to accommodate this variability include building more long-distance transmission into electrical grids, use of firm generators such as nuclear reactors, demand-response

mechanisms to align electrical demand more closely with VRE supply, and grid-scale energy storage.[16,18–20] Long-distance transmission can decrease the impact of variability by averaging supply over a larger geographic area, making the electrical supply more resilient to localized weather changes.[16,21,22] Firm generators that can ramp quickly can fill resource gaps in VRE's, thereby reducing the need for costly energy storage technologies.[19,23] Grid-scale energy storage comes in many different forms that can supply different grid services. This thesis will sort them roughly into "short-duration" storage over the course of a few hours or days, and "long-duration" storage on the scale of months or years. Studies suggest that long-duration storage could substantially decrease the cost of 100% renewable electricity systems by reducing the need to overbuild generation technologies.[20] Battery storage and thermal energy storage will be discussed in this thesis as potential short-duration storage technologies. Current battery storage costs are high compared to dispatchable fossil fuels such as natural gas, and will likely remain so even with battery prices dropping rapidly.[24] Thermal energy storage is cheap, but suffers from low round-trip efficiency unless tied to high-cost generation technologies such as concentrated solar power.[25–27] Using hydrogen gas as a storage medium in a "power-to-gas-to-power" (PGP) process will be considered as a long-duration storage due to the low losses associated with a stable chemical fuel.[20]

1.2.3 Transportation and Fuels

Emissions generated by transportation come from many different modes including personal vehicles, light-duty trucks, long-haul trucks, trains, airplanes, and ships.[14] Some of these emissions can be avoided without technological innovation simply by switching modalities. The Institute for Transportation and Development Policy (ITDP) estimates that 40% of urban passenger transport emissions could be eliminated by 2050 if the world expands public transportation, walking, and cycling in cities.[28] These options combined with rapidly growing electric vehicle and micromobility adoption provides an array of promising solutions for short-distance passenger travel.[29] Similarly, electrified rail can provide decarbonized transport for medium-distance passenger trips and land freight.[30] However, these solutions fail to provide alternatives for air transportation or long-distance shipping which require very high energy density fuels in order to be economically viable.[14] Liquid fuels are likely to remain the best option for these transportation modes.[14] Candidates for zero-emission liquid fuels include hydrogen, ammonia, biofuels, and synthetic hydrocarbons created by

using carbon dioxide from direct air capture as a feedstock.[14] This text will primarily focus on hydrogen, which is currently experiencing heightened interest on a global scale.[31]

Although hydrogen is a zero-emission fuel at point-of-use, the processes used to produce hydrogen often involve greenhouse gas emissions.[32] A color-coded system has been developed to describe the carbon intensity of producing hydrogen fuel, although some categories are not yet well-defined.[33] The most carbon intensive is brown hydrogen, which is produced through coal gasification.[33] Slightly less intensive gray hydrogen is produced by steam-reforming methane, which is currently the cheapest and most common method of hydrogen production.[33] Blue hydrogen results from steam-reforming methane when the carbon emissions are captured and sequestered as part of the production process.[33] Green hydrogen results from using renewable energy sources to split water molecules, and is the lowest carbon-intensity production process.[33] Thus, green hydrogen is the goal for future sustainable fuel systems.

1.3 Solar Fuels Devices

Photoelectrochemical (PEC) solar fuels devices offer a way to achieve artificial photosynthesis, or the direct conversion of solar energy into chemical fuels.[34–36] Thus, they offer a zero-emission method of producing fuels such as green hydrogen that are needed to support full decarbonization of transportation and provide long-duration storage in electricity systems.[14,20] These fuels also offer a lower cost method of transporting energy compared to electricity.[37] Although PEC devices have been developed to generate multiple types of fuels, this text will focus on water splitting to produce hydrogen.

PEC water-splitting devices primarily consist of light-absorbing photoelectrodes in an aqueous electrolyte, with catalysts to promote the desired reactions and a membrane to separate the gaseous products.[35] Although each of these components are active areas of research, here we focus specifically on semiconductor photoelectrodes as light-absorbers. A brief explanation of semiconductors in PEC's is provided here, but for a more thorough treatment, readers may consult Refs [36,38–40].

Semiconductors are characterized by electronic bands separated by gaps. The highest energy band filled with electrons is called the valence band (VB), the lowest energy unfilled band is called the conduction band (CB), and the difference between the two is known as the band gap (E_g). Incident photons with sufficient energy greater than the band gap may be absorbed, thus promoting an electron to the conduction band and leaving behind a hole in the valence band. Photons with energy less than the band gap are transmitted through the semiconductor rather than being absorbed.

In a PEC device, the electrons and hole pairs generated by photon absorption can be transported to the semiconductor-liquid junction to run a chemical reaction or to an ohmic back contact to connect through an external circuit to a counter-electrode. This flow of charge carriers is known as the photocurrent. A PEC device schematic showing light absorption in semiconductor photoelectrodes and the water-splitting half-reactions driven by the resultant photocurrent is provided in Figure 1.5.

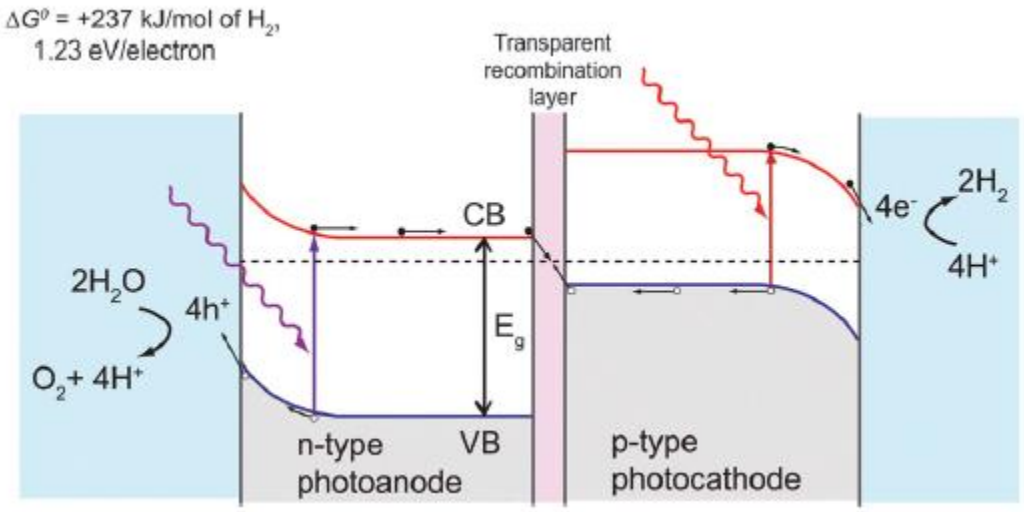

Figure 1.5 Schematic of a tandem PEC water-splitting device. Reproduced from Ref.[1] with permission from The Royal Society of Chemistry.

The device in Figure 1.5 shows half-reactions typical of operation in an acidic environment:

$$4H^+ + 4e^- \rightarrow 2H_2 \qquad (1)$$

$$2H_2O \rightarrow O_2 + 4H^+ + 4e^- \qquad (2)$$

where equation (1) is known as the hydrogen evolution reaction (HER) and equation (2) is known as the oxygen evolution reaction (OER). In an alkaline environment, the HER and OER would be represented by equations (3) and (4), respectively:

$$4H_2O + 4e^- \rightarrow 2H_2 + 4OH^- \qquad (3)$$

$$4OH^- \rightarrow O_2 + 4H_2O + 4e^- \qquad (4)$$

In order for these reactions to occur spontaneously, the semiconductor must meet several conditions. The potential of the conduction band edge at the semiconductor-liquid junction must be more negative than the proton reduction potential for HER. The potential of the valence band edge must be more positive than the water oxidation potential for OER. That is, the semiconductor must have a bandgap $E_g > 1.23$ eV to overcome the thermodynamic potential difference for water-splitting (1.23 V in standard conditions), and the band edges must be aligned properly. This is difficult to achieve with a single material, and those with a wide enough bandgap to do so usually suffer from inefficient light absorption. Many devices combine two different light absorbing materials to create a tandem device instead of relying on a single material, as seen in Figure 1.5. This can supply the necessary band placements while improving the efficiency of light absorption. When a wide bandgap semiconductor and a narrow bandgap semiconductor are combined, low energy light will transmit through the wide bandgap material and be absorbed by the narrow bandgap material. This allows the device to absorb a greater portion of the solar spectrum with less energy lost to thermalization. This thesis investigates a range of semiconductor materials (silicon, GaAs, InP) in terms of their use in solar fuels devices based on previous studies showing their potential to enable highly optimized tandem light-absorbing devices.[41]

1.4 Scope of Thesis

This thesis contributes to efforts to reach net-zero emissions with a focus on energy generation and storage in solar-based technologies, including the production of green hydrogen as an energy carrier derived from solar. Chapter 2 compares failure mechanisms in microwire-based solar fuel device architectures where the wires are removed from substrate and embedded in a membrane or left on the substrate. We demonstrate that both systems exhibit top-down and bottom-up corrosion and identify the primary corrosion pathways for each. Chapter 3 presents fabrication methods for high-efficiency light absorbing nanowires made from III-V semiconductors. Chapter 4 uses a macro-

energy systems model to analyze the role of concentrated solar power with thermal energy storage compared to solar photovoltaics with batteries in a renewable electricity grid across the United States. We demonstrate that concentrated solar with thermal energy storage plays a limited role adding flexibility to a renewable system, but its use is limited by high concentrated solar generation costs and rapidly decreasing battery costs. Chapter 5 concludes with a summary and outlook for future work in these areas.

Chapter 2

CORROSION PATHWAYS IN SILICON MICROWIRE SOLAR FUELS DEVICES

Kennedy, K. M.; Kempler, P. A.; Cabán-Acevedo, M.; Papadantonakis, K. M.; Lewis, N. S. Primary Corrosion Processes for Polymer-Embedded Free-Standing or Substrate-Supported Silicon Microwire Arrays in Aqueous Alkaline Electrolytes. *Nano Lett.* **2021**, *21* (2), 1056–1061. https://doi.org/10.1021/acs.nanolett.0c04298.

2.1 Introduction

Arrays of micro- or nano-wires embedded in a gas-blocking, ionically permselective membrane are a promising approach to full constructs for solar fuels generation.[34,42–45] Light absorbers structured into microwires have several advantages relative to planar photoelectrodes, including control of the density and coverage of bubbles;[46] advanced techniques for optimizing light management;[47–50] control over catalyst placement to minimize optical losses by absorbing or reflecting catalysts while maximizing catalyst activity;[51–54] and enhancements in operational stability relative to planar electrode surfaces.[15] The stability enhancements that are inherent with the microwire array design, which have allowed Si microwire arrays on substrate to continuously oxidize water to O_2 for over 600 h under simulated solar illumination,[55] have been ascribed to physical isolation between the wires in the array of defects in protective coatings. In contrast, on a planar photoelectrode surface that contains a protection layer, unmitigated pit corrosion as a result of even a single nanoscale coating defect will lead eventually to catastrophic failure of a macroscopic electrode area of the photoelectrode.[56,57]

Free-standing microwire arrays should also exhibit enhanced corrosion resistance provided that pit corrosion due to a defect in the protective coating of a light absorber cannot physically propagate to microwires that are not in electrical contact with the unprotected, corroded material. However, access of corrosive electrolyte to various locations in the membrane-embedded construct could introduce other failure modes due to weak points in the system design.[58] Herein, we have experimentally performed a detailed analysis of the physical processes that lead to failure and etching of protected Si microwire arrays both when on a Si substrate and when free-standing in an electrically

insulating polymer membrane based on poly-dimethylsiloxane (PDMS). Although Si passivates as a photoanode under illumination in most aqueous electrolytes due to oxide formation at pinhole defects in protective coatings, we have evaluated the stability and failure modes of such systems in the dark in alkaline electrolytes to obtain conditions under which Si actively etches. This process thus serves as an example of failure by pit corrosion and spreading at defective regions in protective coatings, exemplified by amorphous TiO_2 deposited by atomic-layer deposition.[57,59–61]

2.2 Experimental Methods

Silicon tapered microwire arrays with a 3 μm diameter and a 7 μm pitch were fabricated from an n-Si wafer using a previously reported ICP-RIE etching process.[46] Chips of approximately 5 cm x 2 cm were scribed from this wafer of wire arrays. The wire arrays were cleaned using a standard Radio Corporation of America (RCA) procedure, in which the samples were first cleaned in a Standard Clean 1 bath, 5:1:1 $H_2O/NH_4OH/H_2O_2$ at 80 °C for >10 min. The samples were then dipped into buffered oxide etchant (6:1 (v/v) 40% NH_4F to 49% HF; Transene Inc.) for 5 min at 20 °C, and were then removed and immediately rinsed with >18 Mohm-cm resistivity deionized water and blown dry under a stream of N_2(g). A RCA Standard Clean 2 bath, 6:1:1 $H_2O/HCl/H_2O_2$ at 70 °C for >10 min was used to remove SiO_2, Al_2O_3 and trace metal impurities. Hydrogen Peroxide 30% (w/w) Solution GR ACS was obtained from Millipore Sigma, and Ammonia solution 28.0–30.0% (w/w) was obtained from J.T. Baker. Hydrochloric Acid GR ACS 36.5–38.0% (w/w) was obtained from Millipore Sigma. All chemicals were used as received.

After cleaning, 1,000 cycles of amorphous TiO_2 were deposited, with each cycle consisting of a 0.015 s pulse of H_2O, followed by a 15 s purge of N_2 at 0.02 L min^{-1}, and then a 0.1 s pulse of tetrakisdimethylamidotitanium (TDMAT).[56] The wire arrays were then infilled with polydimethylsiloxane (PDMS) from PDMS from Sylguard® elastomer silicone base, toluene (Millipore Sigma ≥ 99.5%, GR ACS), and Sylguard® 184 silicone elastomer curing agent in a ratio of 10:10:1 by weight. After sonicating the mixture for 10 min, the chip was placed on a Laurell WS-400BZ-6NPP/LITE spin-coater, cleaned by drop casting a few drops of toluene onto the chip at 3000 rpm for 1 min, and then infilled by covering the array with the PDMS mixture followed by spin

coating at 3000 rpm for 1 min. The chips were then cured on a glass slide on a Corning PC-420D Hot Plate at 150°C for 1.5 h.

Four 1 x 1 cm chips were made following this procedure and used as prepared as "on substrate" Si tapered microwire arrays. The on-substrate samples were placed in a Falcon polystyrene petri dish, and Loctite EA9460 epoxy was used to seal all exposed edges and secure the sample to the bottom of the petri dish. Another four 1 x 1 cm chips were prepared, and a razor blade was used to peel off the wires in the PDMS membrane to produce free-standing films comprised of Si microwire arrays in PDMS. The bottom of four Falcon polystyrene petri dishes was covered with a 10:10:1 mixture by weight of polydimethylsiloxane (PDMS) from Sylguard® elastomer silicone base, toluene (Millipore Sigma ≥ 99.5%, GR ACS), and Sylguard® 184 silicone elastomer curing agent, and cured on glass slides using a VWR hot plate at 75°C for 24 h. The four free-standing samples were placed in these petri dishes, and again were placed on glass slides on a VWR hot plate at 75 °C for 1 h to bind the PDMS layers and create fully membrane-embedded, free-standing wire arrays.

Fifty milliliters of 1.0 M KOH(aq) (Sigma-Aldrich ≥85% KOH basis, pellets) was prepared and poured into each of the 8 petri dishes, such that each sample was well covered by the liquid. All samples were then left in the dark, with pairs of one on-substrate sample and one free-standing sample removed after 24 h, 48 h, 168 h, and 240 h of immersion time. As each sample was removed, the KOH(aq) was poured out and the sample was rinsed thoroughly with 18.3 MΩ-cm deionized H_2O. The samples were then blown dry under a stream of N_2(g) and placed in a Napco 5831 Vacuum Oven for 1 h at room temperature.

Samples were imaged with an Olympus BX51 optical microscope, covering as large an area as possible that showed no obvious mechanical damage from sample handling. Additional images were taken with a Thermo Scientific Phenom Pro G2 Desktop scanning electron microscope (SEM). After immersion in KOH(aq), selected areas were milled and imaged using a NOVA 600 Dualbeam Focused Ion Beam (FIB).

3.3 Results and Discussion

Fig 2.1(a) and (b) show optical microscopy and cross-sectional SEM images of Si tapered microwire arrays. The PDMS infill completely covered the substrate and left the wire tips exposed. Prior to immersion in KOH(aq), the microwire arrays appeared uniform in color and spacing in the optical microscope.

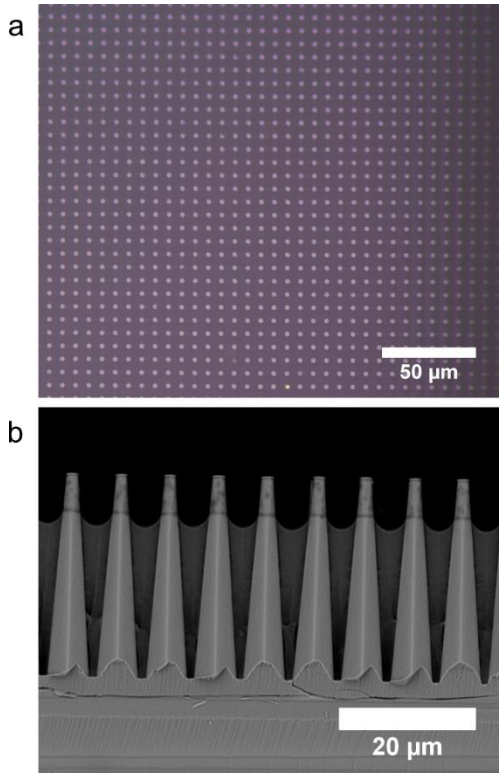

Figure 2.1 Si microwire arrays fabricated, infilled, and imaged on substrate by (a) top-down optical microscope and (b) cross-section SEM.

After immersion in 1.0 M KOH(aq), some wires in both the on-substrate and free-standing samples showed a much higher contrast in optical images than surrounding wires (Fig 2.2). Both types of samples showed increasing numbers of these high contrast wires as the immersion time increased. After 7 days in KOH(aq), the on-substrate samples exhibited substantial clustering of the high contrast wires into square arrays, as shown in Fig 2.2(e) and (g). For the free-standing samples, larger numbers of randomly located high contrast wires appeared after just 2 days of immersion in KOH(aq) (Fig 2.2(d)), with increasing numbers after 7 days in Fig 2.2(f). The high-contrast wires in

the free-standing samples were present at somewhat random locations in the array. After 10 days in KOH(aq) (Fig 2.2(h)), the free-standing sample consisted nearly entirely of medium-contrast wires that did not look like either the pre-immersion images or the high-contrast wires.

The images in Fig 2.2 are representative of the patterns observed across each sample. Figure 2.3 quantifies the variation across samples at each time of observation. The average percentage of observed high contrast wires increased with time for both on-substrate and free-standing samples. The free-standing samples showed a larger rate of increase in the average percentage, and an increase with time in the variation, of high contract wires observed across the sample. The on-substrate samples showed a slow increase in the average number of high-contrast wires, and maintained a relatively low level of variation across sample regions.

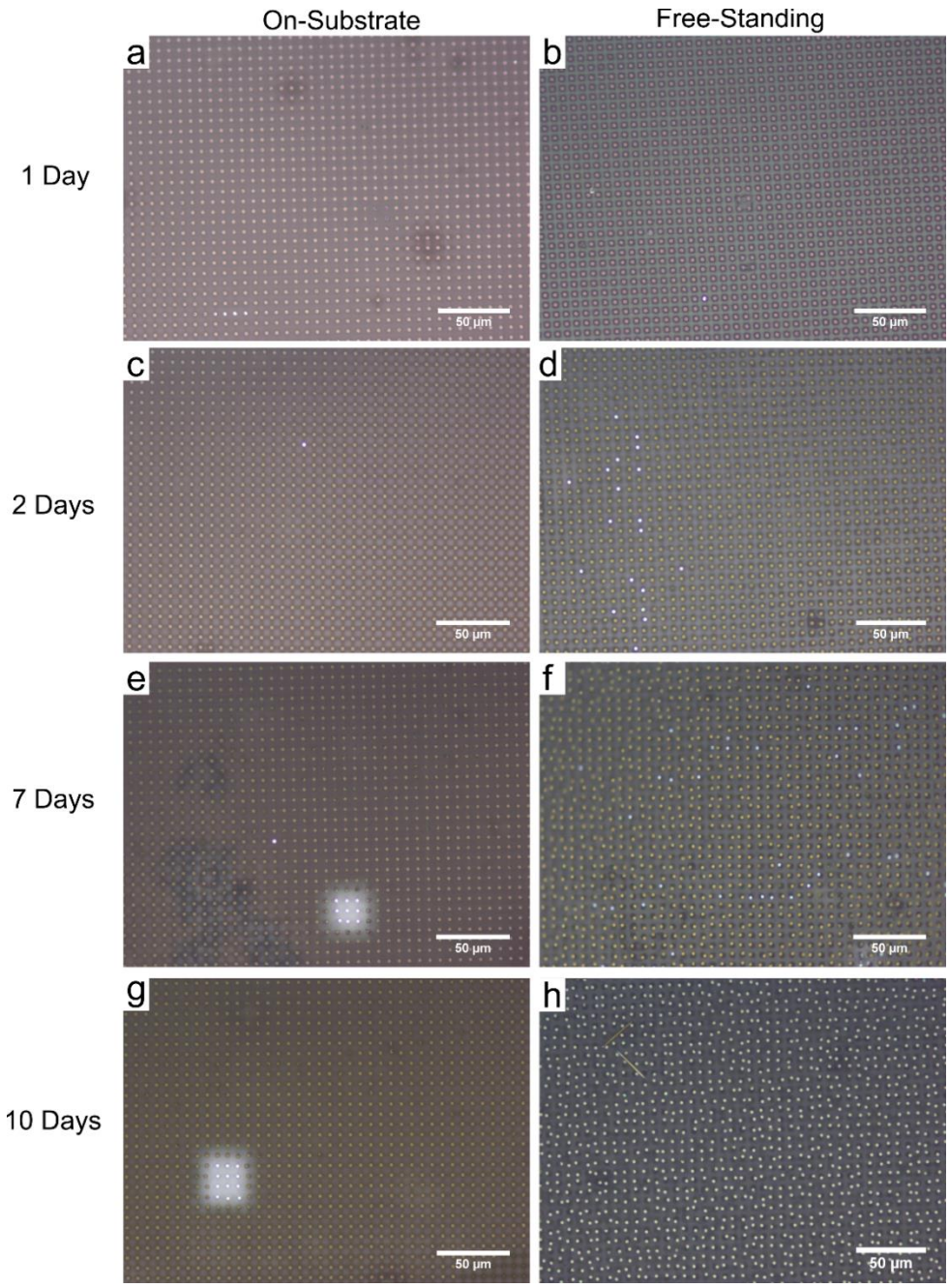

Figure 2.2 High contrast wires appear after immersion in KOH(aq). Representative images are shown of on-substrate and free-standing samples after 1 day in KOH(aq) in (a) and (b), 2 days in KOH(aq) in (c) and (d), 7 days in KOH(aq) in (e) and (f), and 10 days in KOH(aq) in (g) and (h), respectively.

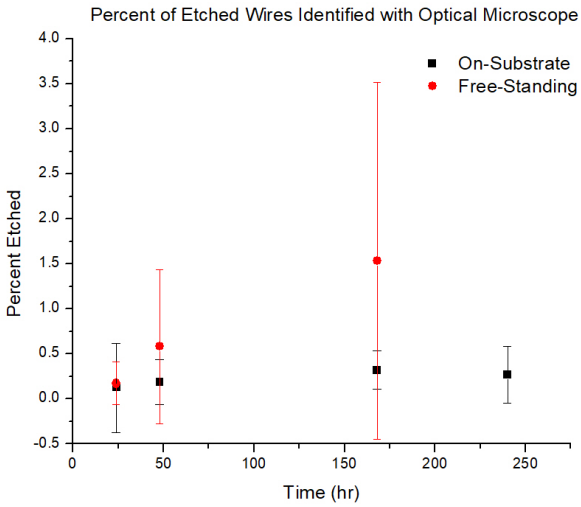

Figure 2.3 Percent of etched wires seen with the optical microscope, with averages given across multiple fields of view in the optical microscope. These data do not take into account incomplete bottom-up etching, which cannot be seen optically. A data point is not given for the free-standing sample after 248 h in 1 M KOH(aq) because no unetched wires were observed.

Focused ion-beam (FIB) milling was used to investigate the different types of wires that were observed by optical imaging. Fig 2.4(a) shows an optical image of the free-standing sample after 1 day of immersion in KOH(aq), with an area of interest indicated by a box around a set of bright and dark wires. Fig 2.4(c) shows SEM images of the same wires in cross-section, showing that the Si had begun to corrode from the top-down inside a shell of TiO_2 in the two high contrast wires. The middle darker wire was also milled, and did not show corrosion. Fig 2.4(b) and Fig 2.4(d) both show cross-sections of dark wires on the same sample, which confirmed solid silicon cores in the wire tips for wires that are exposed, and wires in which the PDMS reached nearly to the wire tip. The wire in Fig 2.4(d) was milled deeper into the PDMS layer, and the circled area revealed bottom-up corrosion even on wires that appeared pristine at their tips. This bottom-up corrosion thus resulted from KOH traveling through the PDMS backing on the free-standing wires.

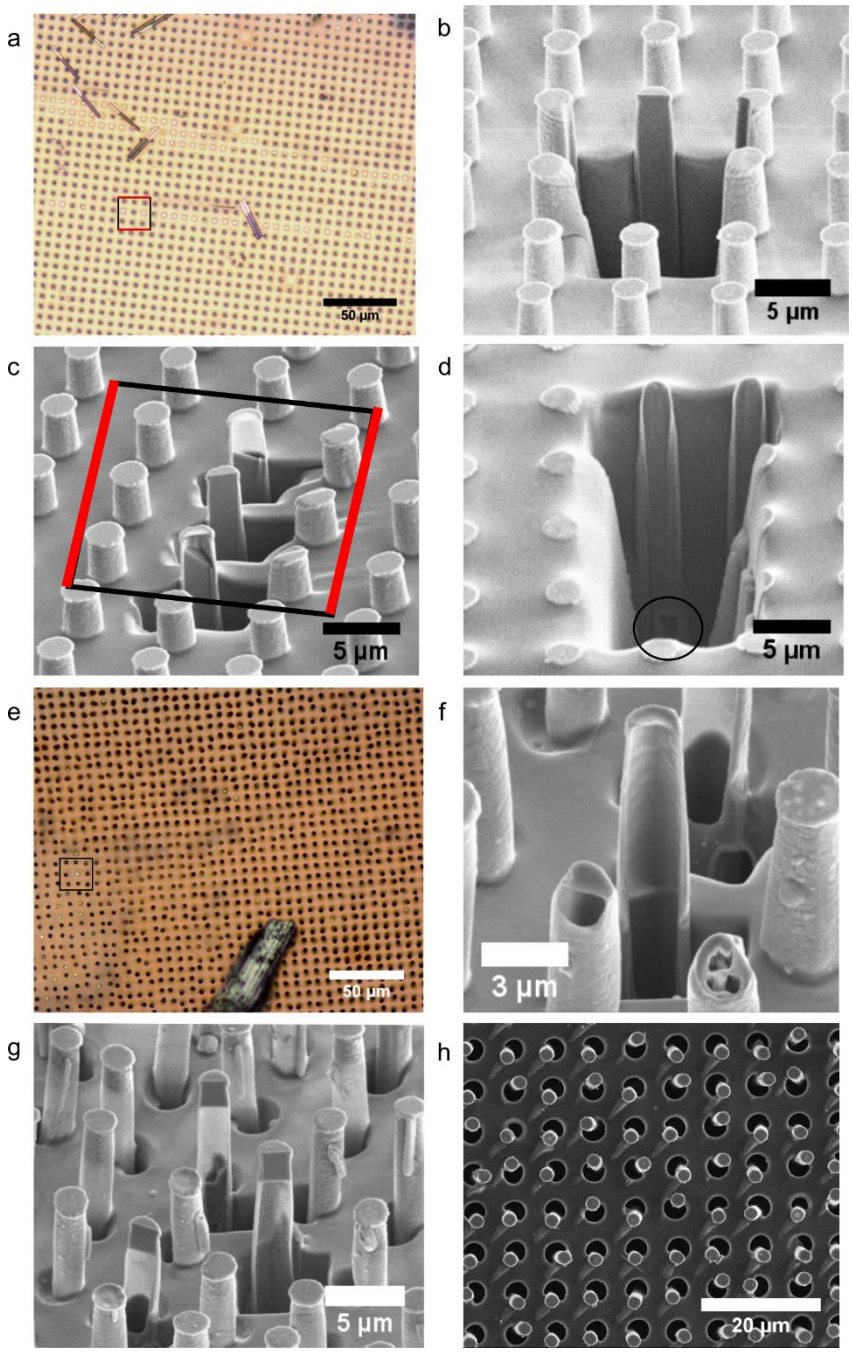

Figure 2.4 Free-standing microwire array after 1 day in KOH(aq) shown in (a)-(d). The optical image in (a) and milled cross-section in (c) show the same wires indicated by a box, with colored edges to indicate orientation relative to the bright contrast wires. (b) and (d) show shallow and deep cross-sections respectively of dark contrast wires, with the circled area in (d) showing bottom-up corrosion. Free-standing microwire array after 7 days in KOH(aq) shown in (e)-(h). The box in the

optical image in (e) indicates the location of the bright contrast wire cross-section in (f), and the dark contrast wire cross-sections in (g). (h) is a top-down SEM view of the wire array.

After 7 days in KOH(aq), this process of bottom-up corrosion in free-standing wires was more visible in cross-section. The optical image in Fig 2.4(e) shows a boxed area of interest that was examined with FIB in Fig 2.4(f) and Fig 2.4(g). The high-contrast wire from the center of the area was completely hollow, as seen in Fig 2.4(f). The dark contrast wires in the box, seen in Fig 2.4(g), experienced advanced bottom-up corrosion with only a small amount of silicon still present in the wire tips. These cross-sections demonstrate that high contrast in the optical images only identifies corrosion in the wire tip, and does not provide information about the extent of bottom-up etching. Gaps between the wires and membrane were also prevalent throughout the free-standing samples after 7 days in KOH(aq), as seen in Fig 2.4(h). These membrane channels provided another pathway for KOH to attack the sides and bottoms of the wires, contributing further to bottom-up corrosion.

Fig 2.5 shows an optical image (a) of an on-substrate sample after 10 days in KOH(aq) matched in (b) with the milled SEM image of the same area marked by the black boxes. The high-contrast wires in the optical image are matched to hollow shells of TiO_2 (locations 2–4, 6–8, 10–12) in the SEM. Further, the corrosion appeared to be progressing down the hollow wires (2–4, 6–8, 10–12), and then corroding the adjacent wires 5 and 9 in a bottom-up process. A pair distribution function analysis of optically identified top-down corroded and completely bottom-up corroded wires (Fig 2.6) showed that such wires were randomly spaced in free-standing samples, but tightly clustered in on-substrate samples. The clustering of corrosion on-substrate indicates that the corrosion spread from an initial defect to adjacent wires. Both types of samples had a membrane infill, but only the substrate samples exhibited this effect, consistent with the hypothesis that the spread occurred primarily through the substrate as opposed to through the membrane and sides of the wires. The identification of this corrosion with optical microscopy after 7 days of immersion indicates that the bottom-up corrosion process progressed more rapidly through this substrate pathway than through the membrane in the free-standing samples, for which complete bottom-up corrosion was not observed until 10 days of immersion. The membrane provided uniform access for corrosion across the sample whereas the

substrate corrosion started locally and spread, resulting in solid wires remaining after 10 days of immersion for on-substrate wires, but none remained in the free-standing membrane.

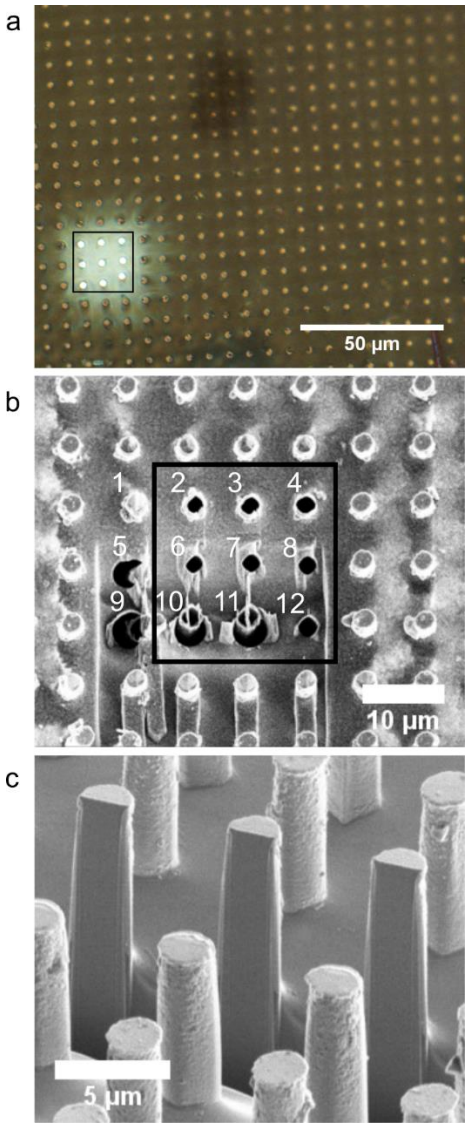

Figure 2.5 Optical (a) and milled SEM (b) image of on-substrate sample after 10 days in KOH(aq), with the same wires indicated by the black box. A milled cross-section of optically dark contrast wires on substrate is shown in (c).

In Fig 2.5(b), wires numbered 5 and 9–11 exhibited a gap between the wire and the membrane. Such membrane channels were observed in all areas where bottom-up corrosion was confirmed with FIB,

although there was not a 1:1 ratio between bottom-up etched wires and membrane channels. However, this gap feature could be used with the FIB to predictively find areas of wires where bottom-up etching had occurred, even when no identifying markers could be seen in the optical images. This behavior suggests that the membrane channels may have contributed to accelerating bottom-up corrosion of wires, in accord with the observations in the free-standing samples. Fig 2.5(c) shows the uncorroded cross-sections of several wires on the same sample that showed dark contrast under optical microscopy and did not have nearby membrane channels.

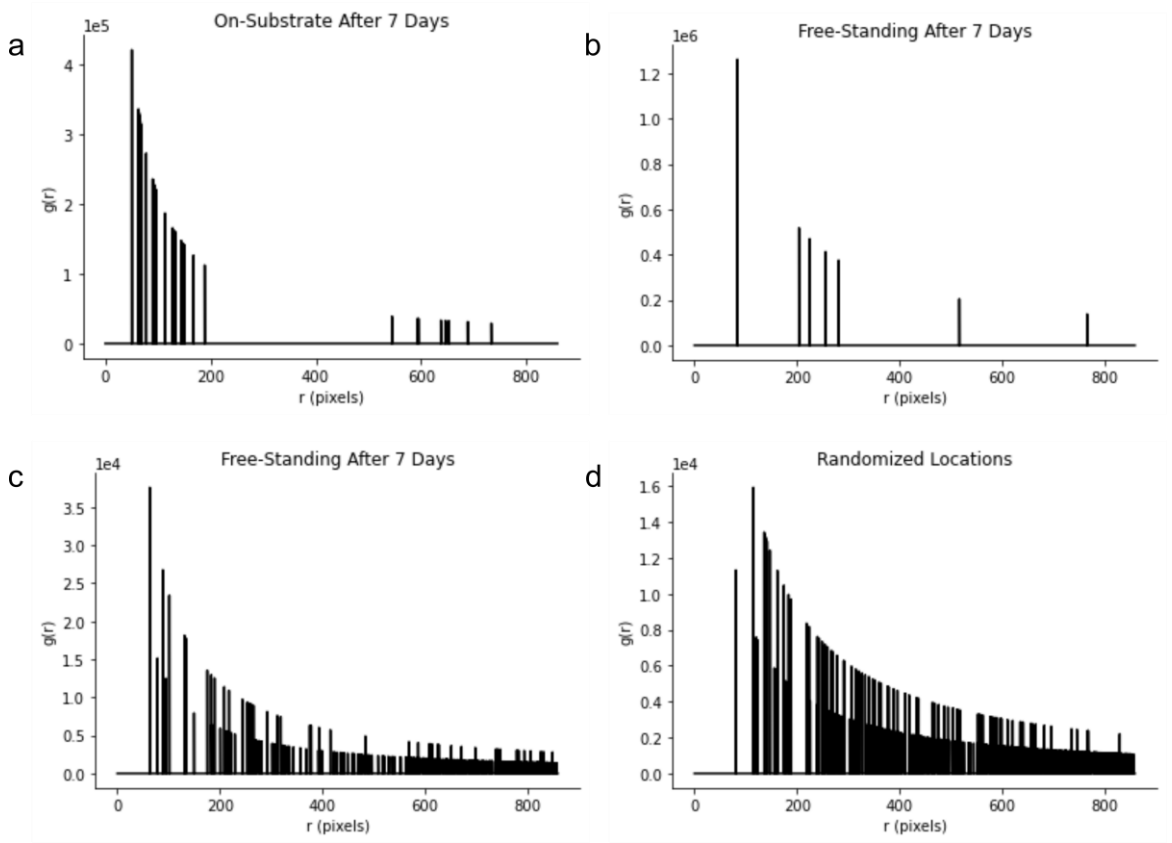

Figure 2.6 Pair distribution functions (PDFs) for etched wires identified in optical images for an on-sample (a) and free-standing sample (b) after 7 days in 1 M KOH(aq). Panel (c) shows the PDF for the free-standing image with the most optically visible etched wires, compared to a random distribution of the same number of wires in (d). The optical images used to generate panels (b) and (c) were taken from different locations on the same sample.

These samples demonstrate the different primary modes of failure for the different constructs that incorporate microwire arrays. The on-substrate samples exhibited a corrosion pathway that appears to begin with a top-down etching process through a failure in the TiO_2 protective layer. The corrosion then continues through the substrate and etches adjacent wires in a bottom-up process. This process created arrays of adjacently etched wires, with the extent of the etched wire arrays increasing with time, provided that the sample remained in KOH(aq), as shown by the group of etched wires in Fig 2.4(c). In contrast, the free-standing samples appeared to corrode primarily through channels in the membrane. Top-down etching was observed, but bottom-up etching was the dominant corrosion pathway and caused uniform etching across the sample such that after 10 days in KOH(aq), no wires were found to contain silicon. These pathways are summarized in Figure 2.7.

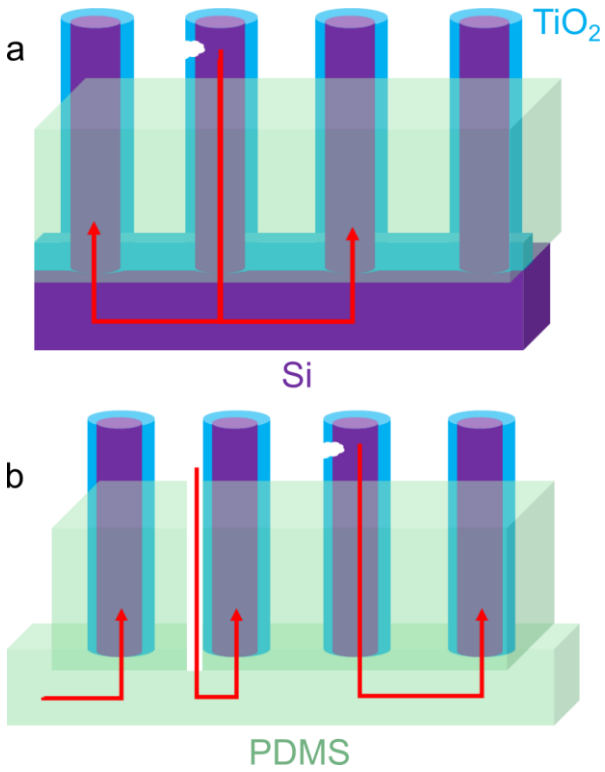

Figure 2.7 Corrosion pathways for on-substrate (a) and free-standing (b) samples indicated by arrows.

To mitigate these corrosion processes for on-substrate samples, the corrosion pathway between the wires and substrate would need to be effectively blocked. In the free-standing sample, the wires are

separated from the substrate, so a more stable membrane in alkaline conditions is required. The uniformity of the bottom-up corrosion process across the free-standing samples suggests that sealing the membrane to a polymer backing is not sufficient, therefore a more robust barrier is required on the backs of the free-standing microwires. These observations have implications for proposed device designs that consist of dual microwire arrays embedded in a polymer matrix. A possible method of blocking the bottom-up corrosion pathway for the free-standing sample would involve deposition of a thin ALD TiO_2 layer on the backside of the wires after the wires have been removed from the substrate. Additionally, other device designs with membrane-embedded wires such as membrane-embedded core-shell wires could facilitate mitigation of this corrosion pathway through strategies such as using continuous catalyst layers to seal the backs of the wires exposed by the membrane.

3.4 Conclusions

The primary failure modes identified herein demonstrate the utility of classical techniques of failure analysis and corrosion science to systematically identify corrosion pathways that need to be addressed in on-substrate and free-standing samples to ensure a long-lasting device. Although the corrosion process was studied in the dark in KOH(aq) in the absence of a protective electrolyte,[62] analogous failure modes are expected for example at pinholes in protective coatings for Si microwire arrays experiencing light/dark illumination cycles in KOH(aq). Further research is needed to determine the efficacy of mitigation strategies for these processes, with mitigation approaches designed systematically and assessed quantitatively in view of the failure modes identified herein for various candidate device architectures and materials combinations.

Chapter 3

FABRICATION OF III-V NANOWIRES FOR LIGHT ABSORPTION

3.1 Introduction and Motivation

Photoelectrochemical devices offer one way of producing green hydrogen as a zero-emission fuel.[35,36] In order to compete with cheap solar photovoltaics and electrolyzers, they must achieve high solar-to-hydrogen efficiencies.[35,63,64] In pursuit of this goal, tandem devices pairing a wide bandgap absorber and a narrow bandgap absorber have been proposed to capture a greater range of the solar spectrum.[41,65] Modeling of such devices suggests that they are capable of reaching nearly 30% solar-to-hydrogen efficiency, as seen in Figure 3.1.

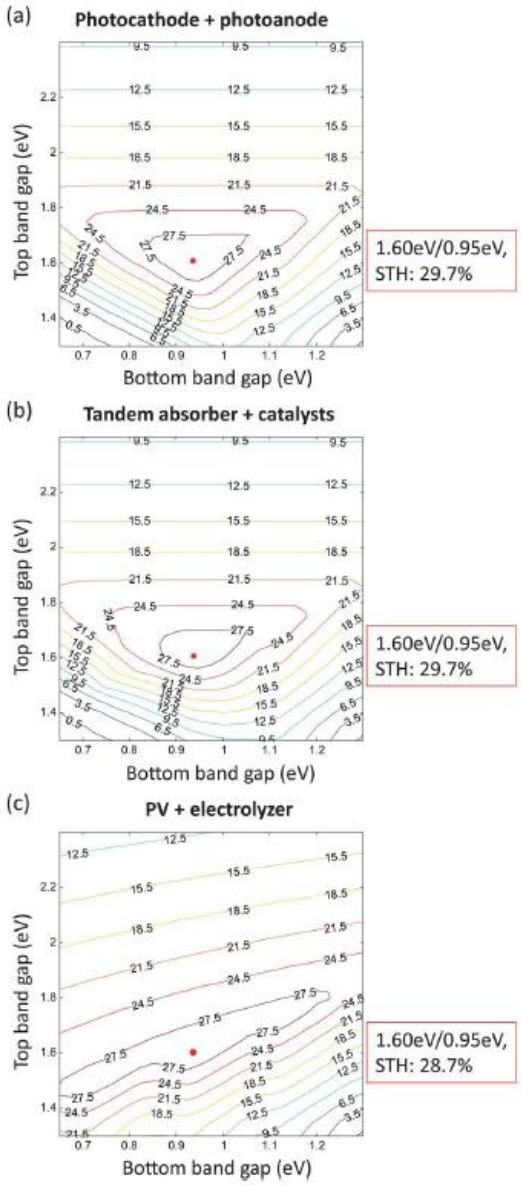

Figure 3.1 Iso-efficiency plots showing the STH efficiency limits for (a) a photocathode + photoanode PEC, (b) a tandem absorber + electrocatalyst PEC, and (c) a two-junction PV + electrolyzer. In (a) and (b), Pt and RuO_2 were chosen as the HER and OER catalysts, the light absorber had FF = 0.85, and the solution resistance was 5 ohm cm^{-2}. In (c), the electrolyzer efficiency was taken to be 73%. Reproduced from Ref.[41] with permission from The Royal Society of Chemistry.

However, even greater efficiencies may be possible by taking advantage of nanoscale optical properties in direct bandgap III-V semiconductors. Fountaine et al. simulated the optical properties of nanostructured GaAs using finite difference time domain (FDTD) methods and found that truncated nanocones exhibited highly localized absorption modes tied to the radii of the wires that were capable of capturing nearly the entire visible spectrum of light, as seen in Figure 3.2.[2] Similar results have also been shown for arrays of nanowires with multiple different radii.[2,66,67]

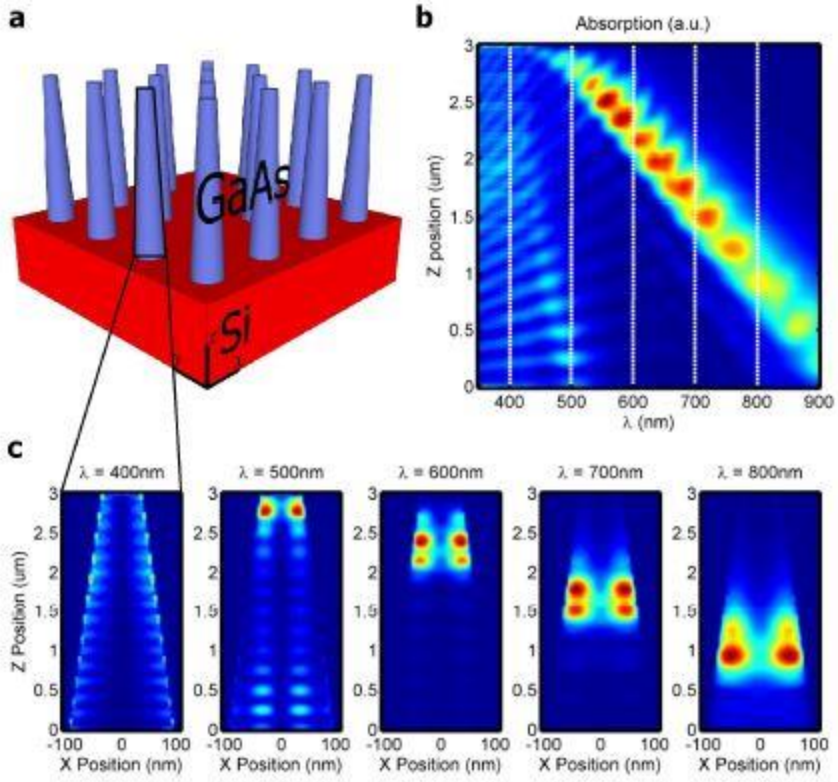

Figure 3.2 Light absorption in nanocones. (a) Array of optimized GaAs truncated nanocones with tip radii of 40 nm, base radii of 100 nm, and heights of 3 μm, labeling *x*, *y*, and *z* dimensions and indicating the vertical cross section shown in (c); (b) Absorption in a single truncated nanocone integrated over *x* and *y*, its radial cross section, (red indicating strong absorption and blue indicating little to no absorption) as a function of both wavelength and position along the z axis (labeled in a); (c) *xz* (vertical) cross sections of absorption for a single nanocone illuminated at wavelengths of 400, 500, 600, 700, and 800 nm. Reprinted with permission from Ref [2] © OSA Publishing.

Here, we report fabrication methods for generating nanostructured GaAs and InP that can be adapted to realize the above benefits in future devices. These structures were achieved through a top-down process using e-beam lithography and an inductively-coupled plasma reactive-ion etcher (ICP-RIE).

3.2 GaAs Nanostructure Fabrication Methods

E-beam resist (MicroChem 950 PMMA A3) was spincoated onto a GaAs wafer at 3000 rpm for 1 minute to obtain a 100 nm thick layer, then cured for 5 minutes at 180 °C. Arrays of circles with 300 nm diameters and 2 micron center-to-center pitch were made in AutoCAD and fractured in Layout BEAMER. A Raith Electron Beam Pattern Generator (EBPG) 5000+ was used to write the patterns, with a 5 nA beam and 900 $\mu C/cm^2$ dose, at 100 kV. After patterning, the resist was developed by immersion for 50 seconds in a solution of 1:3 ratio by volume of Methyl IsoButyl Ketone (J. T. Baker, >90% purity) to Iso Propyl Alcohol (VWR, 99.5% purity). Development was stopped by immersion in Iso Propyl Alcohol (IPA), and the wafer was dried with a nitrogen gun.

Next, the sample was placed in a CHA Mark 40 electron beam evaporator. The chamber was pumped down to 4.0e-6 Torr, and 15 nm of aluminum + 50 nm of chromium were deposited. The aluminum layer was added to facilitate future removal of the metals,[68] while the chromium acted as a hard mask for the etch step. The sample was then submerged in acetone, sonicated for 30s, and then left in the acetone bath for 5 minutes to remove the remaining PMMA. Upon removal from the acetone bath, the sample was rinsed with IPA and blown dry with a nitrogen gun. Finally, the samples were scribed and broken into 5 mm x 5 mm chips using a Dynatex GST-150.

A GaAs etching recipe was developed using an Oxford Instruments Plasma Technology Plasmalab System 100 ICP-RIE 380 that was optimized for the etching of compound semiconductors. First, a standard cleaning recipe was used to prepare the chamber. A five minute etch with 100 sccm of O_2 at 20 mTorr, 100 W RF forward power, 2000 W ICP forward power, and 20°C, followed by a 5 min etch with 50 sccm of SF_6 at 10 mTorr, 150 W RF forward power, 1500 W ICP forward power, and 20 °C. For each etching procedure, the recipe was then adjusted to accommodate the particular chamber conditions at that time by iterating between etching test samples and imaging the test

samples with a Thermo Fisher Sirion Scanning Electron Microscope (SEM), adjusting parameters as needed to achieve the desired sidewall profile in a subsequent batch of samples.

The base recipe used to begin iterating on test samples was 10 sccm $SiCl_4$, 30 sccm Ar, and 5.0 sccm CH_4 at 2.0 mTorr chamber pressure, 80 W RF forward power, 350 W ICP forward power, and 20 °C for 13 minutes. The $SiCl_4$ acted as a chemical etchant forming partially chlorinated $GaCl_x$ and $AsCl_x$ (x = 1-3).[69] Ar increased the anisotropy of the etch through physical sputtering, and CH_4 created taper in the structure through sidewall passivation.[69] The profile of the structure could therefore be adjusted to form tapered cones, straight sidewalls, or inverted cones by adjusting the flow rates of Ar and CH_4. The steps in this GaAs fabrication process are summarized in Figure 3.3.

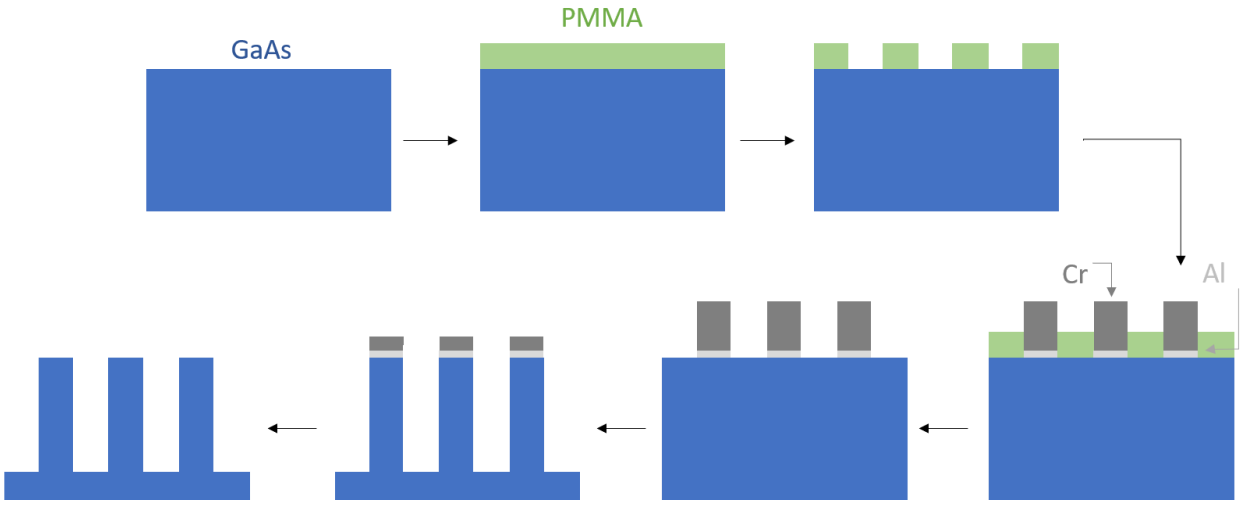

Figure 3.3 Process for top-down fabrication of GaAs nanowires.

Figure 3.4 shows representative samples created with these recipes. The nanocones in (a) were produced by 30 sccm Ar, 10 sccm $SiCl_4$, and 5 sccm CH_4, with 80 W RF forward power, 350 W ICP forward power, 2 mTorr chamber pressure, at 20 °C for 5 minutes. The inverted cones in (b) were produced by 30 sccm Ar, 10 sccm $SiCl_4$, 0 sccm CH_4, with 80 W RF forward power, 350 W ICP forward power, 2 mTorr chamber pressure, at 20 °C for 5 minutes.

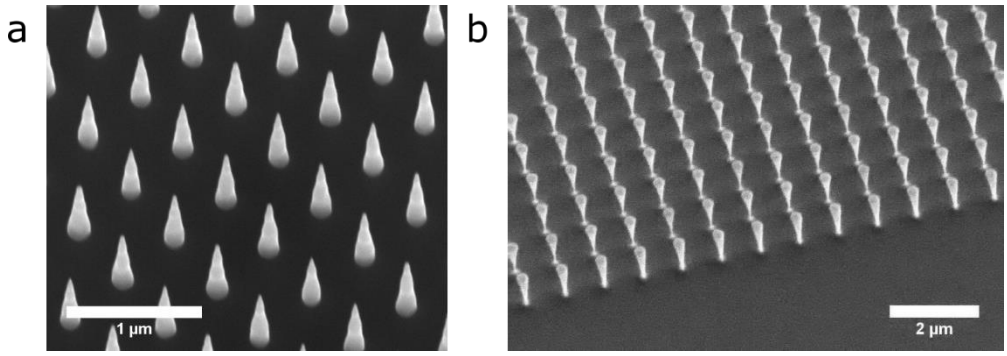

Figure 3.4 SEM of GaAs nanocones in (a) and inverted nanocones in (b).

This procedure resulted in nanostructures up to ~1.6 microns tall, with base radii varying from 200-300 nm. To achieve the optimal structures shown in Figure 3.2, higher-aspect ratio wires are still needed. Using thicker mask layers, longer etch times, and increasing the anisotropy of the etch by increasing the flow of Ar can help obtain improved structures.

3.3 InP Nanostructure Fabrication Methods

The e-beam patterning procedures for InP were the same as described above for GaAs. A mask of 50 nm of Cr was then deposited using the parameters described for GaAs above. The etch for InP structures was adapted from the process described in Foutaine et al.[66] The base recipe was 32 sccm Cl_2, 5.0 sccm H_2, and 18 sccm CH_4, at 4.0 mTorr chamber pressure, 200 W RF forward power, 2200 W ICP forward power, and 60 °C for 2 minutes and 30 seconds. Test samples were used to iterate on H_2 and CH_4 gas flow rates and etch time to achieve optimal results. Higher H_2 flows yielded straight sidewalls while less H_2 and more CH_4 yielded tapered cones. The etch time was varied to etch through the sacrificial mask while maintaining the tallest possible features. Figure 3.5 shows representative samples of such recipes. The straight sidewalls in (a) were produced by 32 sccm Cl_2, 28 sccm H_2, and 18 sccm CH_4, with 200 W RF forward power, 2200 W ICP forward power, 61 °C, and 4 mTorr chamber pressure for 3 minutes. The nanocones in (b) were produced by 32 sccm Cl_2, 5 sccm H_2, and 18 sccm CH_4, with 200 W RF forward power, 2200 W ICP forward power, 61 °C, and 4 mTorr chamber pressure for 2 minutes and 30 seconds.

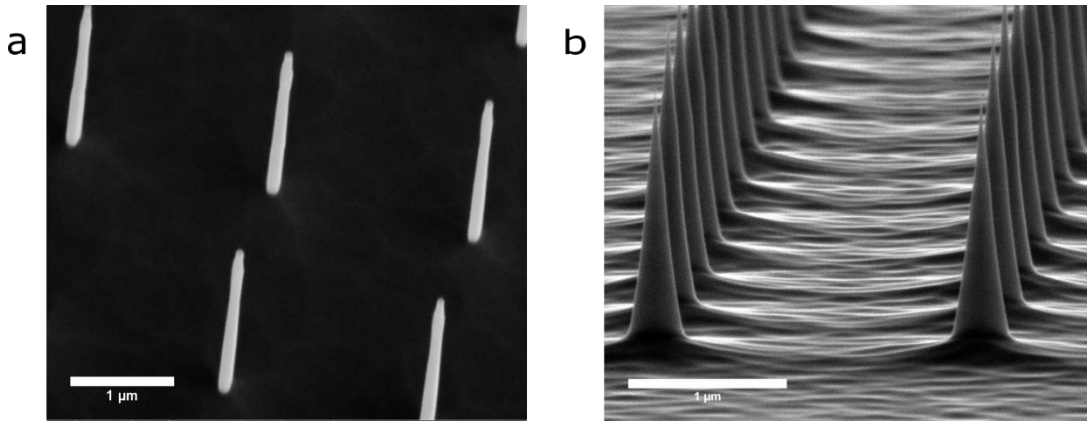

Figure 3.5 Tilted SEM image of InP nanowires with straight sidewalls in (a), and cross-section SEM of InP nanocones with tapered sidewalls in (b).

3.4 Future work

These fabrication recipes represent a foundation for many future research paths. First, more extensive characterization should be done to determine optical absorption performance of these samples. UV/Vis spectroscopy offers an obvious first step. Next, charge-carrier generation in the nanostructures could be examined using a similar approach to previous work by Dasog et al., where photoelectrochemical deposition of gold nanoparticles was used to observe the charge-carrier generation profile in silicon microwires.[70] This approach could provide experimental confirmation of the absorption patterns simulated by Fountaine et al. shown in Figure 3.2.[2] If good optical performance is confirmed by these methods, then further work could be done to integrate these samples into solar water-splitting devices.

One proposed device design for nano- and micro- wire light absorbers is a tandem device with top and bottom wire arrays connected by an ion exchange membrane.[34] While a procedure for embedding microwires in a membrane is well-established,[71] more work is needed to determine the best way to integrate nanowires, which necessitate far thinner membrane layers. Spincoating techniques allow for polymer layers on the order of 100s of nanometers, but removing such thin layers from a substrate is extremely difficult. One way to avoid this problem could be to create a polymer layer several microns thick, assemble the device using this thick layer, and then ablate the polymer by sputtering until the nanowires are exposed. Other device designs such as membrane-

embedded core-shell wires could also bypass this issue by allowing for light-absorption through a thick transparent membrane while using a continuous catalyst layer on the backs of the wires to create the solid-liquid junction needed to run the desired reactions.

Chapter 4

THE ROLE OF CONCENTRATED SOLAR POWER IN ENERGY SYSTEMS

4.1 Introduction

The United States is setting more ambitious renewable energy goals each year, with 30 states and 3 territories adopting renewable portfolio standards, including eight with 100% renewable electricity generation targets.[72] Dozens of other cities and counties have also committed to 100% renewable energy goals.[73] These policies necessitate greater use of variable renewable energy (VRE) sources, which introduces new challenges to satisfy goals and requirements for grid reliability.[15] The North American Electric Reliability Corporation (NERC) resource adequacy planning standard specifies that hourly averaged electricity demand must be met in full except for, at most, one hour in a decade.[15,74] Given that historical weather data shows the dominant VRE generation technologies, solar photovoltaics (PV) and wind turbines, can likely only meet ~80% of US electrical demand reliably without auxiliary technologies and/or extensive curtailment,[15] methods of improving grid flexibility and dispatchability are important to cost-effectively implementing VRE technologies while maintaining resource adequacy.

Full decarbonization of 100% VRE-based power grids is challenging because compensation for the variability of generation cannot be performed by dispatchable fossil fuel generation, specifically natural gas generators.[16] Without firm generators, increased long-distance transmission to connect variable renewable resources across wide geographies can reduce, but not eliminate, the resource variability. Strategies to reliably meet demand include overbuilding of generation capacity while incurring substantial curtailment of generation; cross-sector couplings to enhance flexibility; extensive demand management; and/or grid-scale energy storage technologies.[16,21] Long-duration seasonal storage can substantially decrease the cost of idealized 100% reliable electricity systems based on 100% VRE generation.[20] However, short-duration storage remains a costly necessity for VRE-based grid services such as day-night cycling.

Two frequently cited options that combine VRE generation with short-term storage are solar PV with battery storage and concentrated solar power (CSP) with thermal energy storage (TES). Despite decades of commercial usage, the cost of CSP generation remains high compared to solar PV generation, which has experienced continuous, substantial cost reductions over at least two decades.[25,26,75,76] In contrast, current TES costs are low compared to storage in chemical batteries, which suggests a role for CSP+TES relative to PV+batteries, due to favorable storage costs for TES despite the disadvantage in generation costs for CSP.[24,25] Levelized costs of electricity including overnight storage for marginal addition of CSP+TES capacity are often compared favorably to levelized costs of electricity based on marginal addition of PV and overnight battery storage into existing electricity grids.[77,78]

Concentrated solar power utilizes mirrors, referred to as a "solar field," to concentrate sunlight onto receivers that contain a heat transfer fluid and generate thermal energy.[79] The heat transfer fluid can then be used to run a steam turbine and generate electricity.[79] When combined with TES, either the heat transfer fluid itself can be stored in what is known as "direct" storage, or the heat can be transmitted to another medium for "indirect" storage, allowing electricity to be generated later.[27] The four main types of CSP are Parabolic Trough Collector (PTC), Solar Power Tower (SPT), Linear Fresnel Reflector (LFR), and Parabolic Dish Collector (PDC), with PTC and SPT accounting for most of the global installed capacity.[27,79] This analysis focuses primarily on PTC because it is the most mature CSP technology.

The first commercial CSP plant was built in the US in the 1980s, and CSP has been used continuously ever since.[27] However, global CSP capacity has grown slowly over that period, with development occurring in just a few select nations.[27] CSP and TES are currently enjoying renewed interest, particularly among solar belt countries in Africa[80,81] and the Middle East,[27] as well as in China, which leads the world in planned new CSP capacity.[27] Concentrated solar power offers several potential benefits to a VRE-based electricity system. The primary advantage arises from coupling CSP with TES to provide built-in energy storage, which can substantially increase the capacity factor to > 90%.[79,82] Life-cycle analyses suggest that CSP has lower emissions than solar PV.[83,84] CSP plants can be hybridized to use biofuels, fossil fuels, or geothermal energy to drive the steam turbine when

insufficient solar energy is available.[85,86] The cogeneration of heat and electricity from CSP also provides opportunities to supply heat directly for industry, or for use in other coupled processes such as desalination.[87–89]

The impacts of CSP with TES in an electrical grid have been explored in a range of studies across a variety of geographical areas.[80,90–95] One study on the Brazilian electricity system found that adding CSP with TES was a cost-effective way to add marginal dispatchable capacity that complemented wind and PV generation.[90] CSP+TES also added flexibility to the grid, particularly in the winter when Brazil's large hydrological resources were less available.[90] Another study similarly found that CSP improved flexibility in the Chilean electricity system, with low-cost scenarios leading to CSP with TES accounting for approximately one third of dispatched energy by 2037.[91] In the US, a study of the Western Interconnect comparing CSP+TES to renewable generators without other storage technologies found that CSP+TES could reduce the need for costly start-up and operation of high ramp-rate fossil fuel peaker plants.[96]

Studies have placed particular emphasis on the potential synergies between wind and CSP. A hybrid CSP-wind plant with TES and batteries designed to meet electrical, thermal, and transport needs was modeled for the Greek island Skyros.[92] This configuration provided better exergetic efficiency while requiring less land than the two other configurations considered – PV and wind with batteries and an electrolyzer, or PV and wind with pumped hydropower storage and an electrolyzer.[92] Another study on hybridizing wind and CSP in a Minnesota plant found that although costs at the time favored using only wind power, adding CSP provided valuable grid services by improving load-matching within the system.[93] A third study focused on the Texas panhandle, the region with the largest wind resource in Texas.[94] Extensive wind development has led to an increasingly large mismatch between demand and resource availability in the region, but a ratio of ~2/3 wind generation and ~1/3 CSP with 6 h of TES provided value by improving load-matching across the annual, monthly, and hourly timescales considered.[94] In the Andalusia region of Spain, models suggested that careful siting of wind and CSP+TES could enable baseload renewable power.[95]

The value of grid services provided by addition of marginal capacity and storage to existing grids, especially as measured by the levelized cost of marginal electricity produced into the existing grid system, may be very different than the value of different generation and storage technologies to an electricity system that is fully powered by variable renewable sources, in accord with legislation and mandates in a growing number of cities, states, regions, and nations globally. We analyze herein the role of CSP and TES in an idealized electricity system powered solely by variable renewable energy from solar and wind, using real-world historical demand and hourly weather data across CONUS. Under favorable assumptions that minimize the impacts of resource variability, specifically assuming lossless transmission from generation to load over the contiguous U.S., we assess the conditions under which CSP+TES would play a substantial role relative to other technologies such as PV and batteries in a highly reliable, least-cost electricity system. The base case technology mix modeled for our analysis includes wind, PV, CSP with TES, batteries, and power-to-gas-to-power using hydrogen gas for seasonal storage. The base case uses current asset costs, and we then parameterize costs to perform a sensitivity analysis with no bias as to actual future costs of a specific generation or storage technology.

Using a least-cost linear optimization model, our study focuses on dynamical relationships and system characteristics without attempting to predict future costs or detailed future electricity system architectures. The flexibility and low computational cost of this idealized system allows exploration of a large number of system compositions and moreover facilitates extensive parameterization of costs over a wide range of values to ascertain the robustness of our results. The breadth of analysis offered by this approach could provide potentially interesting parameter spaces for more detailed models to explore. The ability to investigate a wide range of scenarios is important due to uncertainties in cost projections for current renewable generation technologies as well as in the development of future technologies. Thus, this model provides a framework for analysis and decision-making based on fundamental trade-offs and technology niches inherent to a highly reliable, fully decarbonized, VRE-based electricity system.

4.2. Methods

4.2.1 Model Formulation, Costs, and Assumptions

This analysis was performed using an idealized macro-scale electricity system[97] represented by the Macro-Energy Model (MEM).[20,23,98] Each technology in the model was represented by a fixed cost and a variable cost. Wind, solar photovoltaic (PV), and natural gas with carbon capture and storage costs were taken from the EIA's 2020 Annual Energy Outlook and are based on current cost estimates.[99] Costs for concentrated solar power (CSP) and thermal energy storage (TES) were based on NREL's System Advisory Model 2020.2.29.[25,26,100–102] Parabolic trough collectors (PTC) were used as the base case in the model because they are the most mature CSP technology, and they allowed for facile comparison with single-axis tracking PV generation due to similar tracking geometry.[27] Solar power tower (SPT) costs were used for comparison in certain cases. Costs and technology assumptions for the generation technologies are provided in Table 4.1.

Generation Technologies	**Wind**	**Photovoltaics**	**CSP - PTC**	**CSP – SPT**	**Natural Gas**
Technology Description	Onshore wind turbines	Single-axis tracking solar panels	Single-axis tracking parabolic trough CSP	Solar power tower CSP	Combined cycle with multi shaft configuration
Total Overnight Cost ($/kW)	1319[99]	1331[99]	2383.38[100]	3432.17[100]	954[99]
Lifetime (years)	25[99]	25[99]	30[100]	30[100]	30[99]
Discount Rate	0.07	0.07	0.07	0.07	0.07
Capital Recovery Factor (%/year)	8.58%	8.58%	8.06%	8.06%	8.06%
Fixed O&M Costs ($/kW-yr)	26.22[99]	15.19[99]	67.32[100]	67.32[100]	12.15[99]
Variable O&M Costs ($/kWh)	0	0	0	0	0.00186[99]
Fuel Cost ($/kWh)	-	-	-	-	0.0191[99,103]
Annualized Hourly costs					
Fixed Cost	0.0159	0.0148	0.0296	0.0393	0.0102
Variable Cost	0	0	0	0	0.02097

Table 4.1. Model inputs for generation technologies. All cost values are represented in 2019 US dollars. Additional details provided in SI section 2.

Battery costs, capacity, and lifetimes were taken from the financial advisory firm Lazard.[104] Costs for electrolyzer facilities (stack, compressor, and balance of plant (BoP)) and power-to-gas-to-power (PGP) underground storage were based on NREL's H2A model.[105–108] Fuel cell costs were taken from the EPA's Catalog of CHP Technologies.[109] Storage technologies were assumed to be operational at all times, with costs and technology assumptions for storage provided in Table 4.2.

Storage Technologies	**Battery Storage**	**PGP Storage**	**Electrolysis Plant**	**Fuel Cell**	**TES - PTC**	**TES - SPT**
Technology Description	Li-ion battery	Underground hydrogen storage in caverns	PEM Electrolyzer plant with compressors	Molten carbonate	Two-tank indirect	Two-tank direct
Units for Capacity Costs	$/kWh	$/kg/hr*	$/kg/hr*	$/kW	$/kWht	$/kWht
Total Overnight Cost	365.77[104]	6.86[108]	63,008[108]	5000[109]	77.82[100]	27.61[100]
Lifetime (years)	10[104]	30[7]	7 stack, 40 BoP, 15 compressor[108]	20[110]	30[100]	30
Discount Rate	0.07	0.07	0.07	0.07	0.07	0.07
Capital Recovery Factor (%/year)	14.24%	8.06%	18.56% stack, 7.5% BoP, 10.98% compressor	9.44%	8.06%	8.06%
Fixed O&M Costs	12.32[104]	0.537[108]	1822.13 plant, 182.33 compressor[108]	43[109]	0	0
Efficiency	90%[104]	-	61.4%[105]	70%[109]	98.5%[100]	98.5%[100]
Self-Discharge Rate	1E-05[104]	1.14E-08[108]	-	-	3.60E-04[100]	2.9E-04[100]
Energy/Power Ratio (h)	4[104]	-	-	-	6[100]	6[100]
Annualized Hourly costs						
Fixed Cost ($/kWh, $/kW)	0.00735	0.00000373	0.0346	0.0588	0.000716	0.000254
Variable Cost	0	0	0	0	0	0

Table 4.2. Model inputs for storage technologies. All cost values are represented in 2019 US dollars. Additional details provided in Appendix A, Section A.2.

* Values /kg for H_2 storage and the electrolysis plant were converted to kWh's for model inputs using the lower heating value (LHV) of 33.33 kWh/kg for hydrogen.

The model optimized for the least-cost solution with the constraint that electrical sources and demand were balanced on an hourly basis. Directional flows for each technology are represented below in Figure 4.1. Batteries and PGP could accept inputs from any technology that supplied the main node, or electrical grid, whereas energy into TES could only be supplied by generation from CSP. A simple demand response mechanism that allows the system to supply less than the historical use profile by paying a high cost was used to represent load shedding, referred to here interchangeably as lost load.

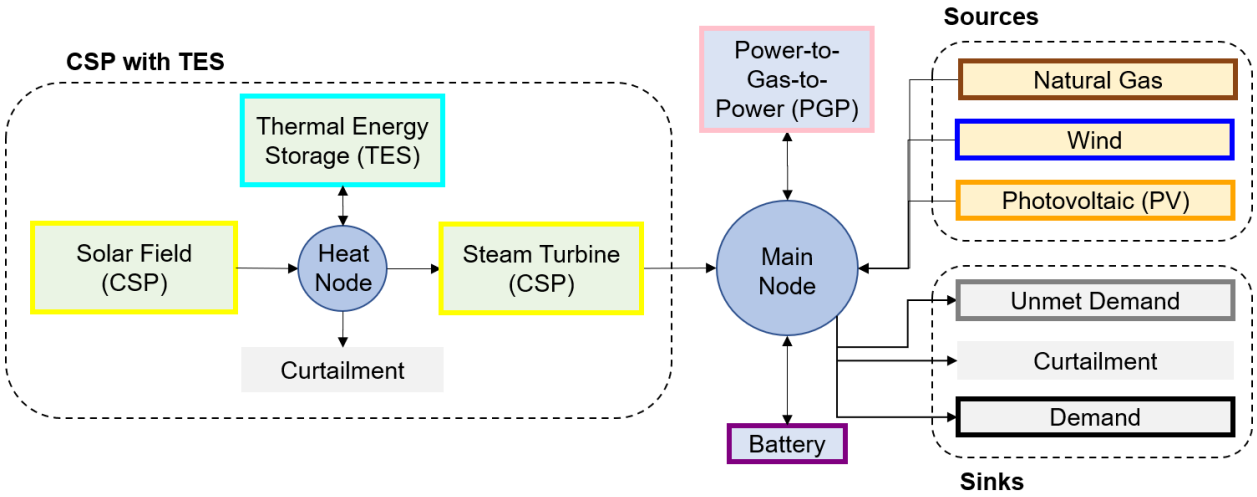

Figure 4.1. Energy flow diagram showing how technologies are connected in the Macro-Energy Model (MEM).

4.2.2 Solar and Wind Data

Hourly capacity factors for solar and wind data were generated using the Modern-Era Retrospective analysis for Research and Application, Version 2 (MERRA-2) reanalysis data.[111] These data have a grid-cell resolution of 0.5° latitude by 0.625° longitude. Solar capacity factors, used for both photovoltaics and concentrated solar power, were calculated for a single-axis tracking system capable of tilting 0°–45°. Wind capacity factors were calculated for a GE 1.6–100 turbine with a 1.6 MW nameplate capacity, using methods described in Refs.[112–114] The geographic regions with the top 25% generation potential were used to create model inputs. The base case year used for solar and wind resource data was 2017.

4.2.3 Demand Data

Demand inputs for the model were generated from hourly data drawn from balancing authorities in the contiguous US, accessed through the EIA's data portal.[115] Previously published methods were used to clean the data and replace missing values using multiple imputation by chained equations (MICE).[116] The validity of this technique was verified by testing against known values within the dataset. The mean absolute percentage error (MAPE) across all balancing authorities was calculated to be 3.5%, with a relatively small bias of 0.33%.[116] The base case year used for demand data was 2017.

4.3. Results

4.3.1 Increased Grid Flexibility through CSP+TES

Figure 4.2 shows dispatch curves in a least-cost electricity system for which the solar, wind, and storage resources were built to meet 2017 demand data on an hourly basis. Positive values indicate sources of electricity being provided to the grid, and negative values indicate sinks in which energy is flowing out of the grid. The dispatch curves represent the base case technology mix with generation from PV, wind, and CSP, and storage from batteries, TES, and PGP. The full year is shown in Figure 4.2 (a), while 4-day panels in Figure 4.2 (b-d) represent the periods of maximum hourly dispatch from each storage technology. These panels show that batteries and TES filled short-term gaps in resource that generally lasted less than 24 h, whereas PGP filled multi-day resource gaps that had a continuous deficit in generation relative to demand. CSP is used primarily to charge TES instead of directly providing electricity to the grid. Therefore, the combined impact of CSP+TES was primarily to add flexibility to the grid through TES's storage role.

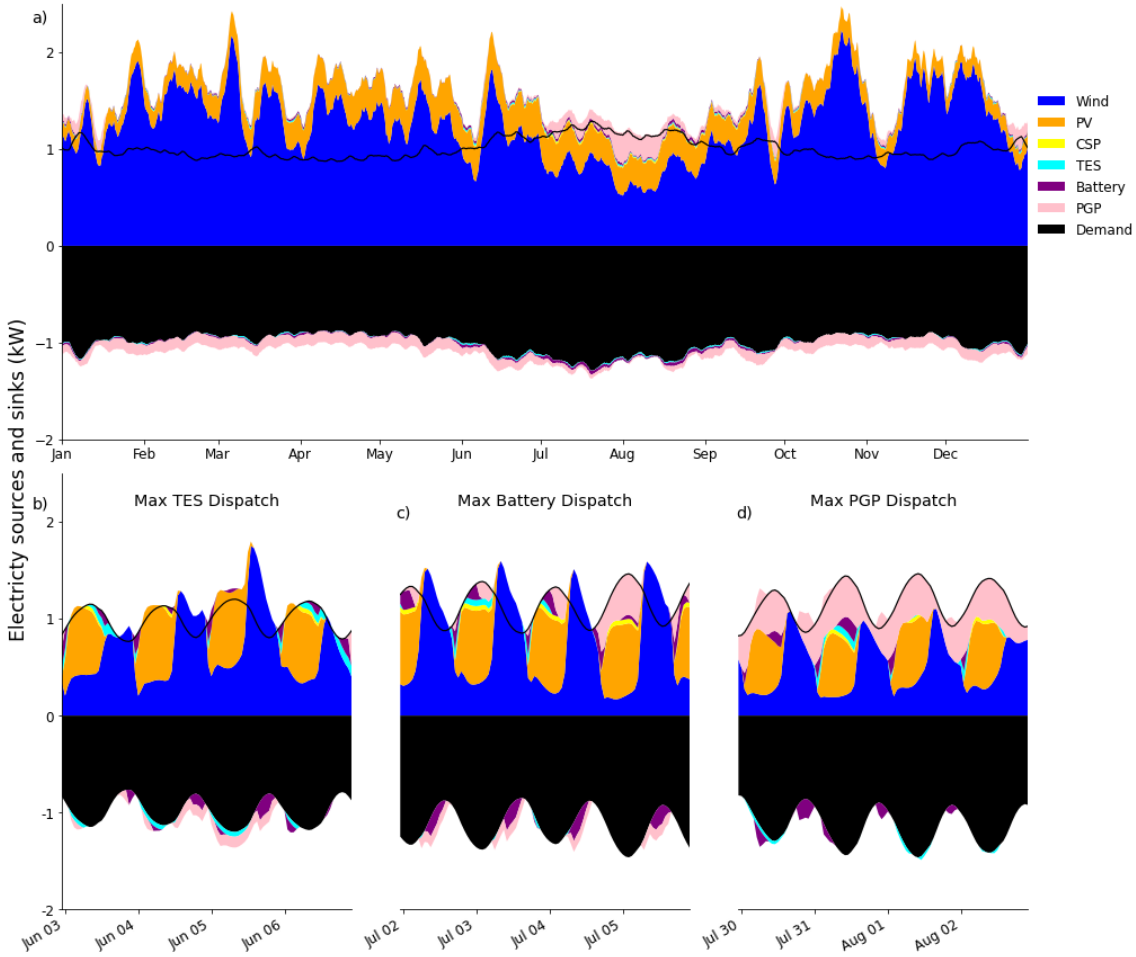

Figure 4.2. Dispatch curve for 2017 data with 5-day averaging for the base case in (a). The panels in (b), (c), and (d) show hourly dispatch for the 4-day periods of maximum dispatch from TES, batteries, and PGP, respectively. CSP+TES plays a small role adding flexibility to the grid.

Without TES, no CSP generation was built. This behavior results from the favorable fixed capacity cost of 0.0148 $/kW/h for solar PV in the model, approximately half of the 0.0296 $/kW/h fixed cost for CSP, given that both technologies as implemented share the same capacity factor resource characteristics. This relationship is reversed for the associated storage technologies, with the battery storage fixed capacity cost of 0.00735 $/kWh/h being an order of magnitude higher than 0.000716 $/kWh/h for TES. The cost advantage of TES allowed the combined CSP+TES technology to play a role in the idealized VRE-dominated electricity system. Further investigation of the balance between cheap PV generation and cheap TES storage is provided in Figure A.1, which displays a

system based solely on solar resources. In this system, some CSP+TES was built in addition to PV+batteries. However, the addition of long duration PGP storage sharply increased the share of demand supplied by TES from ~0.22% to ~17%, indicating that the presence of long-duration storage improved the utility of CSP with TES. None of the solar-only systems used CSP for direct generation.

The capacities and system costs for the base case (Figure 4.2 (a-d)), and for the case in which TES was removed, are given in Table 4.3, to show the impact on the full technology mix. Figures throughout this analysis are shown normalized to the mean hourly electrical demand, but the values in Table 4.3 are scaled up to the 2017 hourly average of 453 GW to provide context for comparing the model results to real-world capacities. Removal of TES resulted in no CSP capacity, but caused substantial increases in deployed battery capacity (from 354 GWh in the base case to 523 GWh in the case without TES), along with only marginal changes in PV (424 GW to 428 GW) and wind (1290 GW to 1290 GW) capacity. This behavior again demonstrates the primacy of the role of TES storage for the combined CSP+TES technologies. The system cost remained essentially constant at 10 ¢/kWh for both cases, with a fractional decrease of 0.07 ¢/kWh when CSP+TES was built. This behavior suggests that purely in terms of cost, adding CSP+TES to the grid is a choice rather than a necessity to reach the least-cost system in this idealized electricity system model.

	Base Case	Base Case without TES
System Cost (¢/kWh)	10.1	10.2
Average hourly demand (GW)	453	453
PV capacity (GW)	424	428
Wind capacity (GW)	1,290	1,290
CSP generation capacity (GW)	27.1	0
CSP turbine capacity (GW)	50.6	0
TES capacity (GWh_e)	623	-
Battery capacity (GWh_e)	354	523
Electrolyzer capacity (GW)	50.6	58.2
PGP storage capacity (GWh_e)	89,400	97,400
Fuel cell capacity (GW)	191	221

Table 4.3. Built capacities and system costs for base case and base case without TES for 2017. Capacities for base case system for years 2016-2019 given in Figure A.2. When TES is not included, no CSP is built.

Figure 4.3 shows the temporal variation of the average charging and discharging behavior of each storage technology on a monthly and hourly basis for the base case. TES was utilized at similar levels year-round, with a slight increase during the summer months. Batteries had noticeably higher usage during June-Sep to compensate for a reduction in wind generation during the summer doldrums.[117] Although the least-cost system contained a higher capacity of TES (1.45 kWh/kW of mean demand) than batteries (0.78 kWh/kW of mean demand), batteries showed a higher average usage. This behavior indicates that batteries were used for more routine storage, whereas TES was used when an unusually high level of flexibility was needed. The monthly distributions of TES and batteries show nearly identical charging and discharging, confirming that both storage technologies are mainly used for short-term storage across several days or weeks (Figure 4.3 (a,c)). In contrast, PGP exhibited inverted monthly charging and discharging patterns, discharging the most power during the summer when wind resources were low, with a smaller discharge peak in the winter when the solar resource was low.

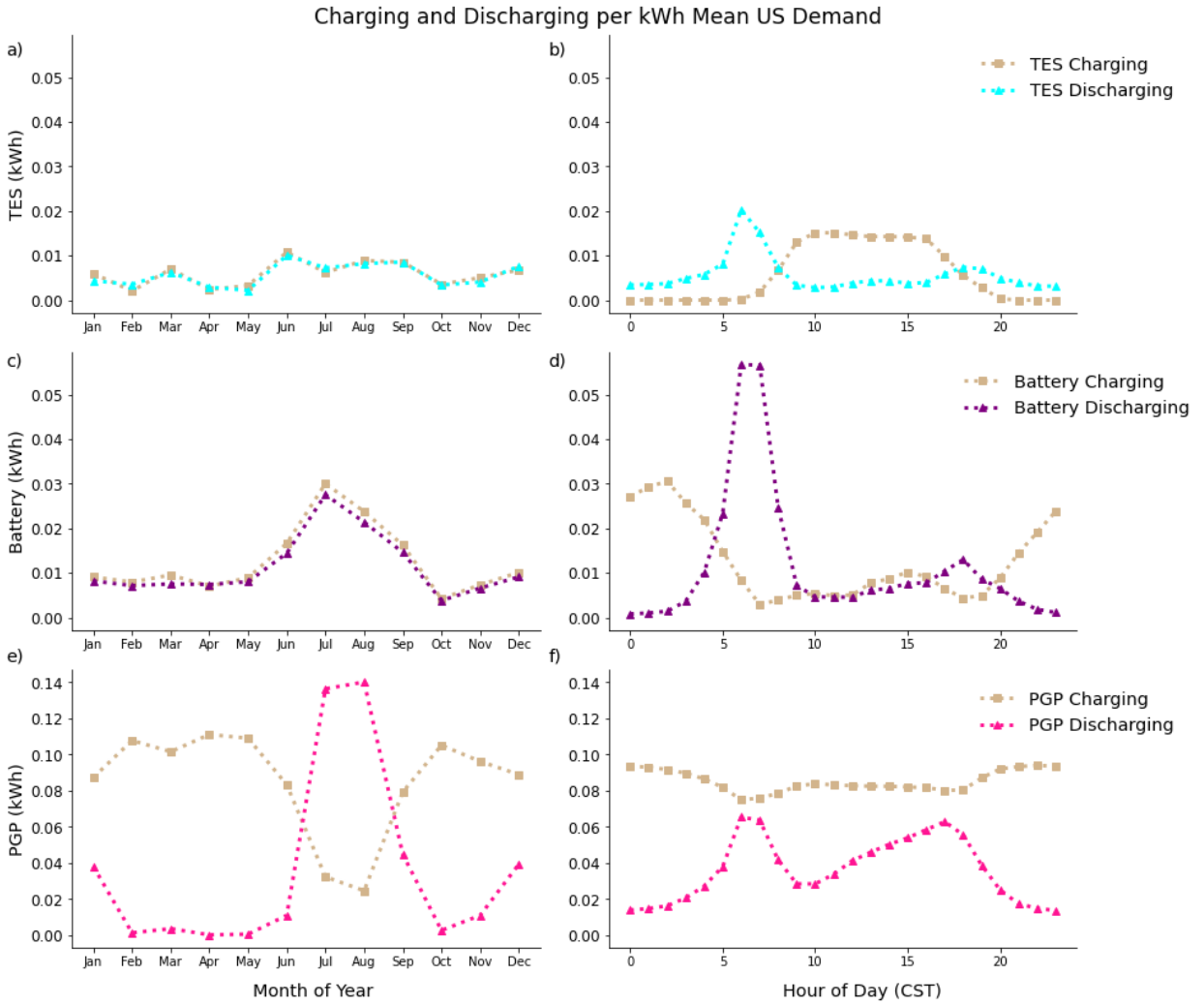

Figure 4.3. Average hourly charging/discharging in each month of the year for TES (a), batteries (c), and PGP (e). Average hourly charging/discharging per hour of day for TES (b), batteries (d), and PGP (f). All plots produced using 2017 base case. Batteries and TES fill a short-duration storage role, with TES charging from solar and batteries charging from wind, whereas PGP fills a seasonal storage role.

The hourly patterns in Figure 4.3 (shown in Central Standard Time (CST)) indicate that TES had a clear cycle of charging determined by the solar resource, with a peak at mid-day. Batteries had the opposite pattern, with peak charging occurring overnight when the wind resource tends to be higher. This pattern for batteries was not substantially different when CSP+TES was removed from the system (Figure A.3). This behavior suggests that given the strong alignment of daytime solar PV

generation with peak daytime demand, PV is preferentially used immediately as opposed to charging battery storage. CSP+TES introduces a cost-effective solar technology that has incentive to store the resource instead of providing direct generation, due to the higher cost of CSP generation compared to TES storage. Batteries and TES both had large discharging peaks in the morning before sunrise and smaller peaks in the evening after sunset, with little use during the day due to the availability of cheap solar PV generation during the daytime demand peak. PGP showed nearly constant charging throughout the day, with similar morning and evening discharge peaks.

The patterns observed for TES and batteries persisted even when long-duration storage was not available, as shown in Figures A.4 and A.5. The absence of PGP led to deployment of excess generation, which decreased the need for frequent use of short-term storage to fill small gaps between resource availability and demand. However, at the times of seasonal lows in generation (summer for wind, winter for solar) a larger capacity of short-term storage was required to meet demand. Removal of PGP from the system consequently resulted in larger capacities of batteries and TES that were used less frequently throughout the year, as shown in Figures A.6-A.10.

4.3.2 Grid Flexibility from other Sources

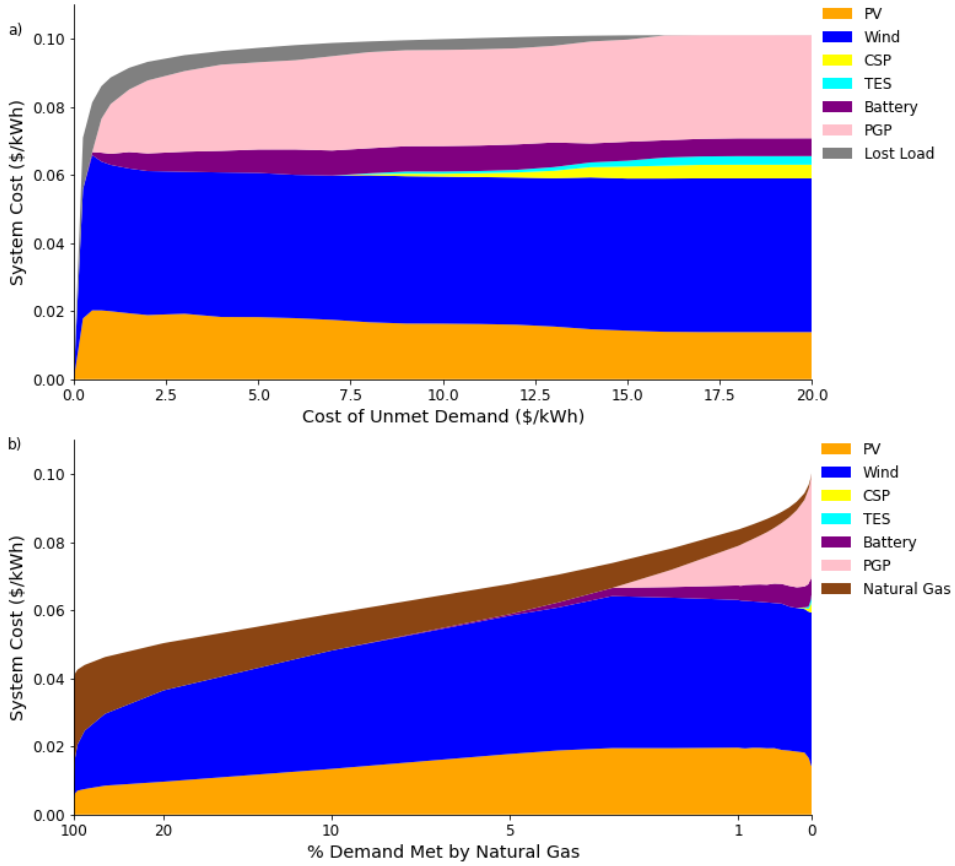

Figure 4.4. System response to the cost placed on unmet demand in (a). System response when the dispatch from natural gas was limited in (b). All systems were modeled using 2017 data for resource availability and demand. These results indicate that CSP with TES, at current ratios of costs, provide valuable grid services when other approaches to grid flexibility are severely limited.

Several approaches can increase the flexibility of an electricity system. In one such approach, the system could occasionally, for a very high cost, supply less than the demand load. The potential effects of a few rare hours in which demand substantially exceeds supply were evaluated by relaxing the strict constraint that demand had to be met for all hours in the period of interest, instead assigning a cost to this "lost load." The cost of lost load was based on the value of economic losses sustained when electrical demand is not met, with units of $/kWh. In the US, estimates place this value between 3–12 $/kWh for the entire economy.[118] The cost of unmet demand was varied between 0 $/kWh and 20 $/kWh to understand how a system built with the base case mix of technologies responded to

looser and tighter constraints on resource adequacy. As shown in Figure 4.4 (a), beginning from the 20 $/kWh unmet demand case supplying 100% of demand, CSP with TES was the first technology to be eliminated from least-cost systems as the cost of unmet demand decreased, and was absent when the cost of unmet demand was ≤$7/kWh. At $7/kWh, only 0.055% of demand, or less than 5 h of mean hourly averaged demand out of the year, went unmet demonstrating that CSP+TES was primarily used to increase flexibility in the grid to meet a small fraction of demand over the course of a year. The overall cost of the system slowly decreased from 10 ¢/kWh in the configuration that met 100% of demand to 9.5 ¢/kWh when the cost of unmet demand was $3/kWh, before dropping precipitously as the cost of lost load decreased to the point where it was cheaper not to build a system at all.

In Figure 4.4 (b), the dispatch from natural gas was constrained to meet no more than a given percentage of demand, thereby requiring VRE generation to meet the remainder of the demand. Natural gas is dispatchable, and thus it acted as a flexibility buffer for the system. Under these constraints and with our specific demand and resource characteristics, at ~90% natural gas, the renewable technology deployed preferentially in least-cost systems was the cheapest generation source, solar PV, followed by wind turbines. Flexibility provided by storage technologies first appeared when batteries entered the system at ~5% natural gas followed by PGP which entered at ~2% natural gas. CSP+TES was not built until natural gas was constrained to meet no more than ~0.1% of demand, making CSP+TES the last technology required to meet the flexibility needs of the idealized VRE-dominated electricity system. However, in the base case system, dispatch from TES actually accounted for ~0.6% of demand with CSP direct generation offering the potential for another ~0.4%. This behavior indicates that once the technology is deployed, it may be used and has value in these idealized least-cost systems beyond the thresholds shown in Figure 4.4 (b). Both the comparison in natural gas in Figure 4.4 (b) and the base case quantities affirm the role of CSP+TES as a “last 1%” technology focused on adding the most difficult and costly final degree of flexibility to the idealized, 100% reliable, 100% variable renewable electricity system. These patterns were also observed when low-carbon, load-following flexibility was added to the grid through natural gas with 90% carbon capture and storage (CCS), as shown in Figure A.11.

4.3.3 Technology Combinations and Interactions

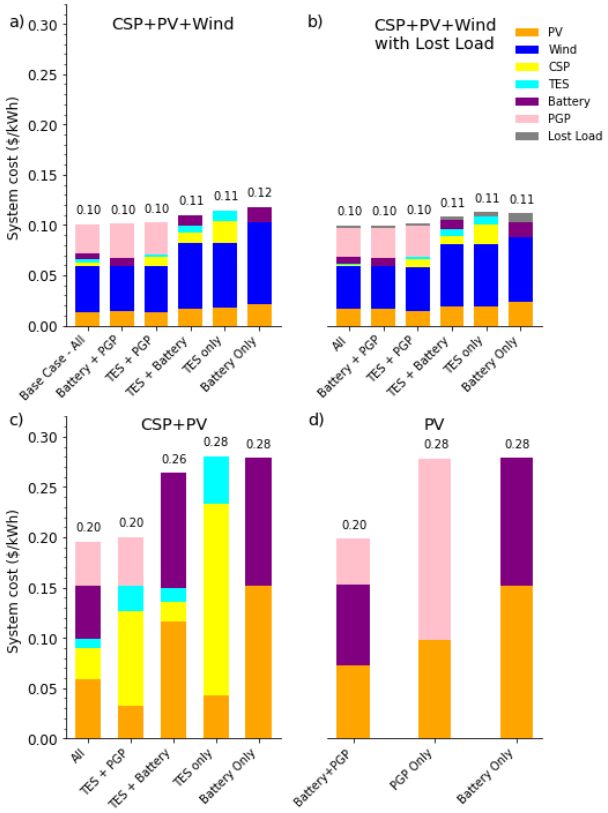

Figure 4.5. Technology combinations for generation and storage, with and without unmet demand. CSP+TES and PV coexist. Wind minimizes need for CSP+TES overnight storage, and unmet demand pushes CSP+TES out of idealized least-cost 100% reliable, 100% VRE-based electricity systems. Additional combinations shown in Figure A.12.

Figure 4.5 shows changes in idealized least-cost electricity systems as different combinations of generation and storage technologies were deployed. When TES was a storage option, CSP with TES was always present in the least-cost systems to add flexibility to the system. Moreover, when both batteries and CSP+TES were included, both technologies were always built simultaneously. More CSP+TES was built in systems without PGP long-duration storage, as seen when comparing the base case to the TES+Battery case in Figure 4.5 (a) and Figure 4.5 (b). Without the PGP buffer, more short-duration storage capacity is needed to meet demand during periods of low solar and wind resources. When PGP was not included in the system and only one short-duration storage technology was used, the TES-only case resulted in a lower system cost than the battery-only case.

In Figure 4.5 (b), a mid-range value of $10/kWh for lost load was used to facilitate comparisons between least-cost systems with (Figure 4.5 (a)) and without (Figure 4.5 (b)) a demand-response mechanism. In general, least-cost systems with lost load included slightly higher installed PV capacity, and lower installed CSP+TES, wind, and PGP capacities compared to cases in which 100% reliability was specified as a strict constraint. Battery capacity increased when lost load was allowed in the base case system, but decreased when lost load was allowed in the Battery+PGP and TES+Battery cases. Capacity values for each case are provided in Table A.4. When lost load is allowed, the substitution of PV for CSP is consistent with the lower asset costs of PV relative to CSP in the base case. Only 0.03% (2.76 hours) of total demand was assigned to lost load when all generation and storage technologies could be deployed. When only one short-duration storage technology could be used, the battery-only system was cheaper than the TES-only system, but experienced twice the lost load (0.09% of demand for battery-only vs 0.04% for TES-only).

Figure 4.5 (c) shows the system assets after removing wind from the generation mix. In the absence of wind power, CSP+TES supplied electricity overnight, resulting in a doubling of system costs due to the higher cost of CSP generation compared to wind. PV remained in the mix to provide generation during the day, with batteries built to support the PV generation. Figure 4.5 (d) then compares this configuration to a system without CSP+TES. The overall system cost for the PV+batteries/PGP storage configuration is essentially the same as the cost for the PV/CSP with TES/batteries/PGP storage configuration, with only a marginal decrease in cost when CSP+TES is added, despite CSP+TES becoming a substantial part of the system. This behavior again suggests that, based on current cost estimates, addition of CSP+TES is a choice rather than a necessity to reach the least-cost system. However, in the absence of PGP, adding CSP+TES to the PV+batteries system decreased system costs by 2 ¢/kWh. Hence, cheap short-duration storage through CSP+TES became more valuable in the absence of seasonal-scale long duration storage.

4.3.4 Cost Drivers for CSP+TES Penetration in the Grid

At current costs, the above analysis shows that CSP+TES fills a short-term storage role that is complementary to and compatible with simultaneous deployment of PV and batteries. Given that costs for many of these technologies are expected to change substantially in the timeframe over

which electricity systems based predominantly on VRE resources are likely to be implemented, a cost sensitivity analysis was performed to analyze the robustness of these results. First, technology costs were varied individually while all other costs were held constant at base case values. Figure 4.6 (a) and (b) provides results when CSP and TES costs respectively are varied, with benchmark costs for Solar Power Tower (SPT) technologies given for each case. CSP cost reductions in (a) primarily resulted in reductions in wind and battery capacity. When CSP reached ~0.6x of the base case cost, batteries were eliminated from the least-cost system. Further cost reductions in CSP reduced the deployment of PGP, with PGP capacity becoming minimal when CSP costs were ≤ 10% of the base case costs. PV was resilient against reductions in CSP cost, remaining in the system even slightly beyond the case in which CSP costs were assumed to reach parity with PV costs. Hence, both solar generation technologies operate within their own niches in providing the ability to meet demand, rather than purely competing with one another based solely on marginal generation capacity cost. Dispatch curves that demonstrated the behavior of least-cost systems as CSP costs decrease are given in Fig A.13.

Reductions in TES costs had a relatively small impact on the overall system cost (Fig 4.6 (b)). As TES costs decreased, the capacities in least-cost systems of batteries and PGP decreased, but neither was fully eliminated from the asset mix until TES costs neared zero. Even in that extreme limit, large capacities of PV and wind generation were deployed in these idealized least-cost electricity systems.

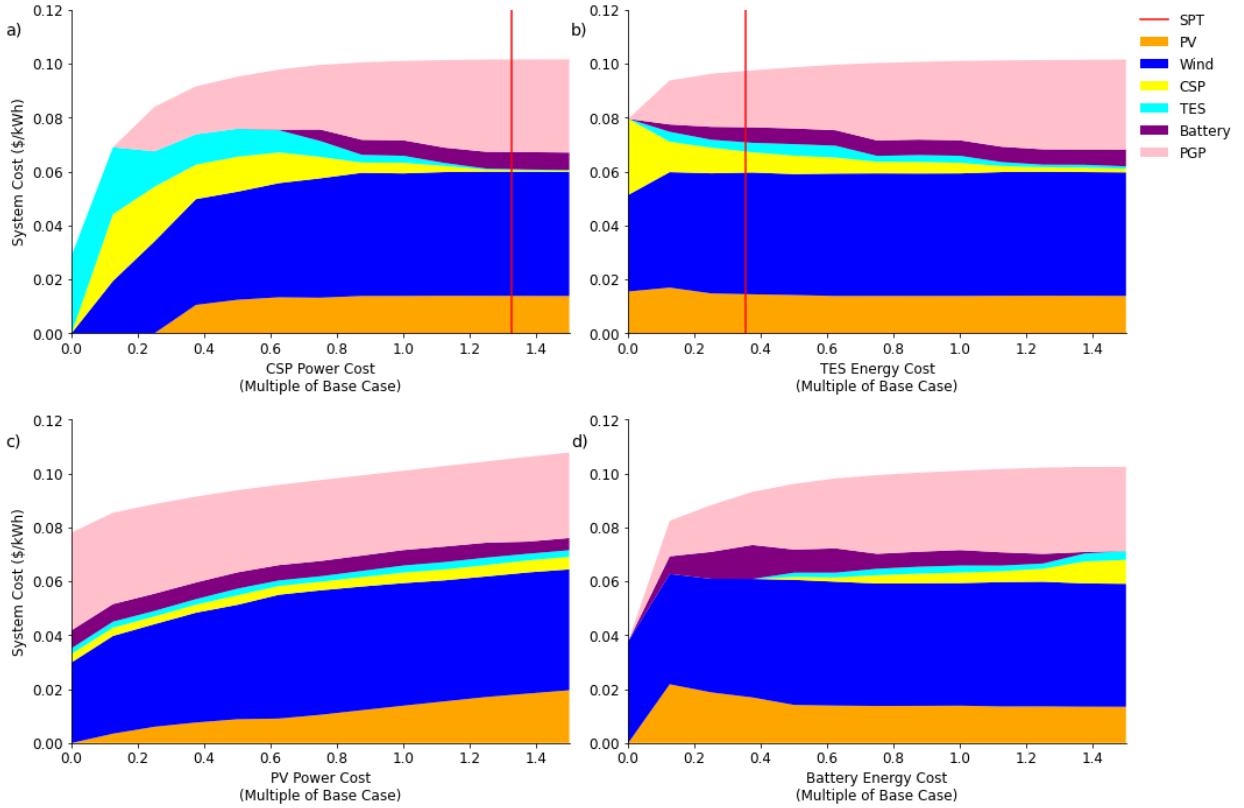

Figure 4.6. System sensitivity to changes in CSP cost (a), TES cost (b), PV cost (c), and battery cost (d) while holding all other costs constant at Parabolic Trough Collector (PTC) base case level. Solar Power Tower (SPT) costs are noted for comparison. The most notable changes in the technology mix were driven by cost changes in batteries and CSP, which could shut each other out of the system by competing to provide flexibility.

Fig 4.6 (c) and (d) show similar cost sensitivity analyses in these idealized least-cost systems as a function of assumed changes in PV costs or battery costs. Decreases in PV costs had a minimal effect on the characteristics of least-cost systems. The wind capacity and overall system cost decreased as PV costs decreased. The absolute cost contributions of PV to the system cost also decreased because the PV costs decreased faster than capacity increased. However, the capacities of other technologies remained nearly constant, with CSP and TES both remaining in least-cost systems even when PV generation was free. This behavior reflects the value of CSP+TES in providing the fundamental need for flexibility inherent in a VRE-based electricity system, even with cheap generation sources. Even

setting PV costs to zero did not eliminate the need for additional flexibility in these idealized least-cost systems beyond that provided by batteries supplied by PV.

When battery costs were varied, CSP and TES were eliminated from least-cost systems when batteries reached 40% of their base case cost, but CSP and TES costs were unchanged (Fig 4.6 (d)). Further decreases in battery cost resulted in a larger deployed capacity of PV in the least-cost systems, whereas the deployed wind capacity decreased slightly. This behavior further confirms that battery costs are the primary driver of combined PV and battery behavior in these idealized least-cost VRE-dominated electricity systems.

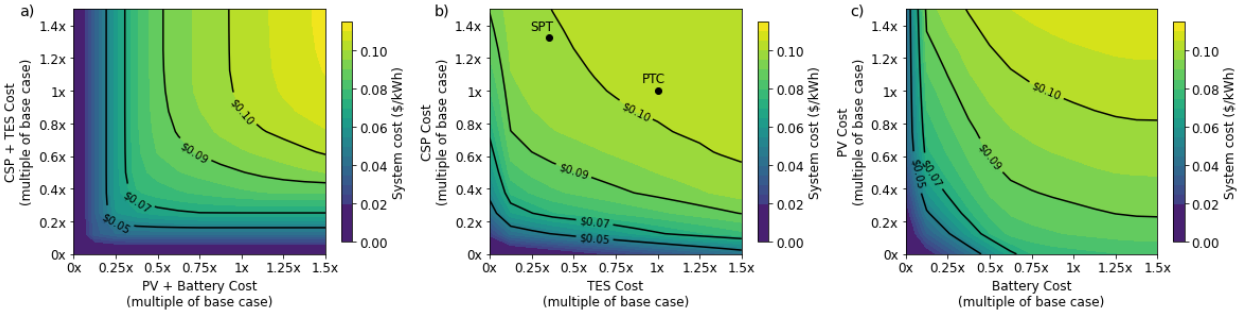

Figure 4.7. Contour plot showing system costs when costs are simultaneously varied for CSP+TES as a pair and PV+batteries as a pair in (a). Contour plot varying cost of CSP generation and TES storage in (b) with current costs of Parabolic Trough Collectors (PTC) and Solar Power Towers (SPT) marked. Contour plot varying cost of PV generation and battery storage in (c). The relatively shallow gradients in panel (b) shows that the results are robust across a range of CSP+TES costs, and the steeper gradient along the vertical direction shows that CSP is the cost-limiting factor for the combined technologies.

Technology costs were also varied in pairs to capture impacts on the overall system costs, as seen in Figure 4.7. In Figure 4.7 (a), the cost of CSP + TES was varied as a single unit by simultaneously applying the same cost multiplier to each technology, and similarly, PV+battery costs were also varied as a unit. The result was nearly symmetrical, with reductions in PV+battery costs exerting a slightly stronger influence on the overall system cost than reductions in CSP+TES costs, as shown by the steeper gradient. Hence these idealized least-cost systems experienced a trade-off between the

two technology pairs, in accord with other results (Figures 4.5 and 4.6). Although the technological mix in the least-cost system might change substantially depending on a choice to deploy CSP+TES instead of PV+batteries, both technology paths were capable of meeting demand at roughly the same overall system cost.

In Figure 4.7 (b), PV and battery costs were kept constant, and CSP and TES costs were varied separately. Although the overall diagonal shape of the contour plot suggests that improvements in both technologies were effective in decreasing system costs, the steeper vertical gradient shows that CSP is clearly the more important cost driver for total asset costs of these idealized least-cost electricity systems. Decreases in TES costs led to greater reductions in electricity costs when CSP costs were high, as demonstrated by the comparison between Parabolic Trough Collector (PTC) and Solar Power Tower (SPT) technologies. Generation costs for SPT were higher than PTC costs, but SPT has lower storage costs than PTC, resulting in an overall lower system cost when SPT was deployed in these idealized electricity systems relative to PTC.

Figure 4.7 (c) shows the opposite pattern for PV and batteries. Although the diagonal contour lines also show that improvements in both technologies decreased system costs, the steeper gradient in the horizontal direction indicates that battery storage was the primary cost driver, rather than generation from PV. This behavior can be understood intuitively from the higher cost of battery storage compared to the cost of PV generation. The costs of the two storage technologies were also varied, and system costs were more sensitive to reductions in battery costs than to reductions in TES costs (Figure A.14).

4.4. Discussion

4.4.1 CSP with TES as a Storage Technology

Dispatch behavior and cost sensitivity analysis both suggest that the primary grid service value of CSP arises from coupling with cheap TES, rather than as a direct generation technology. CSP+TES provides valuable grid services mostly relative to batteries rather than relative to PV generation, with cost benchmarks tied to battery costs for when CSP+TES is a contributor to least-cost systems that meet 100% of demand. At current costs represented by the base case in these 100% reliable idealized

least-cost electricity systems, the CSP + TES grid services niche would be eliminated if battery costs decreased to 40% of their current costs. NREL projects that battery costs will reach 40% of current levels by 2050, or even as soon as 2030 in their most aggressive projection.[24]

Aggressive cost reductions would be required to allow parabolic trough CSP to be deployed in the modeled least-cost systems at those battery costs, but given the relative maturity of CSP technology, these reductions are considered unlikely.[27,119,120] The less mature Solar Power Tower technology could potentially achieve more substantial cost reductions, with DOE SunShot goals calling for a 50% reduction of 2010 costs by 2030.[121] Although CSP generation costs include both the solar field and the steam turbine, the maturity of the steam turbine technology due to extensive usage in other contexts makes the solar field the most likely target for innovation.[122] Turbine efficiency could be improved if higher temperatures could be obtained from the solar field, which would then lower the overall cost of CSP energy generation.[123]

Even substantial cost reductions for solar power towers would only maintain CSP+TES's role as a short-duration storage technology in these idealized least-cost VRE-dominated 100% reliable electricity systems. In our modeled systems, the 50% cost reduction called for in the SunShot goals was not sufficient to convert CSP into a bulk power provider. For example, Fig A.8 shows that CSP generation became a substantial contribution to the asset mix at 25% of base case costs. Reductions in the cost of CSP and TES also would not eliminate the need for long-duration storage such as PGP. The need for seasonal storage decreased in idealized least-cost reliable systems when CSP generation costs were very cheap, but PGP was not eliminated from the asset mix until either CSP or TES were nearly free.

4.4.1.2 CSP with TES in a System without Long-Duration Storage

Without PGP, the analysis shows that batteries and TES were used relatively infrequently, only using the full built capacity during the periods of seasonal resource lows (Figures A.4–A.10). In this regime, the addition of CSP+TES to a battery-only idealized 100% VRE/storage system decreased system costs by ~7% (Figure 4.5). Notably, TES is the preferred technology in this analysis to add the final measure of flexibility needed to reach a reliable 100% VRE-based system. This behavior

was seen both when gradually eliminating natural gas from the system (Figures 4.4(b) and A.11), and when allowing the system to include unmet demand (Figures 4.4 and 4.5). When CSP+TES was removed to leave a battery-only VRE/storage system (Figure 4.5), least-cost systems resulted in additional lost load as opposed to meeting the extra demand with batteries. The cheaper storage from TES made TES a more valuable technology for the highly infrequent use needed in idealized VRE-dominated least-cost systems that did not contain long-duration storage. The modeling indicates that the strongest incentives to build CSP+TES occur in systems without firm generators, long-duration storage, or other mechanisms to obtain grid flexibility.

4.4.2 Considerations for CSP and TES Integration into Renewable Systems

Across a range of scenarios and costs, CSP with TES maintained a small role in idealized least-cost systems that met 100% of demand. This finding was also verified across multiple years of input data between 2016–2019 to ensure that the 2017 base case year was not an outlier (Figure A.2). Unless CSP costs were assumed to reach less than 50% of current levels, CSP+TES primarily acted as a "last 1%" peaker technology. This behavior suggests that efforts to increase demand-side flexibility could minimize the value of CSP to satisfying resource adequacy planning constraints in such electricity systems. NREL's Electrification Futures Study suggests the potential for large shifts in peak demand behavior, particularly in the case of widespread usage of electric vehicles.[18]

4.4.2.1 Impact of Firm Generators

Firm generators with low- or zero-carbon emissions could also minimize the need for storage technologies, reducing the need for CSP+TES to contribute to grid flexibility. The impact of adding such firm generators was evaluated by allowing for either natural gas with CCS (Figure A.11) or nuclear (Figure A.15) to be included in the modeled least-cost electricity systems. For systems with natural gas with CCS, CSP+TES was present in the idealized least-cost system only if natural gas with CCS was limited to ≤3% of total dispatch. The inclusion of nuclear power minimized the role of CSP+TES, but CSP+TES was nevertheless used in combination with batteries to smooth out sharp demand peaks, supplying ~0.1% of demand. Clearly, these firm generator technologies could play a role in meeting demand for electricity systems with large amount of generation from variable renewable resources, but such technologies are often limited from future electricity systems by

regulation or mandate.[72] Dispatchable hydropower was not considered here, but would be expected to have a similar impact in our idealized least-cost system to the other dispatchable technologies that were modeled, such as natural gas. The geographical limitations on hydropower generation also prevent it from fully eliminating the need for variable renewables, with limited hydropower growth expected in the US through 2050.[124] Regardless of firm generators, some amount of variable renewables are expected in future electricity systems, which will consequently require either curtailment or storage of those variable resources. Our analysis indicates that under certain albeit limited conditions, CSP+TES is a viable option to provide such storage, and remains so even at relatively low penetration of variable renewables, as seen in Figures 4.4 (b), A.11, and A.15.

4.4.3 Limitations

This analysis does not consider the use of CSP for non-electrical cogeneration products such as heat, desalinated water, or hydrogen.[120,125] These uses might improve the economics of CSP implementation beyond what is evaluated here.[126] Hybridization of CSP with biofuels, geothermal, or fossil fuels could provide benefits such as increased capacity factor, increased efficiency, and cost-reductions from sharing equipment between technologies.[85,126] These potential benefits are also outside the scope of this analysis. Thus, the results presented here represent a conservative estimate of the utility of CSP.

This model assumes free, lossless transmission across the contiguous US, without separation into more geographically constrained load-balancing regions. The hourly time resolution in the model assumes that load balancing and grid stabilization on shorter time scales will be provided by other currently available technologies. Each model run generates a single end state, so no learning rates were used in cost calculations. The modeled system was assumed to be built instantaneously using "overnight" costs, and the configurations of the modeled least-cost systems were determined using perfect foresight of future resource availability and demand. Consequently, the results herein represent a lower bound for the generation and storage capacity needed to meet electricity demand. The exclusion of offshore wind power from the model is an exception to this lower bound, as wind off the East coast of the US generally has higher capacity factors and less variability.[127] However,

offshore generation profiles still exhibit considerable variability,[127,128] and the conclusions of this analysis should not be substantially impacted by this exclusion.

4.5. Conclusions

CSP with TES occupies a small but persistent niche in an idealized highly reliable least-cost electricity system with 100% of generation from variable renewable resources. The utility of combined CSP and TES technologies arises primarily the addition of cheap energy storage that provides valuable flexibility to the grid by allowing demand to be met a few hours throughout the year at reduced cost compared to batteries. This behavior results in greater competition of CSP+TES with battery usage rather than with PV deployment. Each storage technology provided a distinctive grid service in these least-cost idealized electricity systems. For CSP with TES, the low cost of TES allowed for a large capacity to be built, with TES used to meet the most difficult hours of demand throughout the year. Batteries charged primarily from wind and provided steady short-duration storage that cycled a lower capacity at a higher frequency than TES. PGP provided seasonal-scale storage that reduced the need for overbuild of generation and short-duration storage to meet demand during periods of low solar and wind resources. A cost sensitivity analysis showed that deployment of CSP+TES in idealized least-cost electricity systems would increase more in response to reductions in the cost of solar generation than due to equivalent fractional reductions in the cost of TES technology. These cost improvements should be benchmarked against utility-scale battery storage costs, however, which are declining more rapidly than CSP+TES costs have historically decreased. Thus, although CSP with TES offers a cost-effective approach to provide for the “last 1%” of demand in reliable deeply decarbonized electricity systems, future technology costs may reduce its benefit to the overall system cost.

Chapter 5

SUMMARY AND FUTURE OUTLOOK

In this thesis we have analyzed technologies and modeling techniques with the potential to support a transition to global net-zero emissions. This last chapter will summarize these results briefly, and then discuss some unanswered questions and potential research directions that may be of interest for future research.

5.1 Summary

Chapter 2 examined the failure modes of substrate-supported and free-standing membrane-embedded microwire devices for solar fuels generation. The primary corrosion pathways for each architecture were identified and characterized. Substrate-supported microwires experienced top-down corrosion through defects in the TiO_2 protection layer, with propagation through the substrate that resulted in secondary bottom-up corrosion processes. This resulted in arrays of corroded wires that expanded over time. Free-standing microwires in membranes exhibited uniform bottom-up corrosion through the membrane, which consumed the entire sample within the 10-day period studied. They also experienced top-down corrosion both through TiO_2 defects and through membrane channels.

Chapter 3 presented fabrication methods for GaAs and InP nanowire architectures. Control over the wire diameter, sidewall tapering, and wire height was achieved through e-beam lithography and ICP-RIE plasma etching. These nanostructures offer opportunities for development of future high-efficiency solar devices through improved light absorption.

Chapter 4 analyzed the role of concentrated solar power (CSP) with thermal energy storage (TES) compared to solar photovoltaics (PV) and battery storage in a macro-energy model across the continental US. The addition of CSP with TES was only found to lower costs substantially when long-duration storage was not included in the system. However, the cheap storage from TES was found to improve grid flexibility and reduce the amount of unmet demand in the system. Cost

sensitivity analysis found that the penetration of CSP with TES was primarily limited by the high cost of CSP generation, and they competed principally with batteries rather than with direct electricity generation from solar PV.

5.2 Micro- and Nano-wire Solar Fuels Devices

Current solar fuels devices suffer from short lifetimes that render them impractical for commercial use. Progress has been made in developing protection layers and device architectures that limit degradation, but more work is still needed. One path to a more stable device is through defect isolation, when flaws in the protection layer only lead to corrosion of a piece of the device rather than catastrophic failure of the whole. Microwire arrays offer such isolation if they can be successfully removed from substrate without introducing further defects in their protection layer. Based on the analysis of microwire arrays given here in Chapter 2, future research could pursue this goal through development of membranes that are stable in highly acidic or alkaline conditions, provide good mechanical stability for the microwire arrays with minimal swelling, and can be adhered to other surfaces that provide a back contact for the wires without allowing penetration of a corrosive electrolyte. This would mitigate the bottom-up corrosion pathways analyzed in Chapter 2, while allowing for defect isolation that would minimize the effect of top-down corrosion through the protection layer. Thus, such membranes could facilitate the development of flexible solar fuels devices that are resilient to both chemical and mechanical stresses.

5.3 Systems Modeling for Multi-Benefit Technologies

Reaching a net-zero economy necessarily involves changes across many different systems that have traditionally been treated separately. While there are growing efforts to consider how technologies act at the nexus of such systems, the scale and complexity of the calculations involved make this a difficult task. The simplified style of modeling used in Chapter 4 of this thesis might offer a route to better understand the fundamental tradeoffs involved in these complex intersecting systems. For instance, the inclusion of heating demand in future models of concentrated solar power (CSP) would better capture the overall potential of CSP to provide benefits to the heat-energy nexus compared to the purely electricity-based analysis provided here. Similarly, including transportation powered by

electricity and hydrogen fuel could provide valuable insights on how power-to-gas-to-power (PGP) technologies might act at the electrical-transportation nexus.

It is also important to consider factors beyond purely technoeconomic concerns that will impact decision-making in the net-zero transition. The economy-wide changes needed for this transition will necessarily have effects on jobs, human health, and other non-technical areas. In order to better inform policy-makers trying to balance all of these considerations, scientists could seek out collaborations with experts in these areas, and when suitable, begin integrating these impacts into technical models. Some examples of this kind of integration already exist,[129] and it is my hope that they will become more common as the field develops.

5.4 Future Outlook

The work of transitioning to a sustainable, net-zero society is incredibly challenging. It will require finding the economic and political will to change almost every aspect of how we live, in addition to achieving rapid technological advancement to support those changes. At the time of this writing, there is growing momentum around the world to take action on the scale necessary to start such a revolutionary shift. It is our hope that the work reported in this thesis will contribute to these efforts in some small measure.

Appendix A

SUPPLEMENTARY MODELING INFORMATION

A.1. Model Formulation

A.1.1 Nomenclature

Symbol	Unit	Description
g (superscript)	-	Generation technology (wind, solar, CSP, natural gas, natural gas with CCS)
v (superscript)	-	Energy conversion (electrolyzer, fuel cell, CSP turbine)
s (superscript)	-	Energy storage (PGP storage, battery, TES)
from s (superscript)	-	Discharge from energy storage
to s (superscript)	-	Charge to energy storage
t (subscript)	H	Time step, starting from 1 and ending at T
c_{capital}	\$/kW for generation or conversion \$/kWh for storage	Overnight capital cost
c_{fixed}	\$/kW/h for generation or conversion \$/kWh/h for storage	Fixed cost
$c_{\text{fixed O\&M}}$	\$/kW/yr	Fixed operating and maintenance (O&M) cost
c_{var}	\$/kWh	Variable cost
f	-	Capacity factor (generation technology)
h	h/year	Average number of hours per year
i	-	Discount rate
n	Yrs	Project life
Δt	H	Time step size, i.e., 1 hour in the model
C	kW for generation or conversion kWh_e for storage kWht for heat storage	Capacity
D_t	kW	Dispatch at time step t
M_t	kWh	Demand at time step t
S_t	kWh_e for storage kWht for heat storage	Energy remaining in storage at time step t
γ	1/yr	Capital recovery factor
δ	1/h	Storage decay rate, or energy loss per hour expressed as fraction of energy in storage
η	-	Round-trip efficiency
τ	h	Storage charging duration

Table A.1. Model Nomenclature

A.1.2 Cost Calculations

Fixed cost of generation, conversion, and storage technologies (wind, photovoltaics, CSP, natural gas with CCS, batteries, TES, electrolysis plant, fuel cell, hydrogen storage):

$$c_{\text{fixed}}^{g,v,s} = \frac{\gamma c_{\text{capital}}^{g,v,s} + c_{\text{fixed O\&M}}^{g,v,s}}{h} \qquad (S.1)$$

Capital recovery factor:

$$\gamma = \frac{i(1+i)^n}{(1+i)^n - 1} \qquad (S.2)$$

A.1.3 Constraints

Capacity:

$$C^{g,v,s} \geq 0 \qquad \forall g, v, s \qquad (S.3)$$

Dispatch:

$$0 \leq D_t^g \leq C^g f_t^g \qquad \forall g, t \qquad (S.4)$$

$$0 \leq D_t^v \leq C^v \qquad \forall v, t \qquad (S.5)$$

$$0 \leq D_t^{\text{to } s} \leq \frac{C^s}{\tau^s} \qquad \forall s, t \qquad (S.6)$$

$$0 \leq D_t^{\text{from } s} \leq \frac{C^s}{\tau^s} \qquad \forall s, t \qquad (S.7)$$

$$0 \leq S_t^s \leq C^s \qquad \forall s, t \qquad (S.8)$$

$$0 \leq D_t^{\text{from } s} \leq S_t^s (1 - \delta^s) \qquad \forall s, t \qquad (S.9)$$

Storage energy balance:

$$S_1^s = (1 - \delta^s) S_T \Delta t + \eta^s D_T^{\text{to } s} \Delta t - D_T^{\text{from } s} \Delta t \qquad \forall s \qquad (S.10)$$

$$S_{t+1} = (1 - \delta^s) S_t \Delta t + \eta^s D_t^{\text{to } s} \Delta t - D_t^{\text{from } s} \Delta t \qquad \forall s, t \in 1, \ldots, (T-1) \qquad (S.11)$$

System energy balance:

$$\sum_g D_t^g \Delta t + D_t^{\text{from } s} \Delta t = M_t + D_t^{\text{to } s} \Delta t \qquad \forall g, t \qquad (S.12)$$

A.1.4 Power-to-gas-to-power implementation

Hydrogen is stored with a storage energy balance identical to equations S.10 and S.11. The rate of charging and discharging for the hydrogen storage is limited by the electrolyzer and fuel cell

capacities, as shown below where s' denotes hydrogen storage, v denotes the electrolysis facility, and v' denotes the fuel cell.

$$0 \leq D_t^{to\,s'} \leq C^{v} \quad \forall t \quad (S.13)$$

$$0 \leq D_t^{from\,s'} \leq C^{v'} \quad \forall t \quad (S.14)$$

$$0 \leq S_t' \leq C^{s'} \quad \forall t \quad (S.15)$$

$$0 \leq D_t^{from\,s'} \leq S'(1-\delta^{s'}) \quad \forall t \quad (S.16)$$

A.1.5 Thermal energy storage implementation

Thermal energy is stored with a storage energy balance identical to equations S.10 and S.11. The rate of charging and discharging for TES is limited by the CSP solar field and turbine capacities, as shown below, where s'' denotes thermal energy storage, g' denotes solar field capacity, and v'' denotes turbine capacity.

$$0 \leq D_t^{to\,s''} \leq C^{g'} \quad \forall t \quad (S.17)$$

$$0 \leq D_t^{from\,s''} \leq C^{v''} \quad \forall t \quad (S.18)$$

$$0 \leq S_t'' \leq C^{s''} \quad \forall t \quad (S.19)$$

$$0 \leq D_t^{from\,s''} \leq S''(1-\delta^{s''}) \quad \forall t \quad (S.20)$$

A.1.6 Objective function

$$minimize(system\ cost) \quad (S.21)$$

$$system\ cost = \sum_g c_{fixed}^{g} C^{g} + \sum_g \left(\frac{\sum_t c_{var}^{g} D_t^{g}}{T}\right) + \sum_v c_{fixed}^{v} C^{v}$$
$$+ \sum_s c_{fixed}^{s} C^{s} + \frac{\sum_t c_{var}^{to\,s} D_t^{s}}{T} + \frac{\sum_t c_{var}^{from\,s} D_t^{s}}{T} \quad (S.22)$$

A.1.7 Data and Code Availability

The Macro-Energy Model (MEM) uses historical weather data with hourly time resolution over the contiguous U.S. for years 1980–2020 for wind and solar input data. The model incorporates demand data with hourly time resolution for 2015-2019 from the U.S. Energy Information

Administration (EIA). The model code, hourly input data, and data visualization code are available on GitHub at https://github.com/carnegie/MEM_public.

A.2. Technology Cost Calculations

A.2.1 Generation Technologies

CSP and TES costs from NREL's System Advisory Model 2020.2.29 were multiplied by 1.02 to account for inflation from their 2018 costs to 2019 dollars based on U.S. Department of Labor Bureau of Labor Statistic consumer price index data.

Generation Technologies	**Nuclear**	**Natural Gas with CCS**
Technology Description	Advanced Nuclear	Combined cycle with 90% carbon capture
Total Overnight Cost ($/kW)	6317[99]	2569[99]
Lifetime (years)	40[99]	30[99]
Discount Rate	0.07	0.07
Capital Recovery Factor (%/year)	7.50%	8.06%
Fixed O&M Costs ($/kW-yr)	121.13[99]	27.48[99]
Variable O&M Costs ($/kWh)	2.36[99]	0.00582[99]
Fuel Cost ($/kWh)	0.00715[99]	0.0214[99,103]
Heat Rate (Btu/kWh)	10461[99]	7124[99]
Annualized Hourly costs		
Fixed Cost	0.0679	0.0268
Variable Cost	0.0095	0.0272

Table A.2. Additional costs for generation technologies. Costs taken from the EIA's 2020 Annual Energy Outlook.[99] All values in 2019 US dollars.

Fuel costs for natural gas and natural gas with carbon capture and storage (CCS) were calculated using the formulas:

$$Efficiency = \frac{Heat\ Content\ of\ Electricity\ (\frac{Btu}{kWh})}{Heat\ Rate\ (\frac{Btu}{kWh})} \qquad (S23)$$

$$Fuel\ cost\ (\frac{\$}{kWh}) = \frac{Fuel\ Cost\ (\frac{\$}{MMBtu})}{\frac{Heat\ Rate\ (\frac{Btu}{kWh})}{1000}} \cdot efficiency \qquad (S24)$$

where the heat content of electricity is 3412.14 Btu/kWh.

A.2.2 Power-to-gas-to-power

The power-to-gas-to-power system modeled here was based on NREL's H2A model. This consisted of an electrolysis facility using polymer electrolyte membrane (PEM) electrolyzers with a compressor to produce hydrogen, and underground storage. The power used to compress the hydrogen gas was included in the net electrolysis efficiency, and no ramp rate constraint was used.

Electrolysis Facility	**Electrolyzer**	**Compressor**
Technology Description	Polymer electrolyte membrane (PEM)	Isentropic
Fixed Capital Investment ($/kg$_{H2}$/h)	63000	917
Fixed Annual O&M ($/kg$_{H2}$/h)	1820	182
Lifetime (years)	7 stack, 40 BoP	15
Conversion Efficiency	61.4% (LHV)	-
Annualized Capital Cost ($/yr*kg$_{H2}$/h)	9820	283
Annualized Hourly costs		
Fixed Cost	1.12	0.0323
Variable Cost	0	0

Table A.3. Electrolysis facility costs. All values taken directly or derived from ref.[105] All values in 2019 US dollars.

The electrolysis plant costs are based on a design capacity of 50,000 kg$_{H2}$/day. The final electrolyzer plant cost is 66,400 ($/h)/kg$_{H2}$ produced. The electrolyzer stack accounts for 47% of total costs, and balance of plant (BoP) accounts for 53%. This separation is important because the stack has an estimated lifetime of 7 years compared to 40 years for the BoP components. The fixed annual O&M costs are estimated at 3.80 million dollars for the entire plant. The default NREL H2A PEM

electrolyzer stack uses 49.23 kWh_e/kg_{H2} and is 67.7% efficient based on the lower heating value (LHV) of hydrogen. Additional ancillary power usage in the electrolyzer plant totals 5.04 kWh_e/kg_{H2}.

The H2A default compressor has a design flow rate of 58,000 kg_{H2}/day. The installed cost is 2.22 million dollars, or 917 ($/h)/$kg_{H2}$. The fixed annual O&M costs for the compressor are 441,000 ($/h)/$kg_{H2}$. The default compressor power requirement for the design flow rate is 1,500 kW_e. This equates to an energy requirement of 0.621 kWh_e/kg_{H2} to compress 1 kg_{H2}. The electrolysis facility used in the model consists of this combined electrolyzer, BoP, and compressor. The value $\eta_{electro}$ is the efficiency to create and compress hydrogen for these three components,

$$\eta_{electro} = \left(\frac{49.2\ kWh_e}{kg_{H_2}} + \frac{5.1 kWh_e}{kg_{H_2}} + \frac{0.6\ kWh_e}{kg_{H_2}}\right)^{-1} * \frac{kWh_{H_2}}{kg_{H_2}} \qquad (S25)$$

where $\eta_{electro}$ = 60.7% based on the LHV of hydrogen.

A.3. Supplementary Figures and Tables

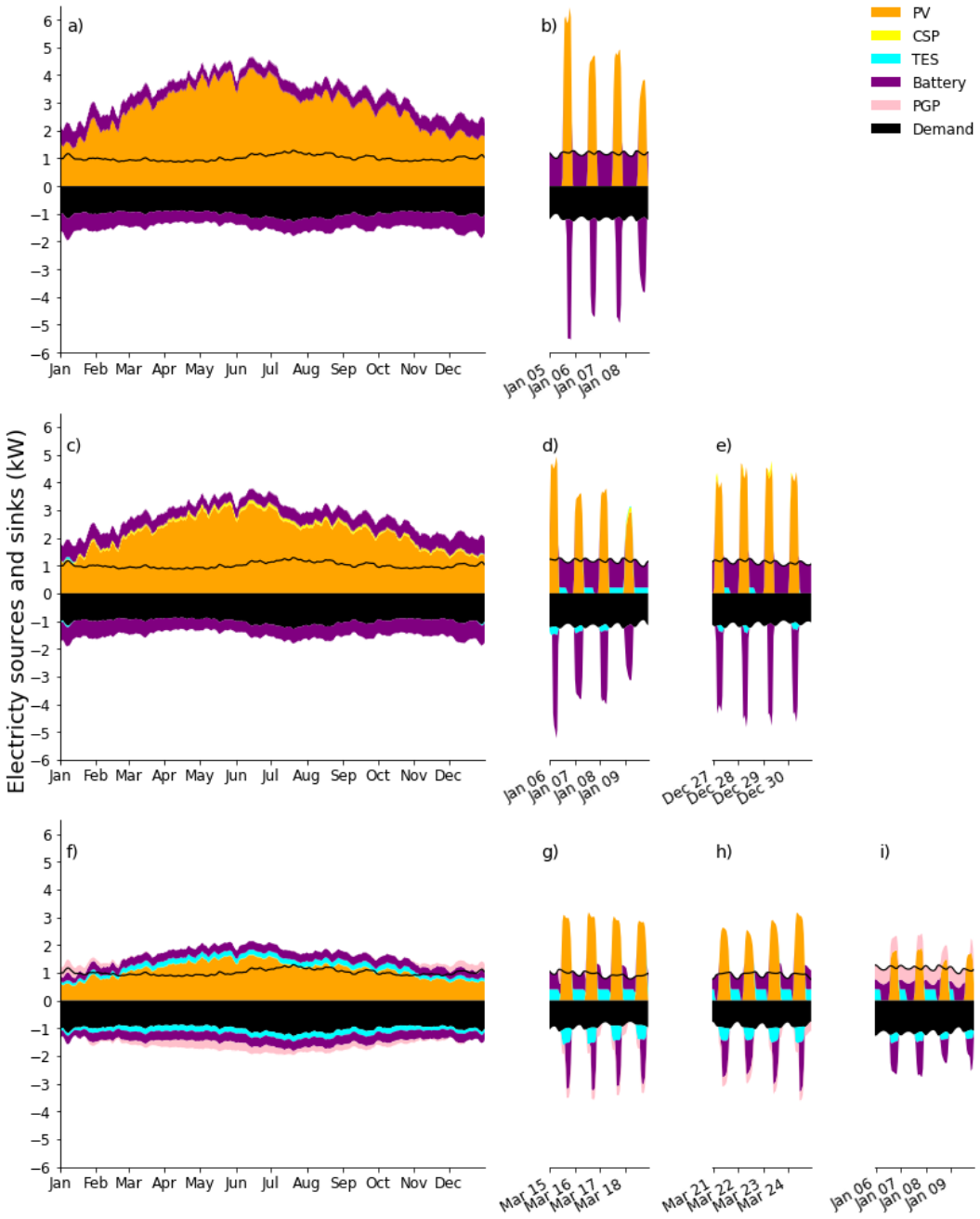

Figure A.1. Dispatch curve for PV + battery system for a year in (a), with the 5 days of maximum hourly battery dispatch shown in (b). Dispatch curve for PV + CSP + TES + battery system over a year in (c), with 5 days of maximum hourly dispatch from TES and batteries in (d) and (e), respectively. Dispatch curve for PV + CSP + TES + Battery + PGP system over a year in (f), with the 5 day period of maximum hourly dispatch for TES, battery, and PGP in (g), (h), and (i),

respectively. All dispatch curves use 2017 data, with 5-day averaging for the annual curves (a), (c), and (f).

The system in Fig. S1 (a-b) with only PV and batteries had a large overbuild of generation, resulting in 15,777 kW of curtailed generation over the course of the year, for an average of 1.80 kW/h. The addition of CSP and TES in Fig. S1 (c-e) reduced the overbuild to a curtailment of 10,651 kW from the grid, and 409 kW at the heat node used to represent CSP in the model. The total was 11,060 kW curtailed, or an average of 1.26 kW/h. The average demand was normalized to 1 kW/h, so both situations represent more electricity being curtailed than utilized.

Batteries were used regularly in Fig. S1 (c) because batteries were paired with low-cost generation from PV. TES was mainly used in the winter when the solar resource was smallest. When long duration PGP storage was included in Fig. S1 (f-h), TES was used year-round. The share of TES used increased sharply when PGP was added, with TES providing ~0.22% of demand in Fig S1 (c) without PGP, and ~17% of demand when PGP was included in Fig S1 (f). Both TES and batteries cycled daily for overnight use, while PGP was used in a seasonal storage role, as expected.[20]

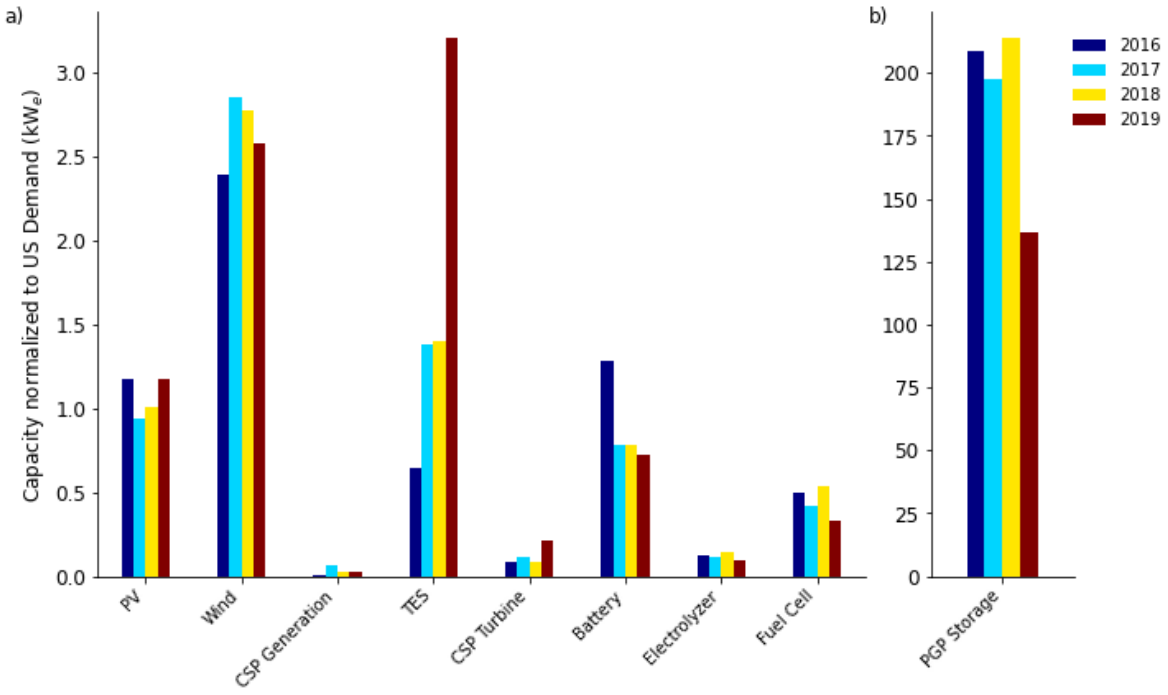

Figure A.2. Capacities of technologies for years 2016-2019 normalized to US demand, with each year modeled separately. The base case year for analysis was 2017.

Modeling of additional years of weather and demand data in Figure S2 showed that the base case year (2017) had mid-range capacity values for CSP+TES. Although the capacity values did fluctuate in different years, all include CSP+TES in the optimal system, indicating that the role of CSP+TES exists across multi-year timeframes.

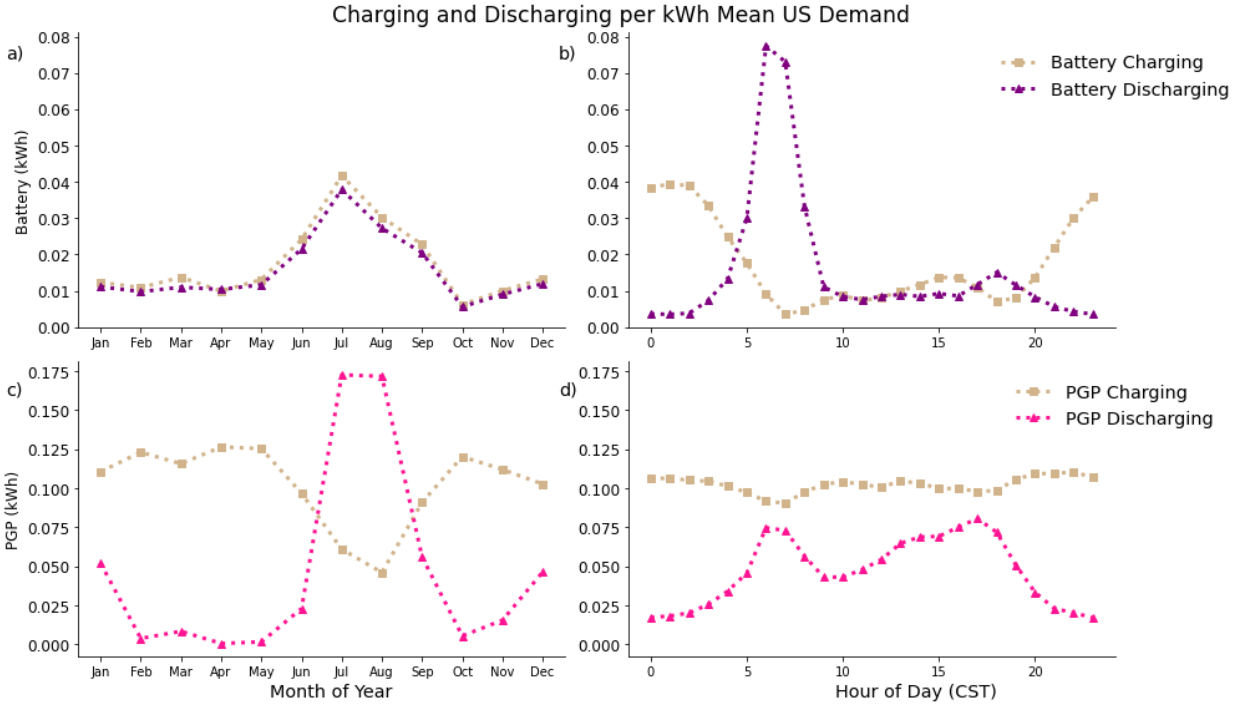

Figure A.3. Average hourly charging/discharging in each month of the year for batteries (a) and PGP (c). Average hourly charging/discharging per hour of day for batteries (b) and PGP (d). All plots produced using 2017 base case. Batteries primarily charge from wind at night, while PGP fills a seasonal storage role.

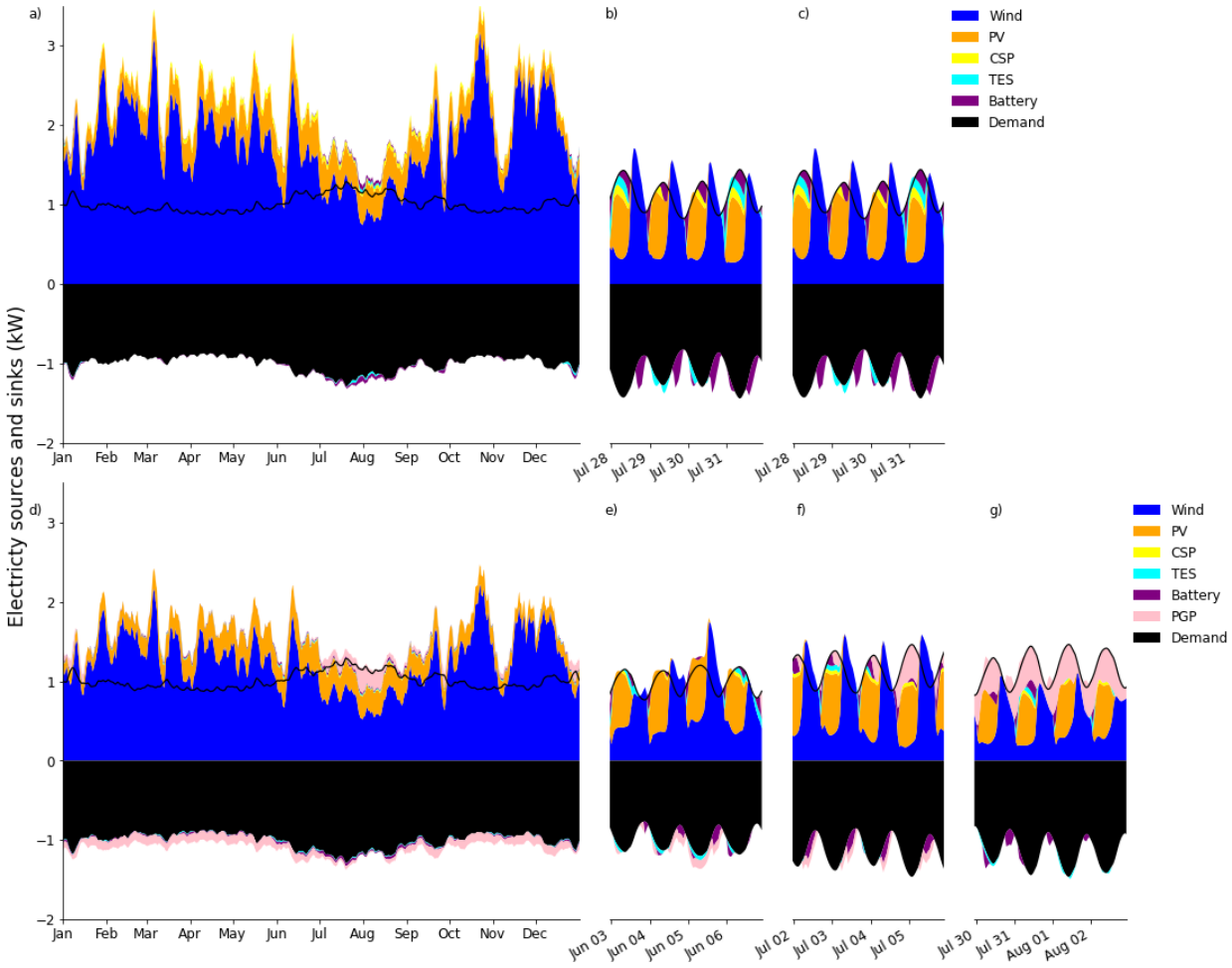

Figure A.4. Dispatch curve for 2017 data with 5-day averaging in (a). The panels in (b) and (c) show hourly dispatch for the 4-day periods of maximum dispatch from TES and batteries, respectively. Dispatch curve for 2017 data with 5-day averaging including long-duration PGP storage in (d). The panels in (e), (f), and (g) show hourly dispatch for the 4-day periods of maximum dispatch from TES, batteries, and PGP, respectively.

The annual dispatch curves with 5-day averaging shown in Figure S4 (a) and (e) demonstrate that batteries and TES both filled a short-term storage role, with neither providing seasonal storage in either scenario. In the absence of PGP, overbuilding generation, particularly wind generation, is cheaper than storing energy seasonally. This finding is in accord with prior analyses of the role of long-duration storage.[20]

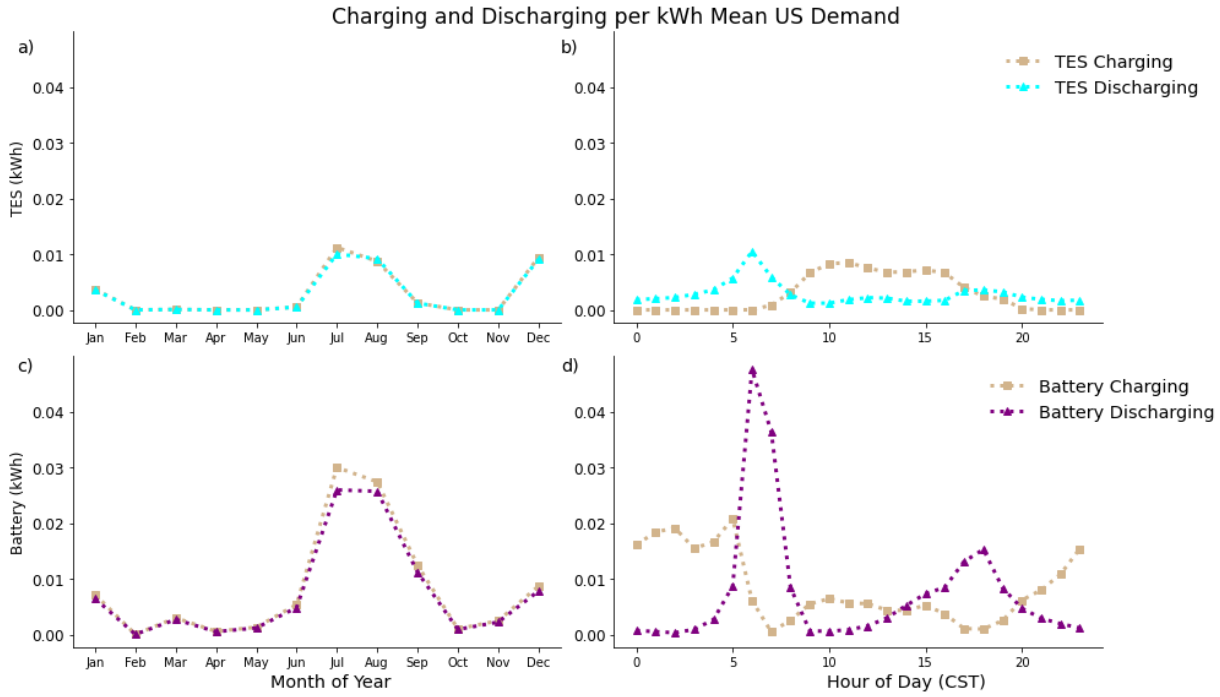

Figure A.5. Average charging/discharging in each month of the year for TES (a) and batteries (c). Average charging/discharging each hour of the day for TES (b) and batteries (d). All plots produced using 2017 data, with generation from wind, PV, and CSP.

Without long-duration storage in the system, batteries and TES retained mutually similar temporal charging patterns. Both storage technologies were used less without PGP than with PGP in the least-cost systems. This change correlates with the increase in overbuilding of generation observed in Fig. 4.2.

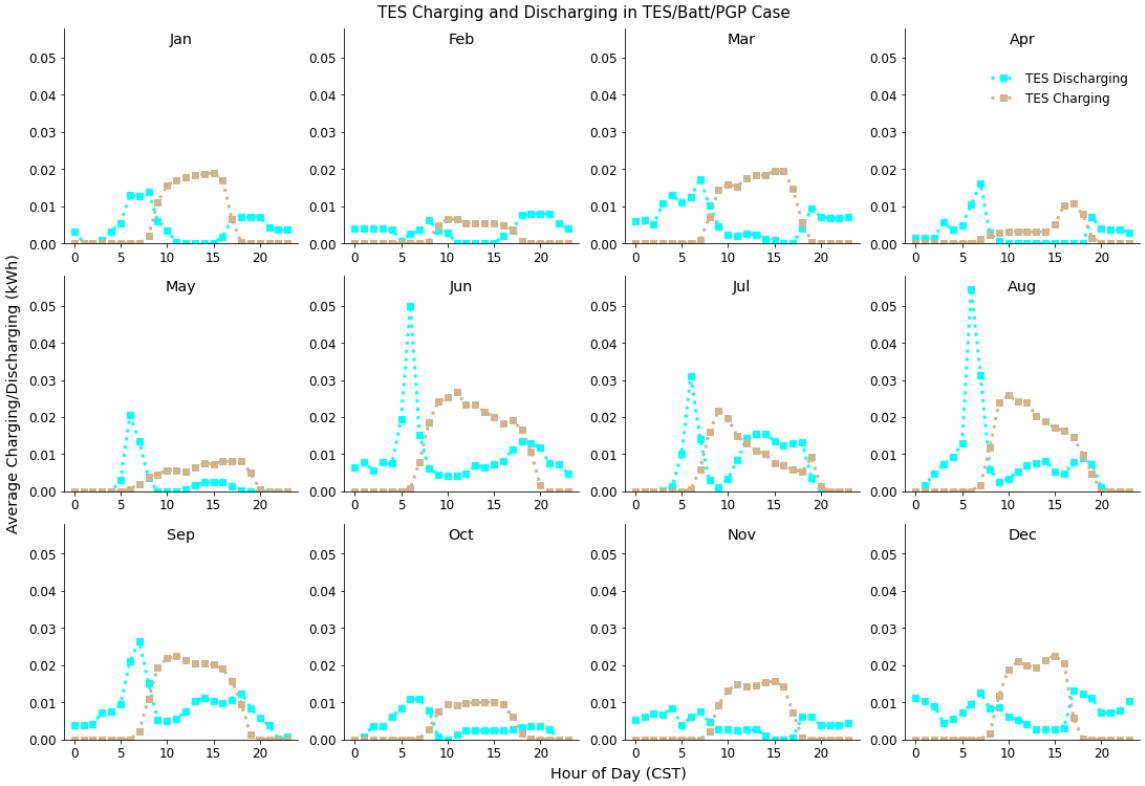

Figure A.6. Average hourly charging and discharging behavior for TES in each month of the year in the base case system. Here, TES is used regularly year-round.

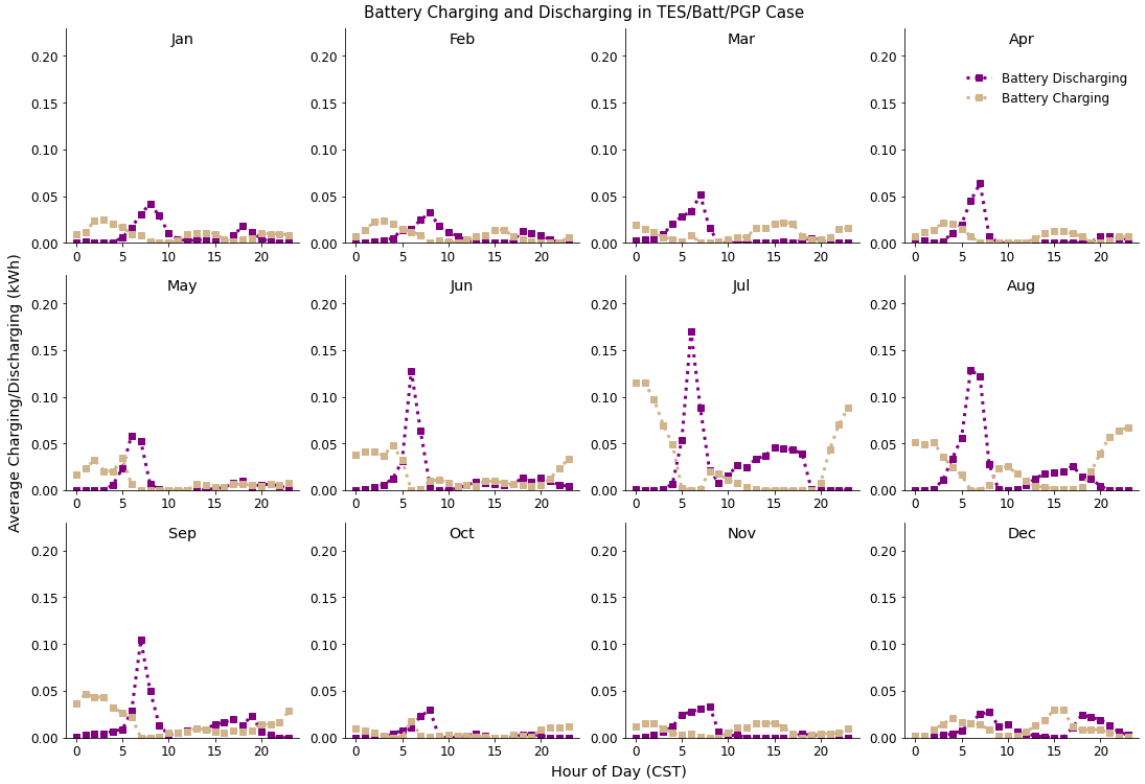

Figure A.7. Average hourly charging and discharging behavior for batteries in each month of the year in the base case system. Here, batteries are used year-round.

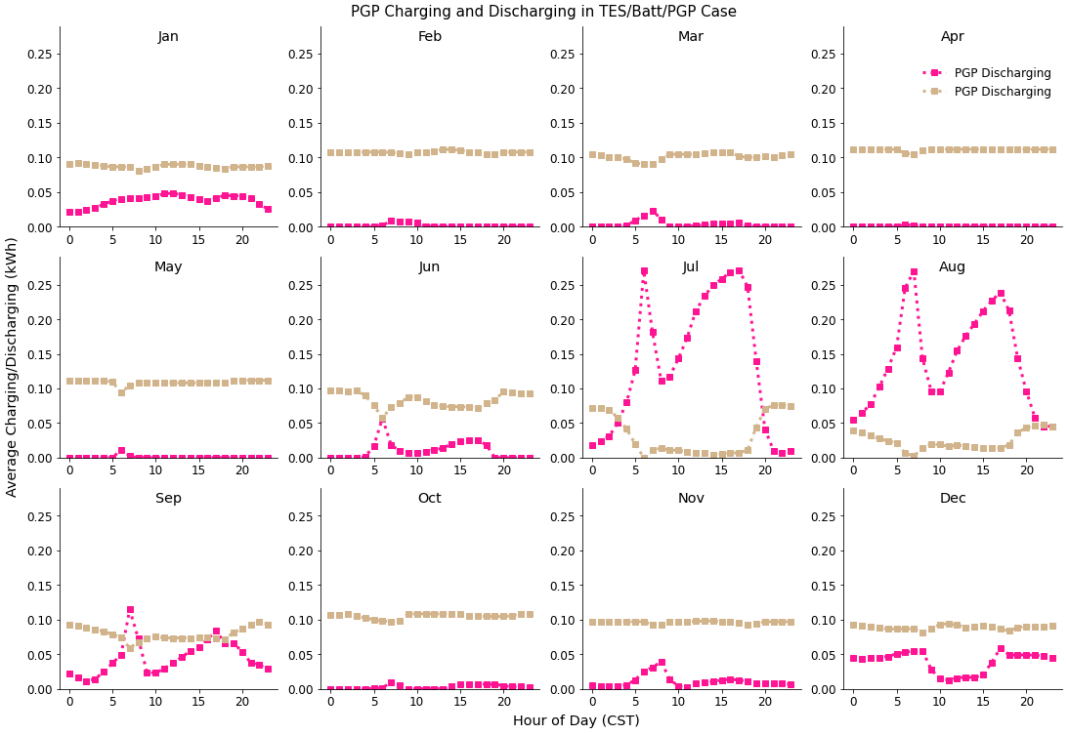

Figure A.8. Average hourly charging and discharging behavior for PGP in each month of the year for the base case system. PGP charges year round, but discharges in summer and winter months to compensate for low wind and solar resources, respectively.

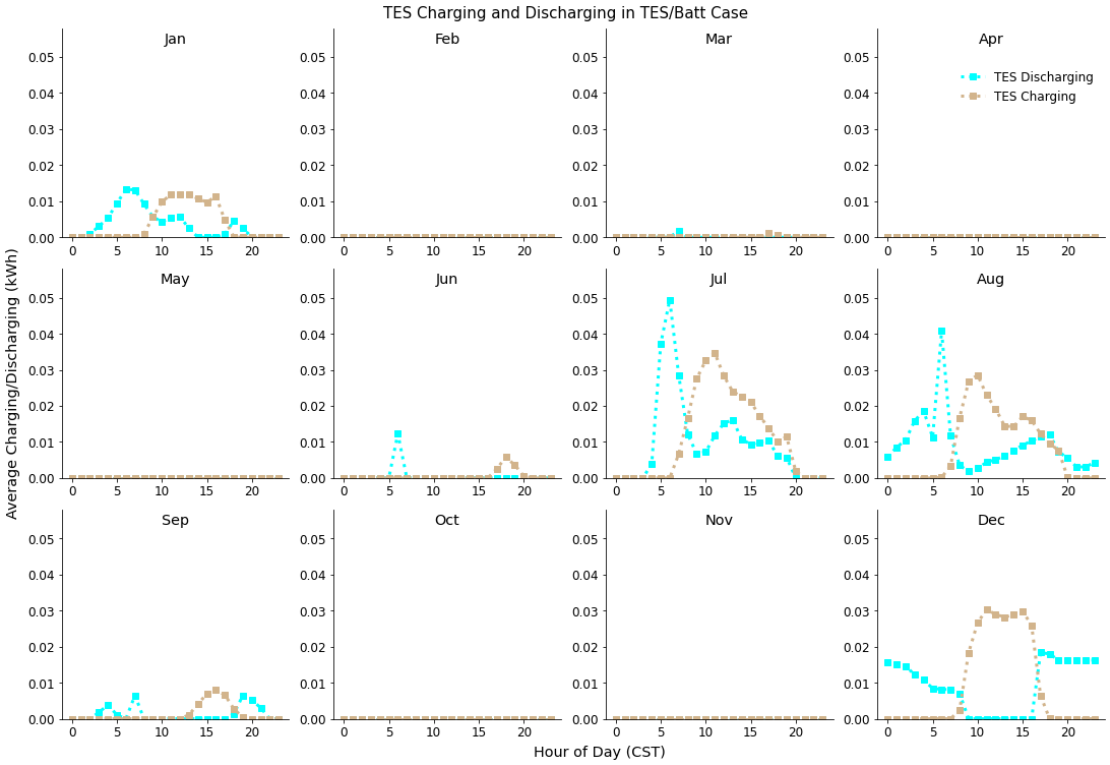

Figure A.9. Average hourly charging and discharging behavior for system without long-duration storage from PGP. Here, TES is only used on a large scale in summer and winter months to compensate for low wind and solar resources, respectively.

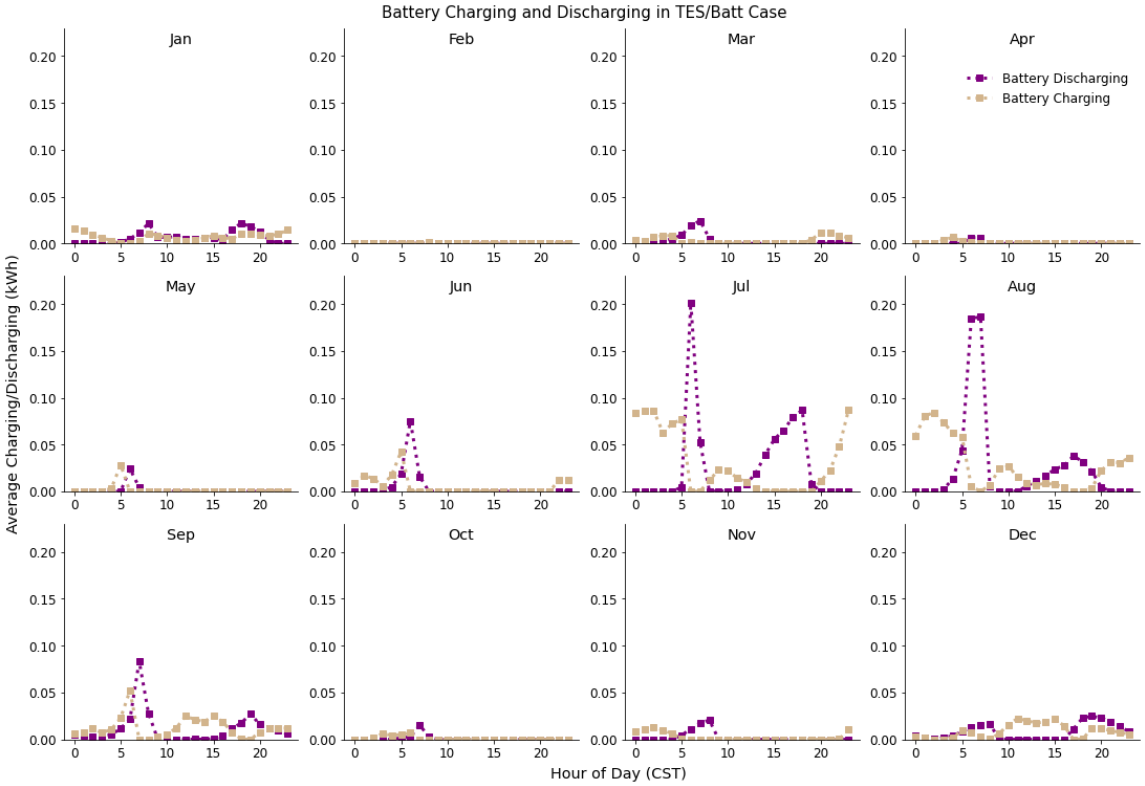

Figure A.10. Average hourly charging and discharging for batteries for system without long-duration storage from PGP. Here, batteries are used on a large scale in summer and winter months to compensate for low wind and solar resources, respectively, with smaller peaks in the interim months.

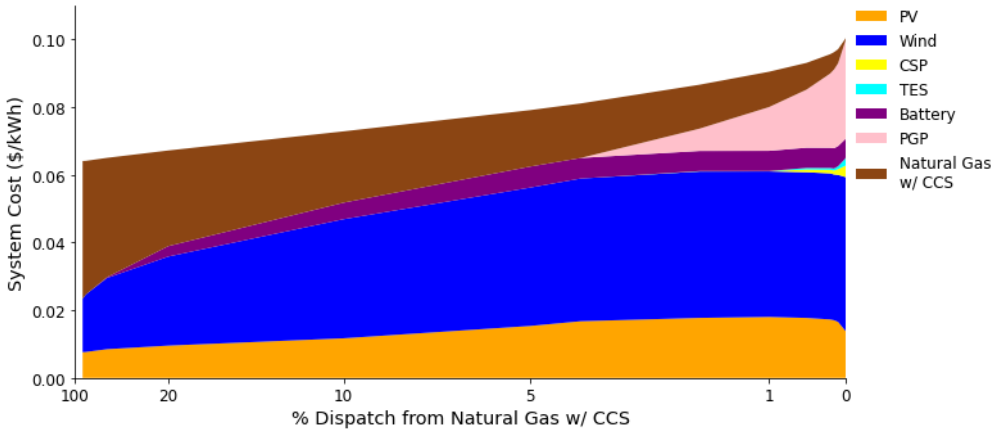

Figure A.11. System response when the capacity of natural gas with CCS is fixed, plotted against the percentage of demand in kWh met by renewable sources.

Under these constraints and with our specific demand and resource curves, the first renewable technologies to be deployed in a least-cost system including natural gas with 90% CCS were solar PV and wind turbines. The same stable system configuration was built for systems where the constraint on natural gas with CCS was ≥45% of dispatch. Flexibility provided by storage technologies first appeared when batteries entered the system at ~30% natural gas and PGP entered at ~3% natural gas. CSP+TES was built soon after when natural gas was constrained to meet no more than ~2.5% of demand. Here, CSP+TES was still the last technology chosen to meet the flexibility needs of the system, as in Figure 4 (b), but entered much earlier due to the higher cost of natural gas with CCS technology.

Technology Capacities	All Storage		Battery+PGP		TES+PGP		TES+Battery	
	100%	LL	100%	LL	100%	LL	100%	LL
PV	0.94	1.11	0.94	1.11	0.91	0.96	1.17	1.30
Wind	2.86	2.71	2.85	2.72	2.87	2.76	4.07	3.86
CSP Generation	0.06	0.01	0	0	0.12	0.12	0.18	0.16
CSP Turbine	0.11	0.03	0	0	0.28	0.21	0.25	0.21
TES	1.38	0.34	-	-	1.71	1.27	3.86	3.12
Battery	0.78	1.02	1.16	1.02	-	-	1.43	1.30
Electrolyzer	0.11	0.11	0.13	0.11	0.12	0.12	-	-
Fuel Cell	0.42	0.40	0.49	0.43	0.45	0.45	-	-
H_2 Storage	198	182	215	184	206	210	-	-

Technology Capacities	TES only		Battery Only	
	100%	LL	100%	LL
PV	1.20	1.28	1.41	1.62
Wind	4.03	3.90	5.17	4.00
CSP Generation	0.35	0.35	0	0
CSP Turbine	0.61	0.47	0	0
TES	5.46	3.90	-	-
Battery	-	-	2.05	2.07
Electrolyzer	-	-	-	-
Fuel Cell	-	-	-	-
H_2 Storage	-	-	-	-

Table A.4. Capacities built for each combination of storage technology when using all generation technologies, with comparisons for 100% reliable systems and the same system with lost load (LL). All values normalized to mean hourly demand.

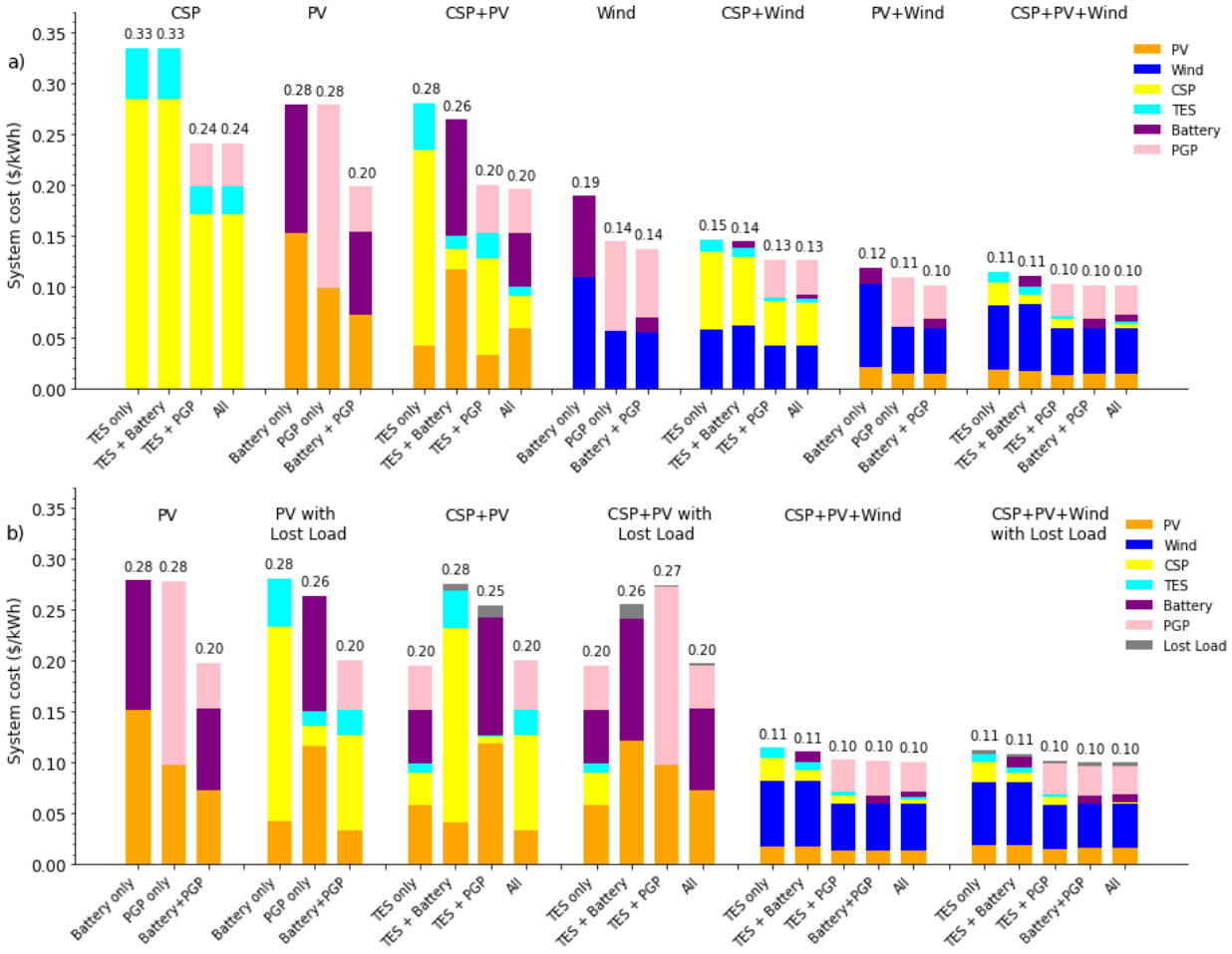

Figure A.12. Technology combinations for generation and storage. Part (a) requires a 100% reliable grid, and part (b) shows comparisons with lost load.

The highest amount of unmet demand observed for any case in Fig. A.12 (b) was 0.135% (11.83 hours) of total demand for the year, which occurred when only PV and batteries were deployed. This percentage of unmet demand decreased to 0.12% (10.62 hours) for CSP+PV with TES+batteries and to 0.03% (2.76 hours) of total demand when all generation and storage technologies could be deployed. All exceeded the NERC standard of 1 hour of unmet demand in a decade.[74]

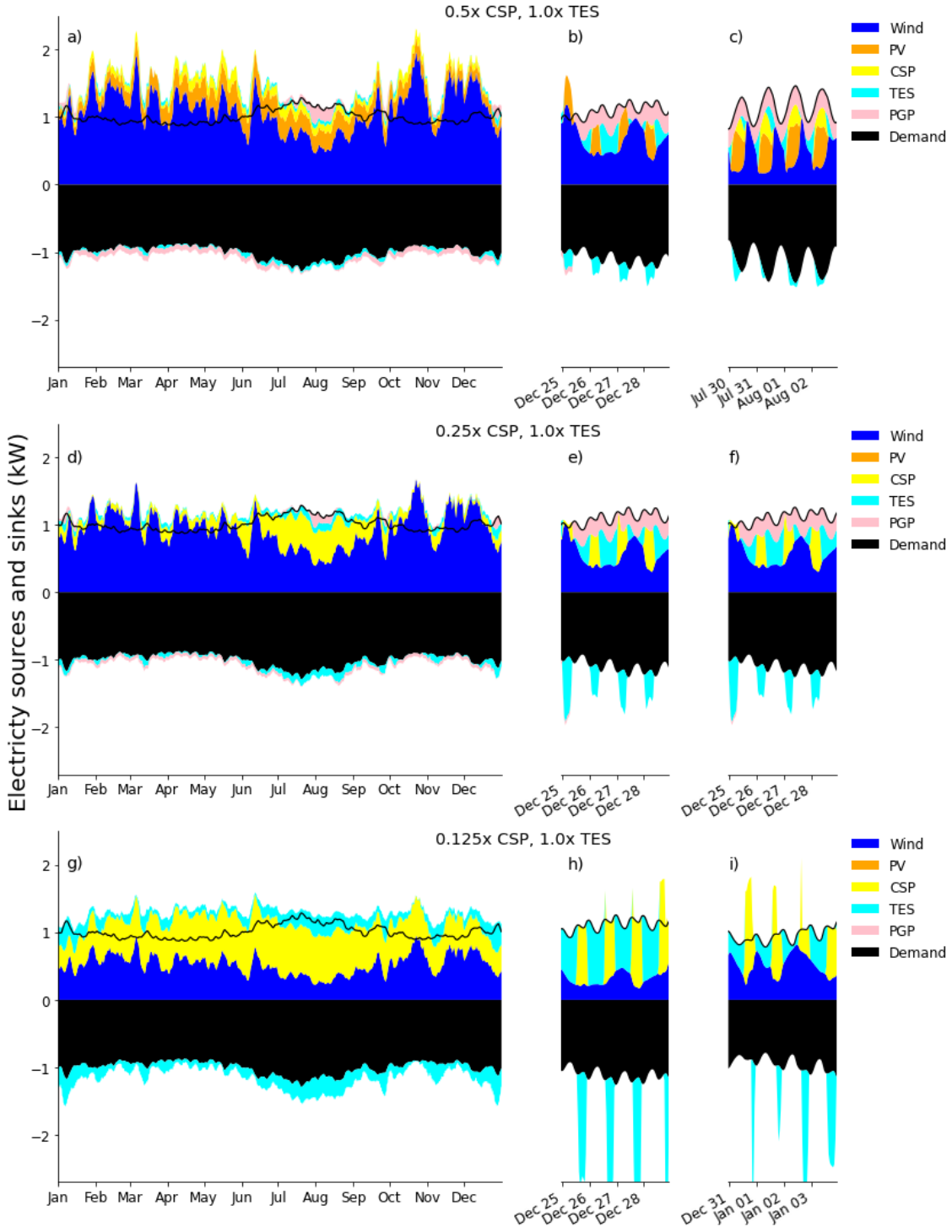

Figure A.13. Dispatch curves for system with varying CSP costs. Annual curve with 5-day averaging in (a) for 0.5x CSP cost. Four days of maximum dispatch for TES and PGP in (b) and (c), respectively. Annual curve with 5-day averaging in (d) for 0.25x CSP cost. Four days of maximum

dispatch for TES and PGP in (e) and (f), respectively. Annual curve with 5-day averaging in (g) for 0.125x CSP cost. Four days of maximum dispatch for TES and PGP in (h) and (i), respectively.

Fig. A.13 shows that even at 0.5x of base case costs, PV generation still exceeded deployment of CSP. Instead, the decrease in CSP costs primarily led to greater usage of TES. At 0.25x cost, CSP took on a bulk generation role, though primarily during summer. At 0.125x of base case costs, CSP provided bulk generation year-round.

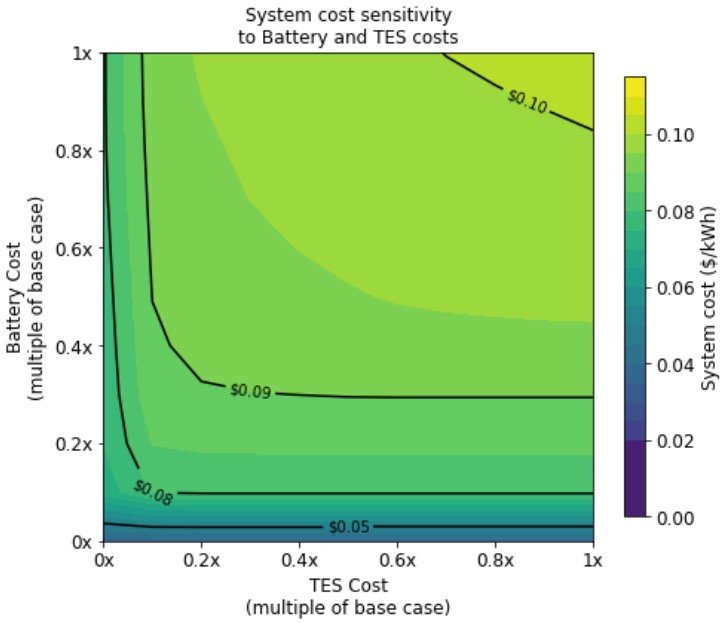

Figure A.14. Contour plot of cost variation for batteries and TES. Decreases in battery costs produced greater decreases in system costs compared to TES costs, as seen by the steeper gradient in the vertical direction.

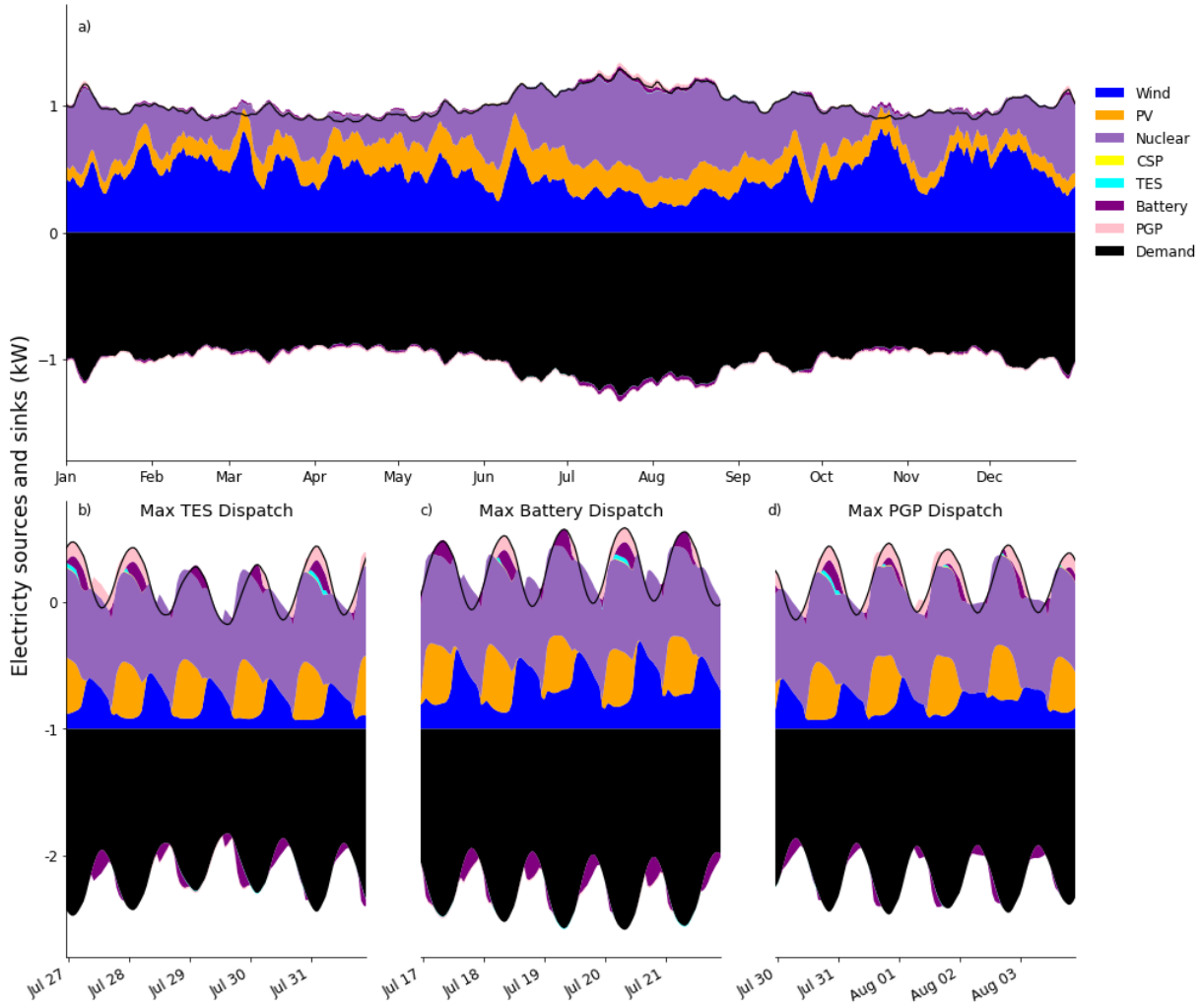

Figure A.15. Dispatch curve for 2017 data with 5-day averaging for the base case plus nuclear in (a). The panels in (b), (c), and (d) show hourly dispatch for the 5-day periods of maximum dispatch from TES, batteries, and PGP, respectively.

While nuclear does take on a large role in this case, small amounts of battery, PGP, and CSP+TES storage were still used in the system. This accords with the analysis of renewable portfolio standards which shows usage of storage technologies even with low penetrations of variable renewables.

BIBLIOGRAPHY

(1) Ager, J. W.; Shaner, M. R.; Walczak, K. A.; Sharp, I. D.; Ardo, S. Experimental Demonstrations of Spontaneous, Solar-Driven Photoelectrochemical Water Splitting. *Energy Environ. Sci.* **2015**, *8* (10), 2811–2824. https://doi.org/10.1039/C5EE00457H.

(2) Fountaine, K. T.; Kendall, C. G.; Atwater, H. A. Near-Unity Broadband Absorption Designs for Semiconducting Nanowire Arrays via Localized Radial Mode Excitation. *Opt. Express* **2014**, *22* (S3), A930. https://doi.org/10.1364/OE.22.00A930.

(3) National Oceanic and Atmospheric Administration. 2020 Was Earth's 2nd-Hottest Year, Just behind 2016, 2021.

(4) Cook, J.; Oreskes, N.; Doran, P. T.; Anderegg, W. R. L.; Verheggen, B.; Maibach, E. W.; Carlton, J. S.; Lewandowsky, S.; Skuce, A. G.; Green, S. A.; Nuccitelli, D.; Jacobs, P.; Richardson, M.; Winkler, B.; Painting, R.; Rice, K. Consensus on Consensus: A Synthesis of Consensus Estimates on Human-Caused Global Warming. *Environ. Res. Lett.* **2016**, *11* (4), 048002. https://doi.org/10.1088/1748-9326/11/4/048002.

(5) Oreskes, N. The Scientific Consensus on Climate Change. *Science* **2004**, *306* (5702), 1686–1686. https://doi.org/10.1126/science.1103618.

(6) Core Writing Team; Pachauri, R. K.; Meyer, L. A. *Climate Change 2014: Synthesis Report. Contribution of Working Groups I, II and III to the Fifth Assessment Report of the Intergovernmental Panel on Climate Change*; IPCC: Geneva, Switzerland, 2014.

(7) Lenssen, N. J. L.; Schmidt, G. A.; Hansen, J. E.; Menne, M. J.; Persin, A.; Ruedy, R.; Zyss, D. Improvements in the GISTEMP Uncertainty Model. *J. Geophys. Res. Atmospheres* **2019**, *124* (12), 6307–6326. https://doi.org/10.1029/2018JD029522.

(8) Hoegh-Guldberg, O.; Jacob, D.; Taylor, M.; Bindi, M.; Brown, S.; Camilloni, I.; Diedhiou, A.; Djalante, R.; Ebi, K. L.; Engelbrecht, F.; Guiot, J.; Hijioka, Y.; Mehrotra, S.; Payne, A.; Seneviratne, S. I.; Thomas, A.; Warren, R.; Zhou, G. *Impacts of 1.5ºC Global Warming on Natural and Human Systems. In: Global Warming of 1.5°C. An IPCC Special Report on the Impacts of Global Warming of 1.5°C above Pre-Industrial Levels and Related Global Greenhouse Gas Emission Pathways, in the Context of Strengthening the Global Response to the Threat of Climate Change, Sustainable Development, and Efforts to Eradicate Poverty*; Masson-Delmotte, V., Zhai, P., Pörtner, H.-O., Roberts, D., Skea, J., Shukla, P. R., Pirani, A., Moufouma-Okia, W., Péan, C., Pidcock, R., Connors, S., Matthews, J. B. R., Chen, Y., Zhou, X., Gomis, M. I., Lonnoy, E., Maycock, T., Tignor, M., Waterfield, T., Series Eds.; IPCC, 2018.

(9) *Summary for Policymakers. In: IPCC Special Report on the Ocean and Cryosphere in a Changing Climate*; Pörtner, H.-O., Roberts, D., Masson-Delmotte, V., Zhai, P., Tignor, M., Poloczanska, E., Mintenbeck, K., Alegría, A., Nicolai, M., Okem, A., Petzold, J., Rama, B., Weyer, N. M., Series Eds.; IPCC, 2019.

(10) The Paris Agreement | UNFCCC https://unfccc.int/process-and-meetings/the-paris-agreement/the-paris-agreement (accessed Apr 12, 2021).

(11) Rogelj, J.; Shindell, D.; Jiang, K.; Fifita, S.; Forster, P.; Ginzburg, V.; Handa, C.; Kheshgi, H.; Kobayashi, S.; Kriegler, E.; Mundaca, L.; Séférian, R.; Vilariño, M. V. *Mitigation*

Pathways Compatible with 1.5°C in the Context of Sustainable Development. In: Global Warming of 1.5°C. An IPCC Special Report on the Impacts of Global Warming of 1.5°C above Pre-Industrial Levels and Related Global Greenhouse Gas Emission Pathways, in the Context of Strengthening the Global Response to the Threat of Climate Change, Sustainable Development, and Efforts to Eradicate Poverty; Masson-Delmotte, V., Zhai, P., Pörtner, H.-O., Roberts, D., Skea, J., Shukla, P. R., Pirani, A., Moufouma-Okia, W., Péan, C., Pidcock, R., Connors, S., Matthews, J. B. R., Chen, Y., Zhou, X., Gomis, M. I., Lonnoy, E., Maycock, T., Tignor, M., Waterfield, T., Series Eds.; IPCC, 2018.

(12) *International Energy Outlook 2019*; U.S. Energy Information Administration: Washington, DC, 2019.

(13) *Annual Energy Outlook 2021*; U.S. Energy Information Administration: Washington, DC, 2021.

(14) Davis, S. J.; Lewis, N. S.; Shaner, M.; Aggarwal, S.; Arent, D.; Azevedo, I. L.; Benson, S. M.; Bradley, T.; Brouwer, J.; Chiang, Y.-M.; Clack, C. T. M.; Cohen, A.; Doig, S.; Edmonds, J.; Fennell, P.; Field, C. B.; Hannegan, B.; Hodge, B.-M.; Hoffert, M. I.; Ingersoll, E.; Jaramillo, P.; Lackner, K. S.; Mach, K. J.; Mastrandrea, M.; Ogden, J.; Peterson, P. F.; Sanchez, D. L.; Sperling, D.; Stagner, J.; Trancik, J. E.; Yang, C.-J.; Caldeira, K. Net-Zero Emissions Energy Systems. *Science* **2018**, *360* (6396), eaas9793. https://doi.org/10.1126/science.aas9793.

(15) Shaner, M. R.; Davis, S. J.; Lewis, N. S.; Caldeira, K. Geophysical Constraints on the Reliability of Solar and Wind Power in the United States. *Energy Environ. Sci.* **2018**, *11* (4), 914–925. https://doi.org/10.1039/C7EE03029K.

(16) Jenkins, J. D.; Luke, M.; Thernstrom, S. Getting to Zero Carbon Emissions in the Electric Power Sector. *Joule* **2018**, *2* (12), 2498–2510. https://doi.org/10.1016/j.joule.2018.11.013.

(17) Rinaldi, K. Z.; Dowling, J. A.; Ruggles, T. H.; Caldeira, K.; Lewis, N. S. Wind and Solar Resource Droughts in California Highlight the Benefits of Long-Term Storage and Integration with the Western Interconnect. *Environ. Sci. Technol.* **2021**, acs.est.0c07848. https://doi.org/10.1021/acs.est.0c07848.

(18) Mai, T.; Jadun, P.; Logan, J.; McMillan, C.; Muratori, M.; Steinberg, D.; Vimmerstedt, L.; Jones, R.; Haley, B.; Nelson, B. *Electrification Futures Study: Scenarios of Electric Technology Adoption and Power Consumption for the United States*; NREL/TP-6A20-71500; National Renewable Energy Laboratory: Golden, CO, 2018.

(19) Sepulveda, N. A.; Jenkins, J. D.; de Sisternes, F. J.; Lester, R. K. The Role of Firm Low-Carbon Electricity Resources in Deep Decarbonization of Power Generation. *Joule* **2018**, *2* (11), 2403–2420. https://doi.org/10.1016/j.joule.2018.08.006.

(20) Dowling, J. A.; Rinaldi, K. Z.; Ruggles, T. H.; Davis, S. J.; Yuan, M.; Tong, F.; Lewis, N. S.; Caldeira, K. Role of Long-Duration Energy Storage in Variable Renewable Electricity Systems. *Joule* **2020**, *4* (9), 1907–1928. https://doi.org/10.1016/j.joule.2020.07.007.

(21) Mai, T.; Sandor, D.; Wiser, R.; Schneider, T. *Renewable Electricity Futures Study: Executive Summary*; NREL/TP-6A20-52409-ES; National Renewable Energy Laboratory: Golden, CO, 2012.

(22) Pleßmann, G.; Blechinger, P. How to Meet EU GHG Emission Reduction Targets? A Model Based Decarbonization Pathway for Europe's Electricity Supply System until 2050. *Energy Strategy Rev.* **2017**, *15*, 19–32. https://doi.org/10.1016/j.esr.2016.11.003.

(23) Yuan, M.; Tong, F.; Duan, L.; Dowling, J. A.; Davis, S. J.; Lewis, N. S.; Caldeira, K. Would Firm Generators Facilitate or Deter Variable Renewable Energy in a Carbon-Free Electricity System? *Appl. Energy* **2020**, *279*, 115789. https://doi.org/10.1016/j.apenergy.2020.115789.
(24) Cole, W.; Frazier, A. W. *Cost Projections for Utility-Scale Battery Storage: 2020 Update*; NREL/TP-6A20-75385; National Renewable Energy Laboratory: Golden, CO, 2020.
(25) Turchi, C.; Heath, G. *Molten Salt Power Tower Cost Model for the System Advisor Model (SAM)*; NREL/TP-5500-57625; National Renewable Energy Laboratory: Golden, CO, 2013.
(26) Kurup, P.; Turchi, C. *Parabolic Trough Collector Cost Update for the System Advisor Model (SAM)*; NREL/TP-6A20-65228; National Renewable Energy Laboratory: Golden, CO, 2015.
(27) Achkari, O.; El Fadar, A. Latest Developments on TES and CSP Technologies – Energy and Environmental Issues, Applications and Research Trends. *Appl. Therm. Eng.* **2020**, *167*, 114806. https://doi.org/10.1016/j.applthermaleng.2019.114806.
(28) Replogle, M.; Fulton, L. *A Global High Shift Scenario: Impacts And Potential For More Public Transport, Walking, And Cycling With Lower Car Use*; Institute for Transportation and Development Policy: New York, NY, 2014.
(29) *Climate Action Pathway Transport Executive Summary*; United Nations, Marrakech Partnership, 2020; p 17.
(30) Zenith, F.; Isaac, R.; Hoffrichter, A.; Thomassen, M. S.; Møller-Holst, S. Techno-Economic Analysis of Freight Railway Electrification by Overhead Line, Hydrogen and Batteries: Case Studies in Norway and USA. *Proc. Inst. Mech. Eng. Part F J. Rail Rapid Transit* **2020**, *234* (7), 791–802. https://doi.org/10.1177/0954409719867495.
(31) Ivanenko, A. Council Post: Get Ready: The Hydrogen Economy Is On Its Way https://www.forbes.com/sites/forbestechcouncil/2021/03/11/get-ready-the-hydrogen-economy-is-on-its-way/ (accessed Apr 16, 2021).
(32) Wang, M. Fuel Choices for Fuel-Cell Vehicles: Well-to-Wheels Energy and Emission Impacts. *J. Power Sources* **2002**, *112* (1), 307–321. https://doi.org/10.1016/S0378-7753(02)00447-0.
(33) Velazquez Abad, A.; Dodds, P. E. Green Hydrogen Characterisation Initiatives: Definitions, Standards, Guarantees of Origin, and Challenges. *Energy Policy* **2020**, *138*, 111300. https://doi.org/10.1016/j.enpol.2020.111300.
(34) Warren, E. L.; Atwater, H. A.; Lewis, N. S. Silicon Microwire Arrays for Solar Energy-Conversion Applications. *J. Phys. Chem. C* **2014**, *118* (2), 747–759. https://doi.org/10.1021/jp406280x.
(35) Ahmed, M.; Dincer, I. A Review on Photoelectrochemical Hydrogen Production Systems: Challenges and Future Directions. *Int. J. Hydrog. Energy* **2019**, *44* (5), 2474–2507. https://doi.org/10.1016/j.ijhydene.2018.12.037.
(36) *Photoelectrochemical Hydrogen Production*; van de Krol, R., Grätzel, M., Eds.; Electronic Materials: Science & Technology; Springer US: Boston, MA, 2012; Vol. 102. https://doi.org/10.1007/978-1-4614-1380-6.
(37) Saadi, F. H.; Lewis, N. S.; McFarland, E. W. Relative Costs of Transporting Electrical and Chemical Energy. *Energy Environ. Sci.* **2018**, *11* (3), 469–475. https://doi.org/10.1039/C7EE01987D.
(38) Kittel, C.; McEuen, P.; John Wiley & Sons. *Introduction to Solid State Physics*; 2015.

(39) Jiang, C.; Moniz, S. J. A.; Wang, A.; Zhang, T.; Tang, J. Photoelectrochemical Devices for Solar Water Splitting – Materials and Challenges. *Chem. Soc. Rev.* **2017**, *46* (15), 4645–4660. https://doi.org/10.1039/C6CS00306K.
(40) Walter, M. G.; Warren, E. L.; McKone, J. R.; Boettcher, S. W.; Mi, Q.; Santori, E. A.; Lewis, N. S. Solar Water Splitting Cells. *Chem. Rev.* **2010**, *110* (11), 6446–6473. https://doi.org/10.1021/cr1002326.
(41) Hu, S.; Xiang, C.; Haussener, S.; Berger, A. D.; Lewis, N. S. An Analysis of the Optimal Band Gaps of Light Absorbers in Integrated Tandem Photoelectrochemical Water-Splitting Systems. *Energy Environ. Sci.* **2013**, *6* (10), 2984. https://doi.org/10.1039/c3ee40453f.
(42) Lewis, N. S. Developing a Scalable Artificial Photosynthesis Technology through Nanomaterials by Design. *Nat. Nanotechnol.* **2016**, *11* (12), 1010–1019. https://doi.org/10.1038/nnano.2016.194.
(43) Spurgeon, J. M.; Walter, M. G.; Zhou, J.; Kohl, P. A.; Lewis, N. S. Electrical Conductivity, Ionic Conductivity, Optical Absorption, and Gas Separation Properties of Ionically Conductive Polymer Membranes Embedded with Si Microwire Arrays. *Energy Environ. Sci.* **2011**, *4* (5), 1772. https://doi.org/10.1039/c1ee01028j.
(44) Liu, C.; Dasgupta, N. P.; Yang, P. Semiconductor Nanowires for Artificial Photosynthesis. *Chem. Mater.* **2014**, *26* (1), 415–422. https://doi.org/10.1021/cm4023198.
(45) Ardo, S.; Park, S. H.; Warren, E. L.; Lewis, N. S. Unassisted Solar-Driven Photoelectrosynthetic HI Splitting Using Membrane-Embedded Si Microwire Arrays. *Energy Environ. Sci.* **2015**, *8* (5), 1484–1492. https://doi.org/10.1039/C5EE00227C.
(46) Kempler, P. A.; Coridan, R. H.; Lewis, N. S. Effects of Bubbles on the Electrochemical Behavior of Hydrogen-Evolving Si Microwire Arrays Oriented against Gravity. *Energy Environ. Sci.* **2020**, *13* (6), 1808–1817. https://doi.org/10.1039/D0EE00356E.
(47) Yalamanchili, S.; Emmer, H. S.; Fountaine, K. T.; Chen, C. T.; Lewis, N. S.; Atwater, H. A. Enhanced Absorption and <1% Spectrum-and-Angle-Averaged Reflection in Tapered Microwire Arrays. *ACS Photonics* **2016**, *3* (10), 1854–1861. https://doi.org/10.1021/acsphotonics.6b00370.
(48) Wu, F.; Lin, H.; Yang, Z.; Liao, M.; Wang, Z.; Li, Z.; Gao, P.; Ye, J.; Shen, W. Suppression of Surface and Auger Recombination by Formation and Control of Radial Junction in Silicon Microwire Solar Cells. *Nano Energy* **2019**, *58*, 817–824. https://doi.org/10.1016/j.nanoen.2019.02.021.
(49) Ritenour, A. J.; Levinrad, S.; Bradley, C.; Cramer, R. C.; Boettcher, S. W. Electrochemical Nanostructuring of *n* -GaAs Photoelectrodes. *ACS Nano* **2013**, *7* (8), 6840–6849. https://doi.org/10.1021/nn4020104.
(50) Kelzenberg, M. D.; Boettcher, S. W.; Petykiewicz, J. A.; Turner-Evans, D. B.; Putnam, M. C.; Warren, E. L.; Spurgeon, J. M.; Briggs, R. M.; Lewis, N. S.; Atwater, H. A. Enhanced Absorption and Carrier Collection in Si Wire Arrays for Photovoltaic Applications. *Nat. Mater.* **2010**, *9* (3), 239–244. https://doi.org/10.1038/nmat2635.
(51) Kempler, P. A.; Gonzalez, M. A.; Papadantonakis, K. M.; Lewis, N. S. Hydrogen Evolution with Minimal Parasitic Light Absorption by Dense Co–P Catalyst Films on Structured p-Si Photocathodes. *ACS Energy Lett.* **2018**, *3* (3), 612–617. https://doi.org/10.1021/acsenergylett.8b00034.
(52) Yalamanchili, S.; Kempler, P. A.; Papadantonakis, K. M.; Atwater, H. A.; Lewis, N. S. Integration of Electrocatalysts with Silicon Microcone Arrays for Minimization of Optical

and Overpotential Losses during Sunlight-Driven Hydrogen Evolution. *Sustain. Energy Fuels* **2019**, *3* (9), 2227–2236. https://doi.org/10.1039/C9SE00294D.

(53) Vijselaar, W.; Tiggelaar, R. M.; Gardeniers, H.; Huskens, J. Efficient and Stable Silicon Microwire Photocathodes with a Nickel Silicide Interlayer for Operation in Strongly Alkaline Solutions. *ACS Energy Lett.* **2018**, *3* (5), 1086–1092. https://doi.org/10.1021/acsenergylett.8b00267.

(54) Vijselaar, W.; Westerik, P.; Veerbeek, J.; Tiggelaar, R. M.; Berenschot, E.; Tas, N. R.; Gardeniers, H.; Huskens, J. Spatial Decoupling of Light Absorption and Catalytic Activity of Ni–Mo-Loaded High-Aspect-Ratio Silicon Microwire Photocathodes. *Nat. Energy* **2018**, *3* (3), 185–192. https://doi.org/10.1038/s41560-017-0068-x.

(55) Shaner, M. R.; Hu, S.; Sun, K.; Lewis, N. S. Stabilization of Si Microwire Arrays for Solar-Driven H_2O Oxidation to O_2 (g) in 1.0 M KOH(Aq) Using Conformal Coatings of Amorphous TiO_2. *Energy Environ. Sci.* **2015**, *8* (1), 203–207. https://doi.org/10.1039/C4EE03012E.

(56) Hu, S.; Shaner, M. R.; Beardslee, J. A.; Lichterman, M.; Brunschwig, B. S.; Lewis, N. S. Amorphous TiO2 Coatings Stabilize Si, GaAs, and GaP Photoanodes for Efficient Water Oxidation. *Science* **2014**, *344* (6187), 1005–1009. https://doi.org/10.1126/science.1251428.

(57) Bae, D.; Seger, B.; Vesborg, P. C. K.; Hansen, O.; Chorkendorff, I. Strategies for Stable Water Splitting via Protected Photoelectrodes. *Chem. Soc. Rev.* **2017**, *46* (7), 1933–1954. https://doi.org/10.1039/C6CS00918B.

(58) Kistler, T. A.; Larson, D.; Walczak, K.; Agbo, P.; Sharp, I. D.; Weber, A. Z.; Danilovic, N. Integrated Membrane-Electrode-Assembly Photoelectrochemical Cell under Various Feed Conditions for Solar Water Splitting. *J. Electrochem. Soc.* **2019**, *166* (5), H3020–H3028. https://doi.org/10.1149/2.0041905jes.

(59) Ducom, G.; Laubie, B.; Ohannessian, A.; Chottier, C.; Germain, P.; Chatain, V. Hydrolysis of Polydimethylsiloxane Fluids in Controlled Aqueous Solutions. *Water Sci. Technol.* **2013**, *68* (4), 813–820. https://doi.org/10.2166/wst.2013.308.

(60) Scheuermann, A. G.; McIntyre, P. C. Atomic Layer Deposited Corrosion Protection: A Path to Stable and Efficient Photoelectrochemical Cells. *J. Phys. Chem. Lett.* **2016**, *7* (14), 2867–2878. https://doi.org/10.1021/acs.jpclett.6b00631.

(61) Bae, D.; Shayestehaminzadeh, S.; Thorsteinsson, E. B.; Pedersen, T.; Hansen, O.; Seger, B.; Vesborg, P. C. K.; Ólafsson, S.; Chorkendorff, I. Protection of Si Photocathode Using TiO2 Deposited by High Power Impulse Magnetron Sputtering for H2 Evolution in Alkaline Media. *Sol. Energy Mater. Sol. Cells* **2016**, *144*, 758–765. https://doi.org/10.1016/j.solmat.2015.10.020.

(62) Lee, D. K.; Choi, K.-S. Enhancing Long-Term Photostability of BiVO4 Photoanodes for Solar Water Splitting by Tuning Electrolyte Composition. *Nat. Energy* **2018**, *3* (1), 53–60. https://doi.org/10.1038/s41560-017-0057-0.

(63) Burton, N. A.; Padilla, R. V.; Rose, A.; Habibullah, H. Increasing the Efficiency of Hydrogen Production from Solar Powered Water Electrolysis. *Renew. Sustain. Energy Rev.* **2021**, *135*, 110255. https://doi.org/10.1016/j.rser.2020.110255.

(64) Ardo, S.; Fernandez Rivas, D.; Modestino, M. A.; Schulze Greiving, V.; Abdi, F. F.; Alarcon Llado, E.; Artero, V.; Ayers, K.; Battaglia, C.; Becker, J.-P.; Bederak, D.; Berger, A.; Buda, F.; Chinello, E.; Dam, B.; Di Palma, V.; Edvinsson, T.; Fujii, K.; Gardeniers, H.; Geerlings, H.; H. Hashemi, S. M.; Haussener, S.; Houle, F.; Huskens, J.; James, B. D.; Konrad, K.;

Kudo, A.; Kunturu, P. P.; Lohse, D.; Mei, B.; Miller, E. L.; Moore, G. F.; Muller, J.; Orchard, K. L.; Rosser, T. E.; Saadi, F. H.; Schüttauf, J.-W.; Seger, B.; Sheehan, S. W.; Smith, W. A.; Spurgeon, J.; Tang, M. H.; van de Krol, R.; Vesborg, P. C. K.; Westerik, P. Pathways to Electrochemical Solar-Hydrogen Technologies. *Energy Environ. Sci.* **2018**, *11* (10), 2768–2783. https://doi.org/10.1039/C7EE03639F.

(65) Verlage, E.; Hu, S.; Liu, R.; Jones, R. J. R.; Sun, K.; Xiang, C.; Lewis, N. S.; Atwater, H. A. A Monolithically Integrated, Intrinsically Safe, 10% Efficient, Solar-Driven Water-Splitting System Based on Active, Stable Earth-Abundant Electrocatalysts in Conjunction with Tandem III–V Light Absorbers Protected by Amorphous TiO_2 Films. *Energy Environ. Sci.* **2015**, *8* (11), 3166–3172. https://doi.org/10.1039/C5EE01786F.

(66) Fountaine, K. T.; Cheng, W.-H.; Bukowsky, C. R.; Atwater, H. A. Near-Unity Unselective Absorption in Sparse InP Nanowire Arrays. *ACS Photonics* **2016**, *3* (10), 1826–1832. https://doi.org/10.1021/acsphotonics.6b00341.

(67) Wu, D.; Tang, X.; Wang, K.; He, Z.; Li, X. An Efficient and Effective Design of InP Nanowires for Maximal Solar Energy Harvesting. *Nanoscale Res. Lett.* **2017**, *12* (1), 604. https://doi.org/10.1186/s11671-017-2354-8.

(68) Dhindsa, N.; Saini, S. S. Top-down Fabricated Tapered GaAs Nanowires with Sacrificial Etching of the Mask. *Nanotechnology* **2017**, *28* (23), 235301. https://doi.org/10.1088/1361-6528/aa6fe9.

(69) Baca, A. G.; Ashby, C. I. H. *Fabrication of GaAs Devices*; Processing series; Institution of Electrical Engineers: London, U.K, 2005.

(70) Dasog, M.; Carim, A. I.; Yalamanchili, S.; Atwater, H. A.; Lewis, N. S. Profiling Photoinduced Carrier Generation in Semiconductor Microwire Arrays via Photoelectrochemical Metal Deposition. *Nano Lett.* **2016**, *16* (8), 5015–5021. https://doi.org/10.1021/acs.nanolett.6b01782.

(71) Kennedy, K. M.; Kempler, P. A.; Cabán-Acevedo, M.; Papadantonakis, K. M.; Lewis, N. S. Primary Corrosion Processes for Polymer-Embedded Free-Standing or Substrate-Supported Silicon Microwire Arrays in Aqueous Alkaline Electrolytes. *Nano Lett.* **2021**, *21* (2), 1056–1061. https://doi.org/10.1021/acs.nanolett.0c04298.

(72) Shields, L. State Renewable Portfolio Standards and Goals https://www.ncsl.org/research/energy/renewable-portfolio-standards.aspx (accessed Feb 5, 2021).

(73) Sierra Club. Ready for 100: Committed https://www.sierraclub.org/ready-for-100/commitments (accessed Feb 5, 2021).

(74) Planning Resource Adequacy Analysis, Assessment and Documentation. North American Electric Reliability Corporation.

(75) Ardani, K.; Margolis, R. *2010 Solar Technologies Market Report*; National Renewable Energy Laboratory: Golden, CO, 2011.

(76) Fu, R.; Feldman, D.; Margolis, R. *U.S. Solar Photovoltaic System Cost Benchmark: Q1 2018*; NREL/TP-6A20-72399; National Renewable Energy Laboratory: Golden, CO, 2018.

(77) Boretti, A. Integration of Solar Thermal and Photovoltaic, Wind, and Battery Energy Storage through AI in NEOM City. *Energy AI* **2021**, *3*, 100038. https://doi.org/10.1016/j.egyai.2020.100038.

(78) Jorgenson, J.; Mehos, M.; Denholm, P. Comparing the Net Cost of CSP-TES to PV Deployed with Battery Storage; Cape Town, South Africa, 2016; p 080003. https://doi.org/10.1063/1.4949183.
(79) *Concentrating Solar Power Technology Brief*; International Renewable Energy Agency, 2013.
(80) Py, X.; Azoumah, Y.; Olives, R. Concentrated Solar Power: Current Technologies, Major Innovative Issues and Applicability to West African Countries. *Renew. Sustain. Energy Rev.* **2013**, *18*, 306–315. https://doi.org/10.1016/j.rser.2012.10.030.
(81) Agyekum, E. B.; Velkin, V. I. Optimization and Techno-Economic Assessment of Concentrated Solar Power (CSP) in South-Western Africa: A Case Study on Ghana. *Sustain. Energy Technol. Assess.* **2020**, *40*, 100763. https://doi.org/10.1016/j.seta.2020.100763.
(82) Madaeni, S. H.; Sioshansi, R.; Denholm, P. *Capacity Value of Concentrating Solar Power Plants*; NREL/TP-6A20-51253; National Renewable Energy Laboratory: Golden, CO, 2011.
(83) Jordaan, S. M.; Xu, Q.; Hobbs, B. F. Grid-Scale Life Cycle Greenhouse Gas Implications of Renewable, Storage, and Carbon Pricing Options. *Environ. Sci. Technol.* **2020**, *54* (17), 10435–10445. https://doi.org/10.1021/acs.est.0c01861.
(84) *Life Cycle Greenhouse Gas Emissions from Concentrating Solar Power*; NREL/FS-6A20-56416; National Renewable Energy Laboratory: Golden, CO, 2012.
(85) Powell, K. M.; Rashid, K.; Ellingwood, K.; Tuttle, J.; Iverson, B. D. Hybrid Concentrated Solar Thermal Power Systems: A Review. *Renew. Sustain. Energy Rev.* **2017**, *80*, 215–237. https://doi.org/10.1016/j.rser.2017.05.067.
(86) Angrisani, G.; Bizon, K.; Chirone, R.; Continillo, G.; Fusco, G.; Lombardi, S.; Marra, F. S.; Miccio, F.; Roselli, C.; Sasso, M.; Solimene, R.; Tariello, F.; Urciuolo, M. Development of a New Concept Solar-Biomass Cogeneration System. *Energy Convers. Manag.* **2013**, *75*, 552–560. https://doi.org/10.1016/j.enconman.2013.06.042.
(87) Trieb, F.; Nitsch, J.; Kronshage, S.; Schillings, C.; Brischke, L.-A.; Knies, G.; Czisch, G. Combined Solar Power and Desalination Plants for the Mediterranean Region — Sustainable Energy Supply Using Large-Scale Solar Thermal Power Plants. *Desalination* **2003**, *153* (1–3), 39–46. https://doi.org/10.1016/S0011-9164(02)01091-3.
(88) Gunawan, A.; Simmons, R. A.; Haynes, M. W.; Moreno, D.; Menon, A. K.; Hatzell, M. C.; Yee, S. K. Techno-Economics of Cogeneration Approaches for Combined Power and Desalination From Concentrated Solar Power. *J. Sol. Energy Eng.* **2019**, *141* (2), 021004. https://doi.org/10.1115/1.4042061.
(89) Schoeneberger, C. A.; McMillan, C. A.; Kurup, P.; Akar, S.; Margolis, R.; Masanet, E. Solar for Industrial Process Heat: A Review of Technologies, Analysis Approaches, and Potential Applications in the United States. *Energy* **2020**, *206*, 118083. https://doi.org/10.1016/j.energy.2020.118083.
(90) Soria, R.; Lucena, A. F. P.; Tomaschek, J.; Fichter, T.; Haasz, T.; Szklo, A.; Schaeffer, R.; Rochedo, P.; Fahl, U.; Kern, J. Modelling Concentrated Solar Power (CSP) in the Brazilian Energy System: A Soft-Linked Model Coupling Approach. *Energy* **2016**, *116*, 265–280. https://doi.org/10.1016/j.energy.2016.09.080.
(91) Mena, R.; Escobar, R.; Lorca, Á.; Negrete-Pincetic, M.; Olivares, D. The Impact of Concentrated Solar Power in Electric Power Systems: A Chilean Case Study. *Appl. Energy* **2019**, *235*, 258–283. https://doi.org/10.1016/j.apenergy.2018.10.088.

(92) Petrakopoulou, F.; Robinson, A.; Loizidou, M. Simulation and Evaluation of a Hybrid Concentrating-Solar and Wind Power Plant for Energy Autonomy on Islands. *Renew. Energy* **2016**, *96*, 863–871. https://doi.org/10.1016/j.renene.2016.05.030.
(93) Reichling, J.; Kulacki, F. Utility Scale Hybrid Wind–Solar Thermal Electrical Generation: A Case Study for Minnesota. *Energy* **2008**, *33* (4), 626–638. https://doi.org/10.1016/j.energy.2007.11.001.
(94) Vick, B. D.; Moss, T. A. Adding Concentrated Solar Power Plants to Wind Farms to Achieve a Good Utility Electrical Load Match. *Sol. Energy* **2013**, *92*, 298–312. https://doi.org/10.1016/j.solener.2013.03.007.
(95) Santos-Alamillos, F. J.; Pozo-Vázquez, D.; Ruiz-Arias, J. A.; Von Bremen, L.; Tovar-Pescador, J. Combining Wind Farms with Concentrating Solar Plants to Provide Stable Renewable Power. *Renew. Energy* **2015**, *76*, 539–550. https://doi.org/10.1016/j.renene.2014.11.055.
(96) Denholm, P.; Wan, Y.-H.; Hummon, M.; Mehos, M. The Value of CSP with Thermal Energy Storage in the Western United States. *Energy Procedia* **2014**, *49*, 1622–1631. https://doi.org/10.1016/j.egypro.2014.03.171.
(97) Levi, P. J.; Kurland, S. D.; Carbajales-Dale, M.; Weyant, J. P.; Brandt, A. R.; Benson, S. M. Macro-Energy Systems: Toward a New Discipline. *Joule* **2019**, *3* (10), 2282–2286. https://doi.org/10.1016/j.joule.2019.07.017.
(98) Tong, F.; Yuan, M.; Lewis, N. S.; Davis, S. J.; Caldeira, K. Effects of Deep Reductions in Energy Storage Costs on Highly Reliable Wind and Solar Electricity Systems. *iScience* **2020**, *23* (9), 101484. https://doi.org/10.1016/j.isci.2020.101484.
(99) Assumptions to the Annual Energy Outlook 2020: Electricity Market Module. US Energy Information Administration January 2020.
(100) Turchi, C. S.; Boyd, M.; Kesseli, D.; Kurup, P.; Mehos, M.; Neises, T.; Sharan, P.; Wagner, M.; Wendelin, T. *CSP Systems Analysis - Final Project Report*; NREL/TP-5500-72856; National Renewable Energy Laboratory: Golden, CO, 2019.
(101) Turchi, C. *Parabolic Trough Reference Plant for Cost Modeling with the Solar Advisor Model (SAM)*; NREL/TP-550-47605; National Renewable Energy Laboratory: Golden, CO, 2010.
(102) Wagner, M. J.; Gilman, P. *Technical Manual for the SAM Physical Trough Model*; NREL/TP-5500-51825; National Renewable Energy Laboratory: Golden, CO, 2011.
(103) U.S. Energy Information Administration. U.S. Natural Gas Electric Power Price.
(104) *Lazard's Levelized Cost of Storage Analysis - Version 5.0*; Lazard, 2019.
(105) James, B.; Colella, W.; Moton, J.; Saur, G.; Ramsden, T. *PEM Electrolysis H2A Production Case Study Documentation*; Strategic Analysis, Inc.: Arlington, VA, 2013.
(106) Steward, D.; Ramsden, T.; Zuboy, J. *H2A Production Model, Version 2 User Guide*; NREL/TP-560-43983; National Renewable Energy Laboratory: Golden, CO, 2008.
(107) Penev, M.; Saur, G.; Hunter, C.; Zuboy, J. *H2A Hydrogen Production Model: Version 3.2018 User Guide (DRAFT)*; National Renewable Energy Laboratory: Golden, CO, 2018.
(108) *Current Central Hydrogen Production from Polymer Electrolyte Membrane (PEM) Electrolysis (2019) Version 3.2018*; National Renewable Energy Laboratory.
(109) Darrow, K.; Tidball, R.; Wang, J.; Hampson, A. *Catalog of CHP Technologies*; U.S. Environmental Protection Agency, 2015.

(110) Steward, D.; Penev, M.; Saur, G.; Becker, W.; Zuboy, J. *Fuel Cell Power Model Version 2: Startup Guide, System Designs, and Case Studies*; NREL/TP-5600-57457; National Renewable Energy Laboratory: Golden, CO, 2013.
(111) Gelaro, R.; McCarty, W.; Suárez, M. J.; Todling, R.; Molod, A.; Takacs, L.; Randles, C. A.; Darmenov, A.; Bosilovich, M. G.; Reichle, R.; Wargan, K.; Coy, L.; Cullather, R.; Draper, C.; Akella, S.; Buchard, V.; Conaty, A.; da Silva, A. M.; Gu, W.; Kim, G.-K.; Koster, R.; Lucchesi, R.; Merkova, D.; Nielsen, J. E.; Partyka, G.; Pawson, S.; Putman, W.; Rienecker, M.; Schubert, S. D.; Sienkiewicz, M.; Zhao, B. The Modern-Era Retrospective Analysis for Research and Applications, Version 2 (MERRA-2). *J. Clim.* **2017**, *30* (14), 5419–5454. https://doi.org/10.1175/JCLI-D-16-0758.1.
(112) Clack, C. T. M.; Alexander, A.; Choukulkar, A.; MacDonald, A. E. Demonstrating the Effect of Vertical and Directional Shear for Resource Mapping of Wind Power. *Wind Energy* **2016**, *19* (9), 1687–1697. https://doi.org/10.1002/we.1944.
(113) Sedaghat, A.; Hassanzadeh, A.; Jamali, J.; Mostafaeipour, A.; Chen, W.-H. Determination of Rated Wind Speed for Maximum Annual Energy Production of Variable Speed Wind Turbines. *Appl. Energy* **2017**, *205*, 781–789. https://doi.org/10.1016/j.apenergy.2017.08.079.
(114) Bett, P. E.; Thornton, H. E. The Climatological Relationships between Wind and Solar Energy Supply in Britain. *Renew. Energy* **2016**, *87*, 96–110. https://doi.org/10.1016/j.renene.2015.10.006.
(115) Open Data. U.S. Energy Information Administration.
(116) Ruggles, T. H.; Farnham, D. J.; Tong, D.; Caldeira, K. Developing Reliable Hourly Electricity Demand Data through Screening and Imputation. *Sci. Data* **2020**, *7* (1), 155. https://doi.org/10.1038/s41597-020-0483-x.
(117) Yu, L.; Zhong, S.; Bian, X.; Heilman, W. E. Temporal and Spatial Variability of Wind Resources in the United States as Derived from the Climate Forecast System Reanalysis. *J. Clim.* **2015**, *28* (3), 1166–1183. https://doi.org/10.1175/JCLI-D-14-00322.1.
(118) van der Welle, A.; van der Zwaan, B. *An Overview of Selected Studies on the Value of Lost Load (VOLL)*; Energy research Centre of the Netherlands (ECN), 2007.
(119) Dowling, A. W.; Zheng, T.; Zavala, V. M. Economic Assessment of Concentrated Solar Power Technologies: A Review. *Renew. Sustain. Energy Rev.* **2017**, *72*, 1019–1032. https://doi.org/10.1016/j.rser.2017.01.006.
(120) Sonawane, P. D.; Bupesh Raja, V. K. An Overview of Concentrated Solar Energy and Its Applications. *Int. J. Ambient Energy* **2018**, *39* (8), 898–903. https://doi.org/10.1080/01430750.2017.1345009.
(121) Murphy, C.; Sun, Y.; Cole, W.; Maclaurin, G.; Turchi, C.; Mehos, M. *The Potential Role of Concentrating Solar Power within the Context of DOE's 2030 Solar Cost Targets*; NREL/TP-6A20-71912; National Renewable Energy Laboratory: Golden, CO, 2019.
(122) U.S. Department of Energy. Combined Heat and Power Technology Fact Sheet Series: Steam Turbines. July 2016.
(123) Silva-Pérez, M. A. Solar Power Towers Using Supercritical CO2 and Supercritical Steam Cycles, and Decoupled Combined Cycles. In *Advances in Concentrating Solar Thermal Research and Technology*; Elsevier, 2017; pp 383–402. https://doi.org/10.1016/B978-0-08-100516-3.00017-4.
(124) *Hydropower Vision*; DOE/GO-102016-4869; U.S. Department of Energy, 2016.

(125) Gençer, E.; Mallapragada, D. S.; Maréchal, F.; Tawarmalani, M.; Agrawal, R. Round-the-Clock Power Supply and a Sustainable Economy via Synergistic Integration of Solar Thermal Power and Hydrogen Processes. *Proc. Natl. Acad. Sci.* **2015**, *112* (52), 15821–15826. https://doi.org/10.1073/pnas.1513488112.
(126) del Río, P.; Peñasco, C.; Mir-Artigues, P. An Overview of Drivers and Barriers to Concentrated Solar Power in the European Union. *Renew. Sustain. Energy Rev.* **2018**, *81*, 1019–1029. https://doi.org/10.1016/j.rser.2017.06.038.
(127) Budischak, C.; Sewell, D.; Thomson, H.; Mach, L.; Veron, D. E.; Kempton, W. Cost-Minimized Combinations of Wind Power, Solar Power and Electrochemical Storage, Powering the Grid up to 99.9% of the Time. *J. Power Sources* **2013**, *225*, 60–74. https://doi.org/10.1016/j.jpowsour.2012.09.054.
(128) Mills, A. D.; Millstein, D.; Jeong, S.; Lavin, L.; Wiser, R.; Bolinger, M. Estimating the Value of Offshore Wind along the United States' Eastern Coast. *Environ. Res. Lett.* **2018**, *13* (9), 094013. https://doi.org/10.1088/1748-9326/aada62.
(129) Mayfield, E. N.; Cohon, J. L.; Muller, N. Z.; Azevedo, I. M. L.; Robinson, A. L. Cumulative Environmental and Employment Impacts of the Shale Gas Boom. *Nat. Sustain.* **2019**, *2* (12), 1122–1131. https://doi.org/10.1038/s41893-019-0420-1.